GA–A27230

THERMOCHEMICAL HEAT STORAGE FOR CONCENTRATED SOLAR POWER

FINAL PROJECT REPORT FOR THE PERIOD SEPTEMBER 30, 2008 THROUGH OCTOBER 31, 2011

by
PROJECT STAFF

Prepared for the
U.S. Department of Energy
under DE-FG36-08GO18145

DATE PUBLISHED: MARCH 2012

GENERAL ATOMICS

DISCLAIMER

GA–A27230

THERMOCHEMICAL HEAT STORAGE FOR CONCENTRATED SOLAR POWER

FINAL PROJECT REPORT FOR THE PERIOD SEPTEMBER 30, 2008 THROUGH OCTOBER 31, 2011

by
PROJECT STAFF

Prepared for the
U.S. Department of Energy
under DE-FG36-08GO18145

GENERAL ATOMICS PROJECT 30314
DATE PUBLISHED: MARCH 2012

GENERAL ATOMICS

EXECUTIVE SUMMARY

Thermal energy storage (TES) is an integral part of a concentrated solar power (CSP) system. It enables plant operators to generate electricity beyond on sun hours and supply power to the grid to meet peak demand. Current CSP sensible heat storage systems employ molten salts as both the heat transfer fluid and the heat storage media. These systems have an upper operating temperature limit of around 400°C. Future TES systems are expected to operate at temperatures between 600°C–1000°C for higher thermal efficiencies which should result in lower electricity cost.

To meet future operating temperature and electricity cost requirements, a TES concept utilizing thermochemical cycles (TCs) based on multivalent solid oxides was proposed. The system employs a pair of reduction and oxidation (REDOX) reactions to store and release heat. In the storage step, hot air from the solar receiver is used to reduce the oxidation state of an oxide cation, e.g. Fe^{3+} to Fe^{2+}. Heat energy is thus stored as chemical bonds and the oxide is "charged." To discharge the stored energy, the reduced oxide is re-oxidized in air and heat is released. Air is used as both the heat transfer fluid and reactant and no storage of fluid is needed. This project investigated the engineering and economic feasibility of this proposed TES concept. The DOE storage cost and LCOE targets are \$15/kWh and \$0.09/kWh respectively.

Sixteen pure oxide cycles were identified through thermodynamic calculations and literature information. Data showed the kinetics of re-oxidation of the various oxides to be a key barrier to implementing the proposed concept. A down selection was carried out based on operating temperature, materials costs and preliminary laboratory measurements. Cobalt oxide, manganese oxide and barium oxide were selected for developmental studies to improve their REDOX reaction kinetics.

A novel approach utilizing mixed oxides to improve the REDOX kinetics of the selected oxides was proposed. It partially replaces some of the primary oxide cations with selected secondary cations. This causes a lattice charge imbalance and increases the anion vacancy density. Such vacancies enhance the ionic mass transport and lead to faster re-oxidation. Re-oxidation fractions of $Mn_3O_4 \rightarrow Mn_2O_3$ and $CoO \rightarrow Co_3O_4$ were improved by up to 16 fold through the addition of a secondary oxide. However, no improvement was obtained in barium based mixed oxides. In addition to enhancing the short term re-oxidation kinetics, it was found that the use of mixed oxides also help to stabilize or even improve the TES properties after long term thermal cycling. Part of this improvement could be attributed to a reduced grain size in the mixed oxides. Based on the measurement results, manganese-iron, cobalt-aluminum and cobalt-iron mixed oxides have been proposed for future engineering scale demonstration.

Using the cobalt and manganese mixed oxides, we were able to demonstrate charge and discharge of the TES media in both a bench top fixed bed and a rotary kiln-moving bed reactor.

Operations of the fixed bed configuration are straight forward but require a large mass flow rate and higher fluid temperature for charging. The rotary kiln makes direct solar irradiation possible and provides significantly better heat transfer, but designs to transport the TES oxide in and out of the reactor will need to be defined. The final reactor and system design will have to be based on the economics of the CSP plant. A materials compatibility study was also conducted and it identified Inconel 625 as a suitable high temperature engineering material to construct a reactor holding either cobalt or manganese mixed oxides.

To assess the economics of such a CSP plant, a packed bed reactor model was established as a baseline. Measured cobalt-aluminum oxide reaction kinetics were applied to the model and the influences of bed properties and process parameters on the overall system design were investigated. The optimal TES system design was found to be a network of eight fixed bed reactors at 18.75 MW_{th} each with charge and discharge temperatures between 1200°C and 600°C, which provides a constant output temperature of 900°C. The charge and discharge time are 8 hours each respectively. This design was integrated into a process flowsheet of a CSP plant and the system's economics were determined using AspenPlus and NREL's Solar Advisory Model. Storage cost is very sensitive to materials cost and was calculated to be based around $40/kWh for cobalt based mixed oxide. It can potentially decrease to $10/kWh based on reduced materials cost on a bulk scale. The corresponding calculated LCOE was between $0.22–0.30/kW-h. The high LCOE is a result of the high charging temperature required in this first design and the cost of cobalt oxide. It is expected that a moving bed reactor using manganese oxide will significantly improve the economics of the proposed concept.

In conclusion, the project has demonstrated the engineering feasibility of using a multivalent solid oxide for TES applications. Preliminary system designs and process pathways have been defined. A system based on manganese oxide and a rotary kiln has the potential to meet the DOE economic targets.

TABLE OF CONTENTS

LIST OF FIGURES

LIST OF TABLES

1. INTRODUCTION

Solid oxide based thermochemical cycles (TCs) have been investigated for use in high density solar Thermal Energy Storage (TES) applications. Heat storage and retrieval are accomplished via reduction and subsequent re-oxidation (REDOX) of solid metal oxides e.g. Co_3O_4 (s) $\leftrightarrow$ CoO (s) + ½O_2 (g). The baseline system concept utilizes a packed bed reactor for charging and discharging of the TES oxide. During on sun hours, hot air from the solar cavity flows through the fixed oxide bed and heats the TES oxide to above the equilibrium transition temperature (Fig. 1.1). The oxide undergoes a reduction and is thus "charged." For heat recovery or "discharge," cool air is introduced into the reactor and oxidizes the reduced oxide. Heat is released and the temperature of the flowing air is raised. The outlet air temperature remains at or near the transition temperature during both day and night operations. The REDOX reactions can also be carried out in a moving bed reactor in which TES oxide flows in and out of the solar reactor. In this case, heating of the oxide can be accomplished via direct solar irradiation resulting in more efficient heat transfer. The proposed TES concept utilizes air as both the heat transfer fluid and the reactant. Storage of air is not necessary and such a system is classified as "open." Similar TES REDOX reactions can also be carried out with carbon dioxide or water based systems. In those cases, the working gases require storage and are thus termed "closed."

There are a number of advantages in using an open loop oxide based TC to store solar heat energy:

- Heat can be stored indefinitely in chemical bonds
- Heat storage capacity (kJ/kg) is high compared to sensible heat storage
- Heat is released at a constant temperature which provides a constant heat source. A TC can be selected to match the required turbine operating temperature
- Air is used as both the heat transfer medium and reactant. No corrosive fluid or high temperature solid needs to be handled. Only solid oxides need to be stored and there is no need to compress gases for storage
- Minimal environmental effect for most oxide cycles

This project's goal is to identify, assess and develop TCs that are applicable to the proposed "open" loop concept and demonstrate the technology's economic and engineering feasibility and advantages when integrated with a solar power plant. DOE's storage cost and LCOE targets are \$15/kWh and \$0.09/kWh respectively. Three phases were planned for this project, two of which have been completed. A block diagram showing the main project tasks is shown in Fig. 1.2. In Phase I, a survey of potentially applicable oxide systems was carried out. The metal-air thermodynamic phase equilibria for pure solid metal oxides were established via HSC chemistry software. A preliminary down select of applicable TCs based on equilibrium temperature and calculated storage cost was carried out. A literature survey on the REDOX behavior of the remaining oxide systems and their mixed oxides was conducted. Experimental measurements on the REDOX properties of some of the candidate oxides were also carried out in parallel. Based on all the available data, a final down select was performed and it identified manganese oxide, cobalt oxide and barium oxide as potential TES candidates for further development in Phase II.

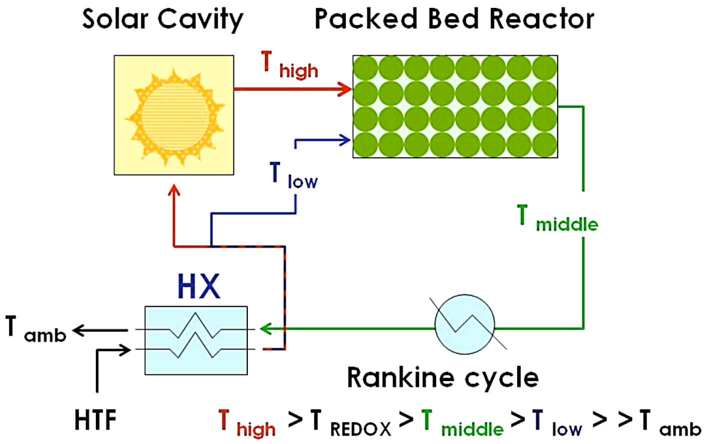

$$MO_{2x+1} \rightarrow MO + xO_2 \longrightarrow \text{On sun endo. (charge)}$$
$$MO + xO_2 \rightarrow MO_{2x+1} \longrightarrow \text{Off sun exo. (discharge)}$$

Fig. 1.1. Process flow diagram schematic of the baseline solid oxide based TES concept.

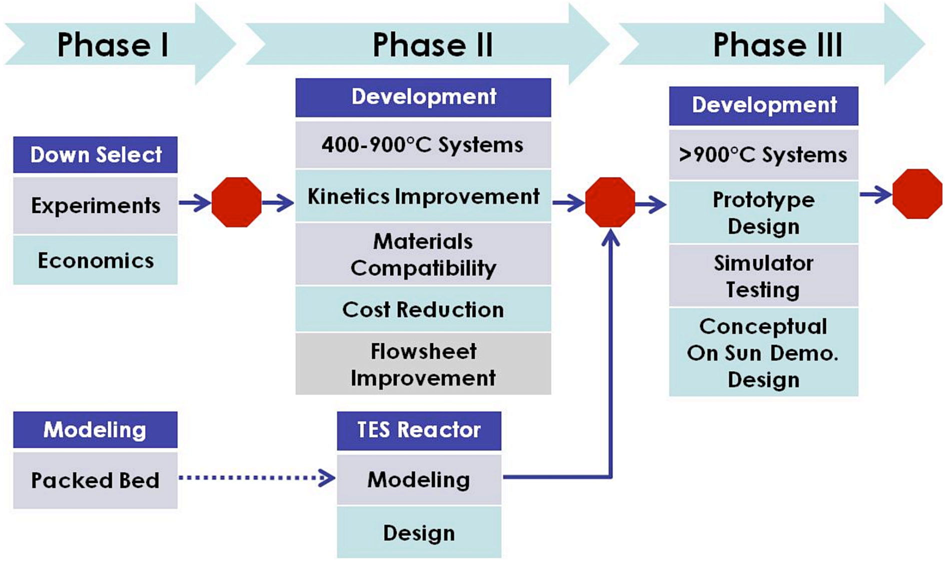

Fig. 1.2. Block diagram showing the key project activities.

Phase II addressed two key areas: (i) the sluggish oxide re-oxidation kinetics of the three pure oxides and (ii) reactor design, system integration and economics. The team was able to successfully enhance the short and long term reaction kinetics of cobalt and manganese based oxides through the incorporation of secondary oxides. The mixed oxides enable higher oxygen mass transfer in addition to limiting oxide grain growth under prototypical operating conditions. For reactor design, a model was developed based on experimental measured kinetics. Reactor dimension, mass flow rate and process boundary conditions were derived based on the required power level. The charge and discharge was modeled in detail and the results were applied to calculate the economics of the overall system. Materials compatibility tests were conducted to identify materials that can be used to construct a bench top test model. Key highlights of the project are presented in the following sections. Details can be found in various GA reports listed in Table 1.1.

1.1. TECHNICAL REPORTS

Table 1.1
List of General Atomics Technical Reports

GA Report No.	Title	Date
GA-C26524	Quarterly Report	JUN2009 2Q SEP2009 3Q DEC2009 4Q MAR2010 1Q JUN2010 2Q SEP2010 3Q DEC2010 4Q MAR2011 1Q
GA–C26617	Survey on Multivalent Metal Oxides Applicable to Thermal Heat Storage	NOVEMBER 2009
GA–C26695	Promising Thermochemical Cycles for Thermochemical Heat Storage Down Select	MARCH 2010
GA–C26699	Evaluation of MnO_2 REDOX Cycle for Thermal Energy Storage	MARCH 2010
GA-C26645	Milestone Report on the Experimental Evaluation Protocol for Solid Oxides Based Thermochemical Cycle	FEBRUARY 2010
GA–C27022	Oxide-Based Thermal Energy Storage	JANUARY 2011
GA-C27024	Construction Materials Compatibility with Solid Oxide-Based Thermal Energy Storage	FEBRUARY 2011
GA-C27055	Solid Oxide-Based Thermochemical Cycles Applicable to Thermal Heat Storage for Temperatures between 450°C–700°C and 700°C–900°C	APRIL 2011

1.2. LIST OF PRESENTATIONS

Lloyd Brown, “Multivalent Metal Oxides for Thermochemical Energy Storage,” Poster Presentation at 14th Annual Solarpaces Conference, 2009, Berlin, Germany.

Bunsen Wong, “Thermochemical Heat Storage for Concentrated Solar Power,” Oral Presentation at the DOE CSP Project Review, 2010 Albuquerque, New Mexico.

Bunsen Wong, “Oxide Based Thermochemical Heat Storage,” Oral Presentation at the 15th Annual Solarpaces Conference, 2010 Perpignan, France.

Bunsen Wong, “Thermochemical Heat Storage for Concentrated Solar Power Based on Multivalent Metal Oxides,” Oral Presentation at the DOE CSP Project Review, 2011 Golden, Colorado.

Robert Buckingham, “Metal Oxide Based Thermochemical Energy Storage for Concentrated Solar Power – Thermodynamics and Parasitic Loads for Packed Bed Reactors,” Poster Presentation at the 16th Annual Solarpaces Conference, 2011, Granada, Spain.

1.3. LIST OF PUBLICATIONS

Bunsen Wong, Lloyd Brown, Franziska Schaube, Rainer Tamme and Christian Sattler, “Oxide Based Thermochemical Heat Storage,” Proceedings of 15th Annual Solarpaces Conference, Perpignan, France.

Robert Buckingham, Bunsen Wong, Lloyd Brown, Christian Sattler, Franziska Schaube and, Antje Woerner, “Metal Oxide Based Thermochemical Energy Storage for Concentrated Solar Power – Thermodynamics and Parasitic Loads for Packed Bed Reactors,” Proceedings of 16th Annual Solarpaces Conference, Granada, Spain.

Martina Neises, Stefania Tescari, Lamark de Oliveira, Martin Roeb, Christian Sattler and Bunsen Wong, “Solar-Heated Rotary Kiln for Thermochemical Energy Storage,” submitted to the International Journal of Energy Research.

2. METAL OXIDE SYSTEM SURVEY AND DOWN SELECT

2.1. REDOX OXIDE SYSTEMS EVALUATION USING HSC CHEMISTRY

HSC Chemical Reaction and Equilibrium Software was used to calculate the equilibrium thermodynamics of all solid oxide – air systems. HSC is designed for various kinds of chemical reaction and equilibrium calculations as well as process simulation. In this study, nominal air (79%N2-21%O2) at atmospheric pressure was used as the carrier gas. A total of 74 different pure solid oxide systems were evaluated and they are highlighted in Fig. 2.1.

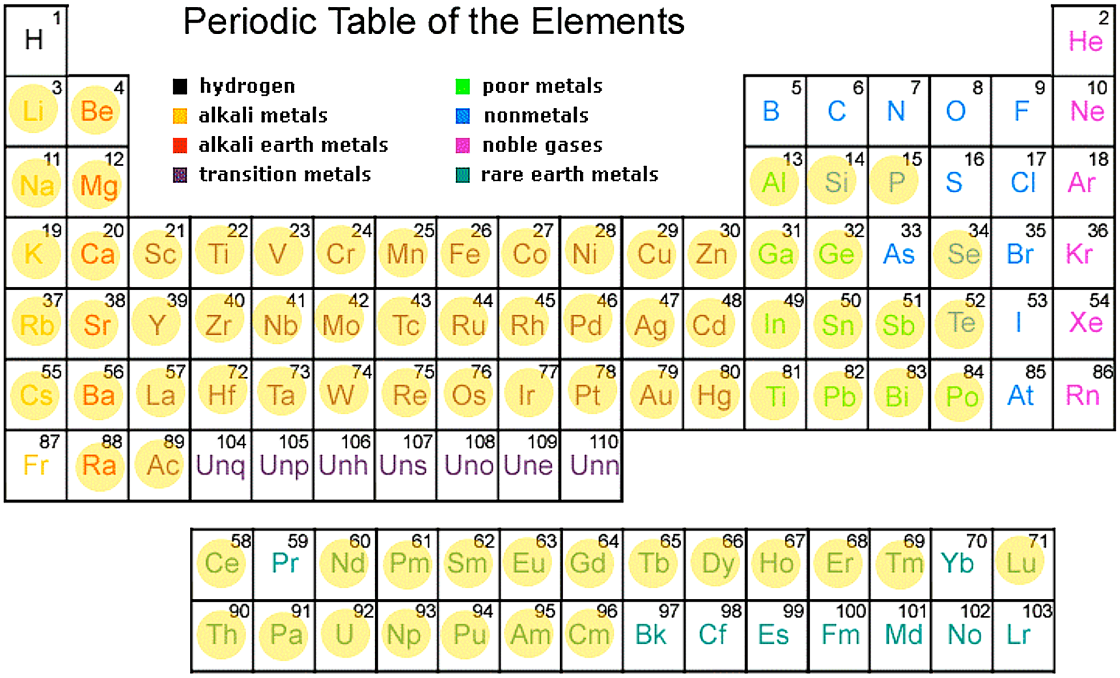

Fig. 2.1 Periodic table showing oxide of elements (marked in yellow) that have been evaluated with HSC software.

Figure 2.2 shows examples of the HSC calculation results. A $Co_3O_4 \leftrightarrow CoO$ REDOX transition, which takes place at an equilibrium temperature of 890°C, is illustrated in the cobalt oxide-air phase stability diagram [Fig. 2.2(a)]. The enthalpy of this reaction is 202 kJ/mole (844 kJ/kg) of Co_3O_4. Oxides with similar sharp transition can be used for TES as they can absorb and release heat within a very narrow temperature range. This can be compared with the phase stability diagram of the nickel oxide-air system [Fig. 2.2(b)]. There is no REDOX transition so the system is not suitable for TES. Details of all calculation results can be found in General Atomics report GA-A20323.

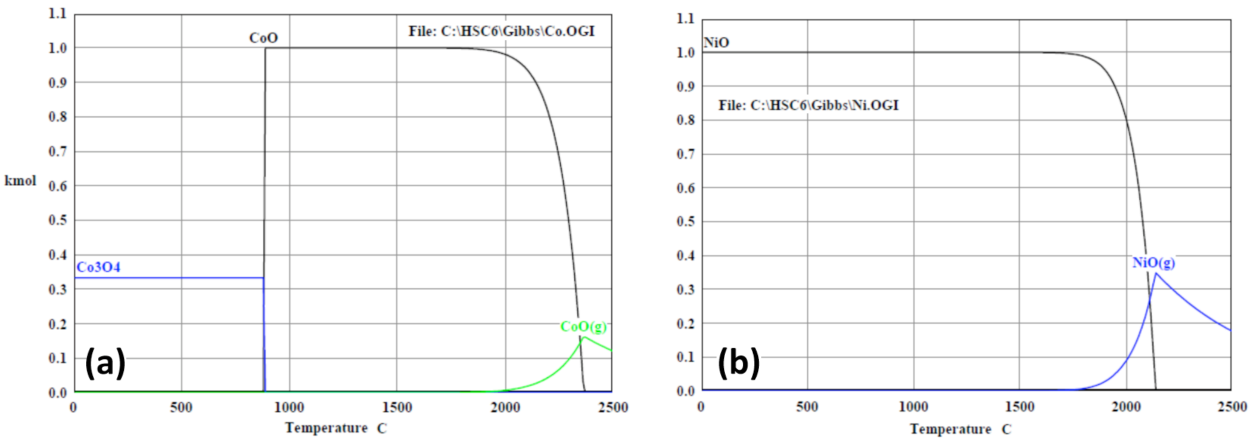

Fig. 2.2. Phase stability diagrams for the (a) cobalt oxide-air and (b) nickel-oxide air at ambient pressure. Air is the carrier gas.

The HSC effort yielded a total of 16 pure oxide TES candidates. Lanthanide and actinide oxides that showed useful TES characteristics were not included as their use is not practical. Table 2.1 lists the enthalpy and the heat storage density associated with the oxide candidates.

Table 2.1
Metal Oxide Systems Applicable to TES Based on Thermodynamics Considerations

Reaction	**Temperature (°C)**	**ΔH (kJ/mole oxide)**	**Storage Density (kJ/kg)**
$Cr_5O_{12} \rightarrow 2.5Cr_2O_3 + 2.25O_2$	110	126.0	279
$2Li_2O_2 \rightarrow 2Li_2O + O_2$	150	68.2	1483
$2Mg_2O \rightarrow 2MgO + O_2$	205	21.8	505
$2PbO_2 \rightarrow 2PbO + O_2$	405	62.8	262
$2PtO_2 \rightarrow 2PtO + O_2$	420	62.8	277
$2Sb_2O_5 \rightarrow 2Sb_2O_4 + O_2$	515	92.5	286
$4MnO_2 \rightarrow 2Mn_2O_3 + O_2$	530	41.8	481
$6UO_3 \rightarrow 6U_3O_8 + O_2$	670	35.2	123
$2BaO_2 \rightarrow 2BaO + O_2$	885	72.5	474
$2Co_3O_4 \rightarrow 6CoO + O_2$	890	202.5	844
$Rh_2O_3 \rightarrow Rh_2O + O_2$	970	249.2	981
$6Mn_2O_3 \rightarrow 4Mn_3O_4 + O_2$	1000	31.9	202
$4CuO \rightarrow 2Cu_2O + O_2$	1120	64.5	811
$6Fe_2O_3 \rightarrow 4Fe_3O_4 + O_2$	1400	79.2	496
$2V_2O_5 \rightarrow 2V_2O_4 + O_2$	1560	180.7	993
$2Mn_3O_4 \rightarrow 6MnO + O_2$	1700	194.6	850

The equilibrium reaction temperatures of Cr_5O_{12}, Li_2O_2 and Mg_2O are below 250°C. At these temperatures, REDOX reaction kinetics are slow and heat recovery is inefficient. Hence, they are removed from consideration. Figure 2.3 shows the estimated TES raw materials costs for the remaining 13 oxide candidates calculated based on their theoretical reaction enthalpies (this estimation did not take into account the sensible heat of the oxide). The materials costs ($/kg) were derived using published internet values so they may be higher than the actual cost in bulk. Results showed PtO_2, Rh_2O_3 and UO_3 are too expensive for use with the present TES concept as material costs alone are two orders of magnitude above the DOE target of $15/kWh. They were eliminated from future deliberation. A total of 10 potential candidates remained and they are classified based on their equilibrium temperatures in Table 2.2.

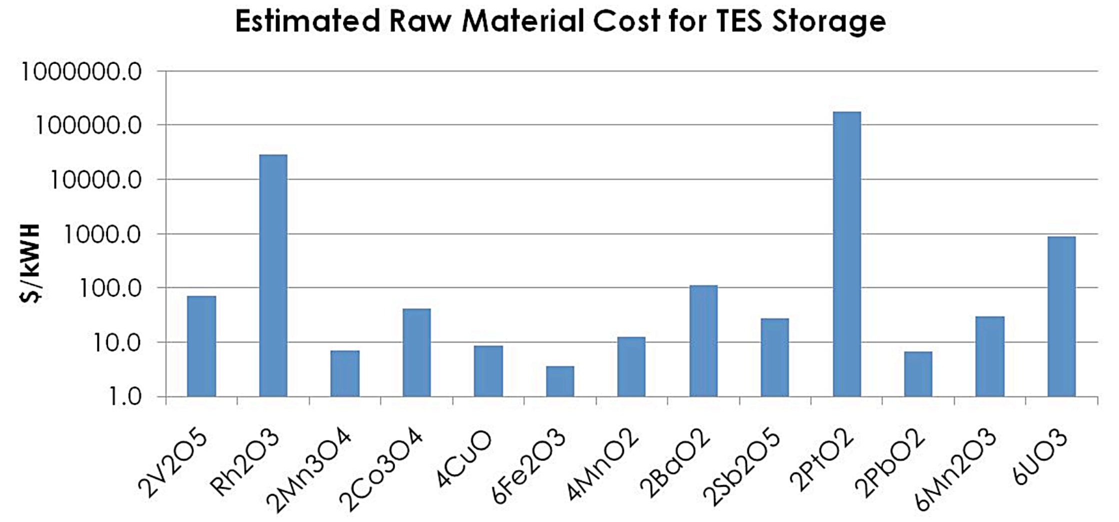

Fig. 2.3 Raw material cost for TES using various oxides.

Table 2.2
Potential TES Oxide Candidates

Temperature	TES Oxide Candidates
350°C<T<700°C	MnO_2, Sb_2O_5
700°C<T<900°C	Co_3O_4, BaO, Mn_2O_3
900°C<T<1100°C	CuO
1100°C<T	Fe_2O_3 , Mn_3O_4, V_2O_5

2.2. LITERATURE SURVEY ON PURE AND MIXED OXIDE SYSTEMS

A literature survey on the REDOX characteristics of the pure oxides listed in Table 2.2 and their mixed systems was carried out. Complete details of this survey can be found in General Atomics report GA-C26617. A summary is provided in the following sections.

2.2.1. Manganese Oxides

The manganese-oxygen system has four different stable oxides: $MnO_2 \rightarrow Mn_2O_3 \rightarrow Mn_3O_4 \rightarrow MnO$. The three REDOX reactions can all be used for TES but since the equilibrium temperature of the $Mn_3O_4 \leftrightarrow MnO$ transition is too high, 1700°C, it is not considered in this project. The reduction of all manganese oxides takes place readily and the reversibility of $Mn_2O_3 \leftrightarrow Mn_3O_4$ and $Mn_3O_4 \leftrightarrow MnO$ REDOX reactions have been demonstrated at ambient pressure. No re-oxidation of Mn_2O_3 into MnO_2 at ambient pressure has been observed, but the literature reports that reaction may require a pure oxygen gas pressure of 3000 bar. Various intermediate oxides have been observed in the $MnO_2 \rightarrow Mn_2O_3$ decomposition process and their existence is related to the oxide preparation method. The absence of $MnO_2 \rightarrow Mn_2O_3$ re-oxidation may be related to the existence of such intermediate phases. Manganese oxide particle size also plays an important role on the re-oxidation process. High surface area, i.e. fine grain size, reduces the re-oxidation temperature of Mn_3O_4. In summary, the manganese oxide systems have many attributes that enable for them to be considered for TES media.

2.2.2. Cobalt Oxide

The cobalt oxide system has only one transition: Co_3O_4, a spinel, decomposes into CoO at temperatures around 890°C and above in air [Fig. 2.2(a)]. The REDOX reactions are readily reversible and reaction kinetics were shown to be controlled primarily by heat transfer and diffusion. The $Co_3O_4 \leftrightarrow CoO$ system is well-suited for use in the proposed TES concept. Previous worked showed larger CoO particles could not be fully re-oxidized at low re-oxidation temperatures due to a surface Co_3O_4 layer acting as a barrier. In addition, REDOX performance was shown to decrease with cycling. Thus, the long term REDOX performance of cobalt oxide will need to be addressed.

2.2.3. Iron Oxides

The iron oxygen system has two known REDOX transitions: $Fe_2O_3 \leftrightarrow Fe_3O_4$ and $Fe_3O_4 \leftrightarrow FeO$. The equilibrium temperature for $Fe_3O_4 \rightarrow FeO$ decomposition in air is above 2000°C so this reaction is not considered within the framework of the present project. Fe_2O_3 (hematite) and Fe_3O_4 (magnetite) are among the most common materials on earth and their reactions are very well characterized and the reversibility of this transition has been documented. Reduction of $Fe_2O_3 \rightarrow Fe_3O_4$ begins to take place at temperatures above 1200°C. Re-oxidation proceeds also at a rapid rate but high moisture content has been shown to retard this process. The key problem associated with this transition is the formation of transformation stress induced porosity and cracks during the reduction step. This leads to a severe attrition problem and makes this system not suitable for TES.

2.2.4. Lead Oxide

Lead oxide is another attractive TES candidate as it is a low cost material. HSC calculation results showed only two stable lead oxide phases: $PbO_2 \leftrightarrow PbO$. However, a survey of literature revealed many intermediate Pb-O phases as the presence of impurities and lattice strain led to the formation of various lead oxide intermediates. Depending on sample history, the transition temperatures and nature of Pb-O phases would vary. Formation of intermediate oxides means heat is not released in a narrow temperature range but is discharged continuously as the reduced lead oxide goes through the different oxidation states. Such heat release mechanism is not ideal for the proposed TES concept which works best with a narrow temperature output range.

2.2.5. Antimony Oxide

HSC Chemistry showed only one transition in the antimony air-oxide system: $Sb_2O_5 \rightarrow Sb_2O_4$. On the other hand, the literature review showed the most common antimony oxide is a metastable Sb_2O_3. The transitions between Sb_2O_3, Sb_2O_4 and Sb_2O_5 are relatively complicated due to the thermal instability of Sb_2O_5 and the volatility of Sb_2O_3. Decomposition of Sb_2O_5 into Sb_2O_4 has been demonstrated whereas re-oxidation in air has not. Thus, it is doubtful whether pure antimony oxide can be used for TES.

2.2.6. Vanadium Oxide

HSC calculation results showed a $V_2O_5 \rightarrow V_2O_4$ (VO_2) transition in the vanadium oxide-air phase stability diagram. Upon review, literature data showed an additional higher temperature transition between $VO_2 \rightarrow V_2O_3$. A number of other intermediate oxide phases such as V_3O_5 , V_4O_7 and V_6O_{13} etc have been identified repeatedly. The reduction kinetics in air may be slow as full $V_2O_5 \rightarrow V_2O_3$ conversion in an inert gas environment took 5 hours to complete. Exposure of V_2O_3 to air has been shown to promote oxidation to VO_2 but the re-oxidation kinetics with respect to the re-oxidation temperature range were not known. Similar to lead oxide, the presence of many intermediate phases makes vanadium oxide not very suitable for TES use.

2.2.7. Barium Oxide

Only BaO and BaO_2 are present in the barium oxide – air system as modeled by HSC Chemistry. The use of the $BaO_2 \leftrightarrow BaO$ REDOX transition as a chemical heat storage mechanism had been explored previously. The REDOX reactions were shown to be reversible but the conversion fraction decreased as the barium oxide went through additional cycling. This was due to the formation of a BaO_2 ash layer on the surface of BaO particles during re-oxidation, similar to what was observed in cobalt oxide. The thickness of this layer formed an oxygen diffusion barrier around the BaO particles and slowed down re-oxidation. To make barium oxide usable for TES, stable high diffusion paths are needed to ensure complete reversibility of this transition.

2.2.8. Copper Oxide

Both HSC chemistry and literature data showed only a $CuO \leftrightarrow Cu_2O$ transition in the copper oxide-air system. Reduction in air takes place at temperature close to a 1000°C. Since the melting point of Cu_2O is at 1232°C, the proximity between transition temperature and melting point could pose problems to the physical operation of the TES system since grain coarsening will be extensive. Literature data showed re-oxidation of Cu_2O can take place at a temperature significantly lower than equilibrium transition. This capacity will provide flexibility in the design and operation of the TES system. Hence, copper oxide is a potential TES candidate.

2.3. MIXED METAL OXIDES

There are two types of mixed oxide REDOX reactions: (i) solid-solid and (ii) solid solution. In the first type, the two oxides form a single phase oxide after the reaction:

$$Mn_2O_3 + 2Fe_2O_3 \rightarrow 2MnFe_2O_4 + O_2$$

Such a system is not practical for TES as thermal cycling of oxides will result in material attrition. In the latter, cations take up different lattice sites in an oxide matrix and the mixed oxide undergoes REDOX similar to a pure oxide. e.g.:

$$Co_2NiO_4 \rightarrow Co_2NiO_3 + \tfrac{1}{2}O_2$$

Such systems are applicable for TES and the selection and amount of the secondary cation see essential. In such mixed oxides, a primary metal cation is replaced by a secondary cation in the oxide lattice. The replacement can be stoichiometric, e.g. substitution of Co by Ni in Co_3O_4 to form Co_2NiO_4, or partial, e.g. doping of Co_3O_4 with Fe_2O_3. It has been shown that $FeNiCoO_4$ does not decompose in contrast to Co_2NiO_4. This is due to the locations of cations in the spinel oxide structure. The original substitution of Co by Ni resulted in a local charge imbalance because both Co^{3+} and Ni^{2+} have a strong preference for octahedral sites in the spinel structure. Hence, when Ni^{2+} replaces Co^{3+} the resulting $Co^{2+}[\ Ni^{2+}Co^{3+}]O_4$ oxide has one positive charge unallocated. This imbalance forces the creation of oxygen anion vacancies which enhances the REDOX process. On the other hand, Fe^{3+} replaces Co^{2+} in the tetrahedral site and resulted in a neutral lattice with sluggish kinetics.

This effect of charge imbalance on kinetics was demonstrated in pure oxides in which a small amount of secondary metal oxide was dissolved (doped). Doping reduces the phase transition temperatures based on the thermodynamics. This was confirmed by the additions Co_3O_4 into Mn_3O_4 and Mn_2O_3 into Fe_2O_3 etc. The doping cations in the primary lattice leads to an increase in the concentration of the anionic (oxygen) vacancies. They act as active centers for the chemisorption of oxygen and subsequent oxidation. The effectiveness will depend on the valence state and ionic radii of the dissolved secondary cations. Such additions have been shown to increase the reactivity between CoO and oxygen and reduce the Co_3O_4 decomposition temperature. Similar approaches have been used to modify lead and vanadium oxides. Hence, the replacements of cations have the capacity to modify the REDOX reaction kinetics.

2.4. PEROVSKITE OXIDES

The third type of oxide that was found to be applicable to TES is those based on the perovskite structure. These are usually rare-earth/transition metal mixed oxides and an example of a perovskite oxidation reaction is $La_2CoO_{4.0} + x/2\ O_2 \rightarrow La_2CoO_{4\ +\ x}$. Perovskites have extremely high oxygen transport at room temperature due to their large, open unit cells and the existence of extended defects. Diffusion coefficients along these defects can be 6-8 orders of magnitude higher than bulk materials. Many perovskite oxides have been developed for use as solid oxide fuel cell materials because of their high oxygen permeability. Replacement of rare earth and transition metal cations further creates oxygen vacancies which in turn enhance both conductivity of the oxide and the REDOX kinetics. These oxygen vacancies act as absorption sites for the re-oxidation of the perovskite. Even though perovskites have the desirable properties for TES media, they require extensive processing and their use in an application that requires large quantities of materials is uncertain.

3. CHARACTERIZATION OF TES OXIDE CANDIDATES

To assess the suitability of various oxide candidates for TES application, various measurements and characterization techniques were employed to examine the oxides' short and long term REDOX reaction properties and process induced structural modifications. The data helped define the thermodynamics and the kinetics of pure and mixed oxides and the suitability of the oxides for long term application. Four different test systems were used for the measurements. They are (i) Thermogravimetric Analyzer (TGA), (ii) Thermal Cyclic System, (iii) Bench Top Packed Bed Reactor and (iv) Rotary Kiln Reactor. X-ray diffraction and scanning electron microscopy were employed for structural characterizations. Details of the measurement techniques and results can be found in General Atomics report GA-C26645. Highlights of the results are contained in the following sections.

3.1. CHARACTERIZATION TEST SYSTEMS

3.1.1. Thermogravimetric Analysis (TGA)

TGA measures reaction characteristics as a function of temperatures, heat and cooling rates and carrier gas content while using a very small amount of sample material. The specimen's weight change, heat absorption and release and variation in the carrier gas composition are measured simultaneously. The resulting data is used to determine the kinetics of both reduction (charging) and re-oxidation (discharging) reactions. TGA is a fast and convenient tool to determine whether an oxide candidate has suitable TES characteristics.

Figure 3.1 shows the TGA plot of a Co_3O_4 sample subjected to heating and cooling at a rate of 1°C/min. Air was used as the carrier gas. As Co_3O_4 was heated above the equilibrium temperature, the endothermic reduction reaction ($Co_3O_4 \rightarrow CoO + O_2$) took place resulting in a weight loss due to oxygen release. The sample is "charged." As the sample cooled below the equilibrium temperature, it was oxidized by oxygen in an exothermic reaction and released the stored energy. Consequently, weight that was lost during reduction was recovered. The intake and release of thermal heat are marked by the endo- and exothermic peaks in the heat flow curve. This plot illustrates the required TGA characteristics of a TES medium.

3.1.2. Thermal Cyclic System

Literature review indicated that long term REDOX performance is a critical issue for solid oxide based TES. In view of this, a thermal cyclic system was constructed to help assess the long term REDOX characteristics of TES oxide candidates. Test samples were cycled through the transition temperature as the sample carrier moved in and out of the tube furnace (Fig. 3.2). TGA studies were then carried out to determine REDOX characteristics of cycled samples. The system was also used to test compatibility between TES oxide candidates and various construction materials. Coupons were embedded in selected oxides for these tests.

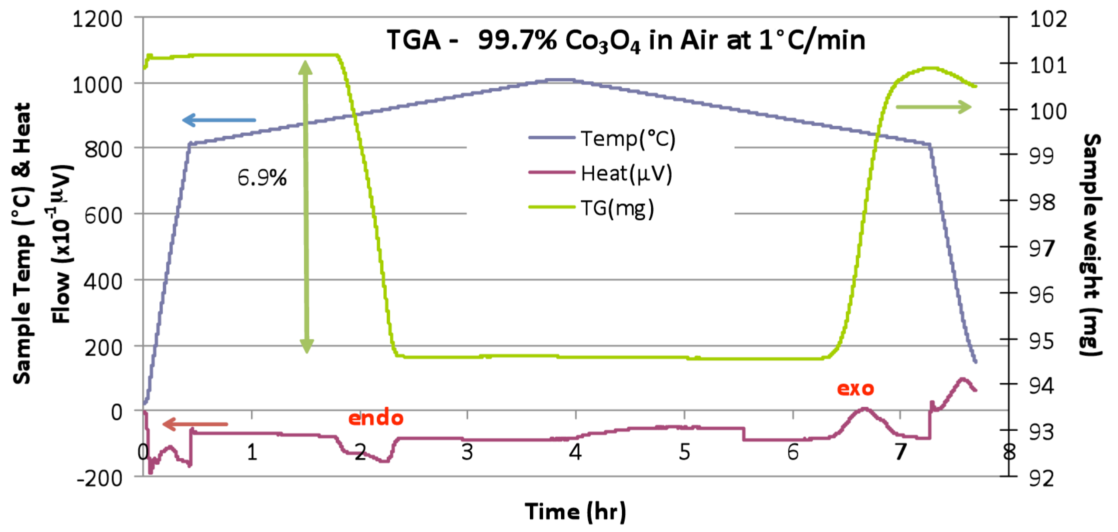

Fig. 3.1. TGA plot of Co_3O_4 oxide that was heated and cooled at a rate of 1°C/min. Air is the carrier gas.

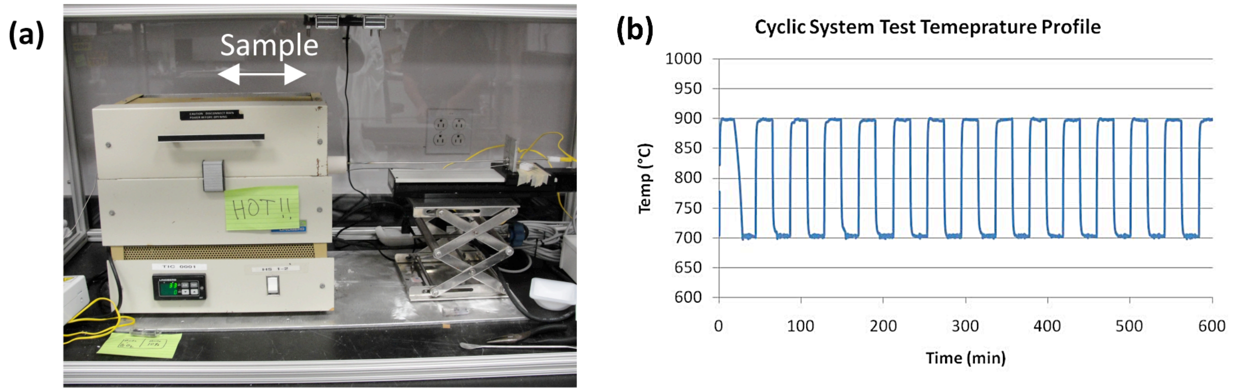

Fig. 3.2. (a) Thermal cyclic test system for solid oxides and (b) system temperature profile

3.1.3. Fixed Bed TES Oxide Test Set Up

The baseline TES concept employs a packed bed reactor for both charging and discharging of the solid oxide. Thus, candidate oxides need to demonstrate the REODX characteristics in a fixed bed to verify this concept. To accomplish this, a simple packed bed test system was set up in the laboratory (Fig. 3.3). The oxide bed was packed inside a quartz tube. A multi-zone thermocouple was embedded along the bed axis to monitor temperature profile changes during REDOX.

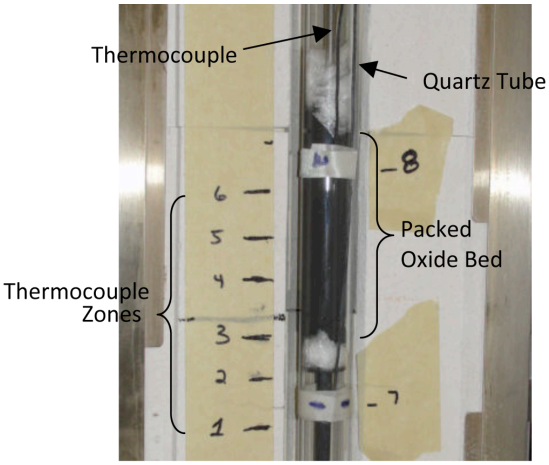

Fig. 3.3. Set up of an oxide packed bed system operating at atmospheric pressure.

3.1.4. Rotary Kiln TES Oxide Test System

A rotary kiln directly irradiated by concentrated solar radiation was used to demonstrate solid oxide REDOX in a moving bed reactor. A secondary concentrator in front of the rotary kiln is used to direct the incoming solar irradiation into the reaction chamber and provides high process temperature (Fig. 3.4). A quartz window located at the entrance plane of the secondary concentrator seals the kiln from the environment and enables the adjustment of gas compositions inside the chamber. Within the chamber the solar beam expands and irradiates the chamber wall surface and the metal oxide powder within. The re-direction and concentration of solar radiation onto the rotary kiln is carried out by a solar furnace. The energy required for metal oxide reduction is provided by the solar furnace which can provide a solar concentration of up to 5000 times.

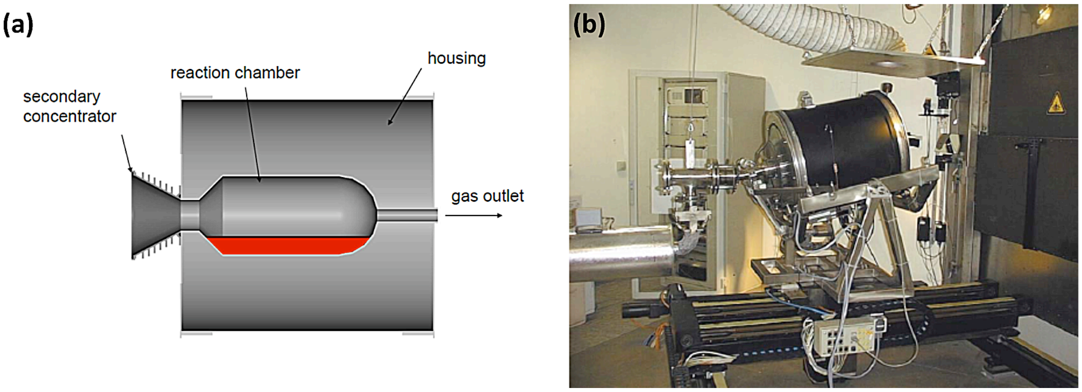

Fig. 3.4. (a) Schematic and (b) actual set up of the solar rotary kiln reactor that will be used for demonstration.

The reaction chamber of the rotary kiln is made with silicon carbide which has good thermal conductivity. To reduce heat losses and minimize thermal stresses, the chamber is insulated with ceramic fibre plates. The entire kiln is enclosed in a metal housing and can be rotated on motor driven rollers [Fig. 3.4(b)]. The rotational speed can be varied to up to 6 RPM.

3.2. PURE OXIDE CHARACTERIZATION

Preliminary characterization of pure solid oxide candidates listed in Table 2.2 was carried out using the various test systems. Measurement data was used to identify the short comings of various oxides and to carry out a down select of the potential candidates for further developmental.

3.2.1. Manganese Oxide

The two manganese oxide transitions of interest are $MnO_2 \leftrightarrow Mn_2O_3$ and $Mn_2O_3 \leftrightarrow Mn_3O_4$. TGA measurements showed decomposition of MnO_2 and Mn_2O_3 took place readily when the oxide was heated above the equilibrium temperature. In contrast, re-oxidation did not proceed as easily upon cooling. There is no observable re-oxidation of Mn_2O_3 into MnO_2 after the first reduction cycle [Fig. 3.5(a)]. Cyclic TGA measurements revealed extremely minor weight gains and losses thereafter [Fig. 3.5(b)]. This indicates that re-oxidation took place in only a very small fraction of the oxide. Surface analysis with XPS showed evidence of Mn^{2+} cations on the surface of Mn_2O_3 oxide particles. Hence, the observed weight gain in Fig. 3.5(b) could be the result of oxidation on Mn_2O_3 grain surfaces to form MnO_2. This suggests surface re-oxidation formed a barrier that prevented further reaction underneath similar to what was observed in pure cobalt and barium oxides. Once this layer formed, further oxygen diffusion into the lattice was stopped thus arresting $Mn_2O_3 \rightarrow MnO_2$ re-oxidation. A potential solution is to modify the surface structure to create stable oxygen diffusion paths for re-oxidation to continue.

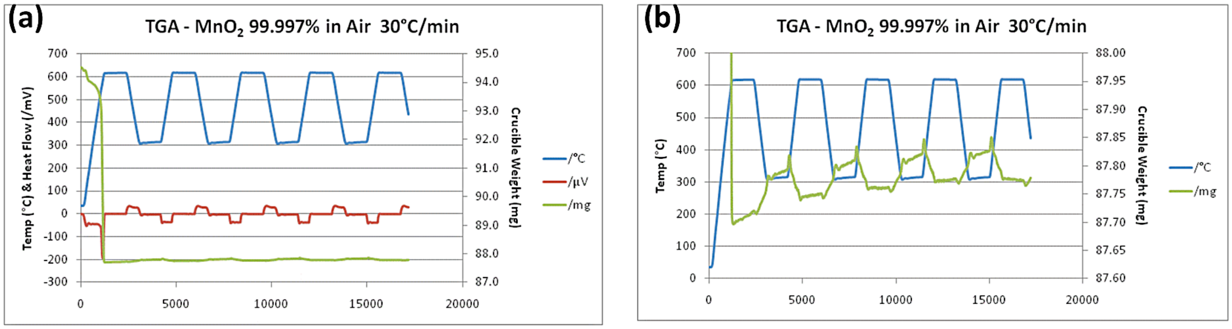

Fig. 3.5. TGA plots of a MnO_2 sample cycle between 300°C and 600°C.

The re-oxidation of Mn_3O_4 into Mn_2O_3 did proceed on a large scale but was slow (Fig. 3.6). A re-oxidation of 6% was recorded which was significantly less than cobalt oxide measured under similar conditions (see Fig. 3.7). The results showed the manganese oxide re-oxidation kinetics were slow and they must be enhanced if the manganese oxides are to be employed as a workable TES oxide.

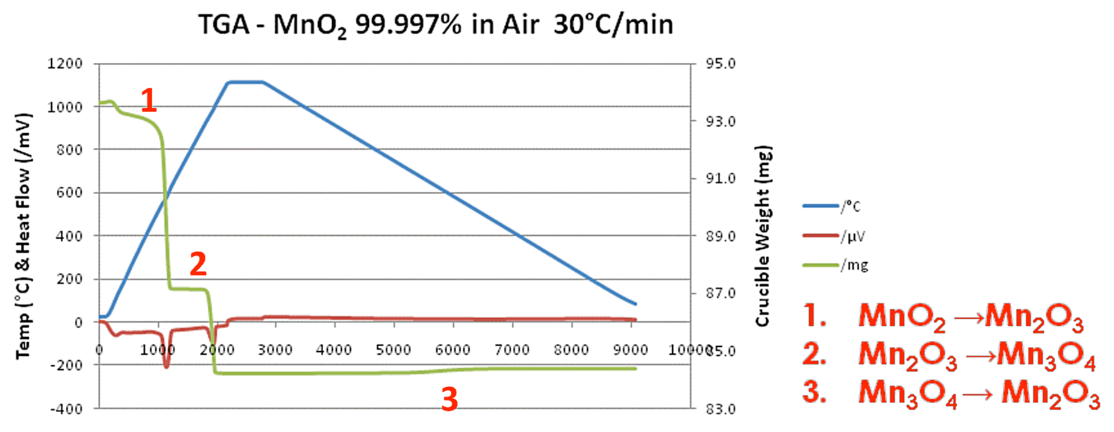

Fig. 3.6. TGA plot of a MnO_2 sample heated up to 1100°C and cooled down in air.

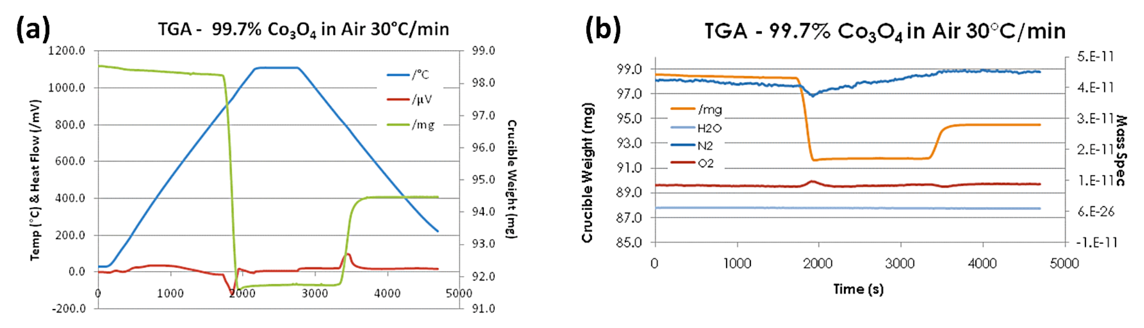

Fig. 3.7. (a) TGA plots of a Co_3O_4 sample heated up to 1100°C and cooled down in air. (b) the corresponding mass spectrometer signal of the carrier gas.

3.2.2. Cobalt Oxide

TGA measurements of cobalt oxide showed $Co_3O_4 \leftrightarrow CoO$ REDOX reactions took place readily. An endothermic valley, sample weight loss and oxygen release marked the decomposition of Co_3O_4 at around 860°C [Fig. 3.7(a)]. The reaction rate depends on the furnace heating rate but was complete well before the furnace reached 1000°C (Fig. 3.8). Upon cooling, re-oxidation took place accompanied by an exothermic peak, sample weight gain and oxygen uptake in the mass spectroscopy oxygen signal. The incomplete re-oxidation is due to the fast cooling rate (Table 3.1) which shows the importance of faster kinetics in such systems. The results showed that cobalt oxide is a viable TES candidate but pathways to improve the re-oxidation kinetics of pure cobalt oxide must be explored.

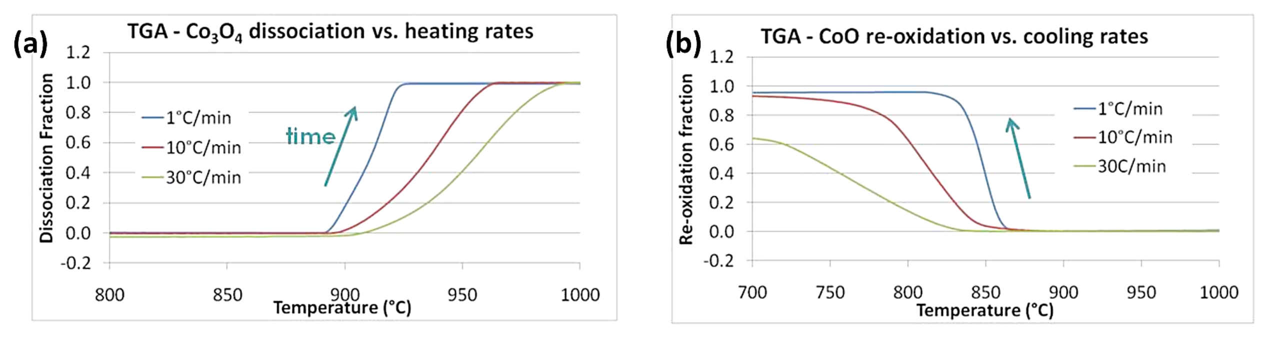

Fig. 3.8. Co_3O_4 (a) dissociation and (b) re-oxidation fractions as a function of temperature for heating rates between 1°C–30°C/min.

Table 3.1
Effect of Cooling Rates on Re-oxidation Fraction of CoO → Co_3O_4

Cooling Rate (°C/min)	Re-Oxidation %
1	94.6%
10	92.4%
30	69.0%

Since cobalt oxide was shown to be capable of undergoing full REDOX, it was used to verify the baseline packed bed TES concept in the laboratory and to study the discharge characteristics of a packed bed. Figure 3.9 shows the temperature profile of a cobalt oxide bed during one cycle of charge and discharge. The bed was reduced in nitrogen at 850°C and then cooled down to temperatures between 500°C to 700°C for re-oxidation. Once the bed had equilibrated at the lower re-oxidation temperature, the carrier gas was switched from nitrogen to air. The bed temperature began to rise as soon as air was introduced, prompted by the oxidation of CoO into Co_3O_4. The peak temperature, which represents the reaction front, travelled down the bed as the reaction proceeds through the oxide. The discharge took less than 2 hours and the bed temperature returned to the baseline once oxidation was complete. The amount of heat released was characterized by the integrated peak area. Results showed the total heat release to be a function of reduction and re-oxidation temperatures. Heat release leveled off with reduction temperature as complete reduction was achieved at around 900°C [Fig. 3.10(a)]. Higher reduction temperatures posed no additional benefits whereas at too low a reduction temperature e.g. 850°C, not all the oxide was reduced. This led to less stored energy and a lower total heat output during re-oxidation. Heat release was also measured as a function of re-oxidation temperature [Fig. 3.10(b)]. At the lower re-oxidation temperatures, the slower reaction kinetics led to slower heat release. Given a constant heat loss, the rise in bed temperature was less, which led to an apparently smaller total heat output. These experiments demonstrated that a packed bed TES reactor is feasible. The reduction and re-oxidation temperatures for the packed bed reactor will need to be carefully chosen in order to maximize the TES capacity of the system.

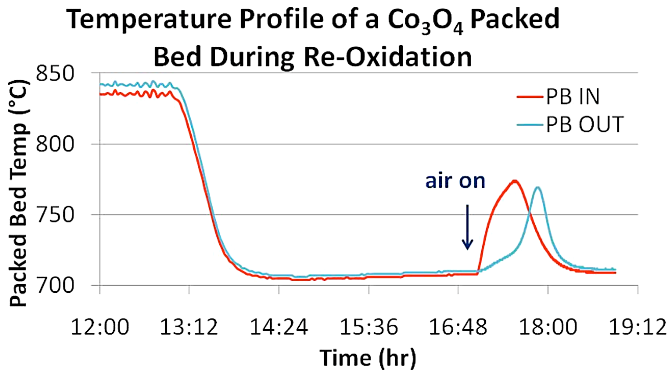

Fig. 3.9. The temperature profile of a cobalt oxide packed bed system during REDOX reaction. Heat is produced upon introduction of air and re-oxidation.

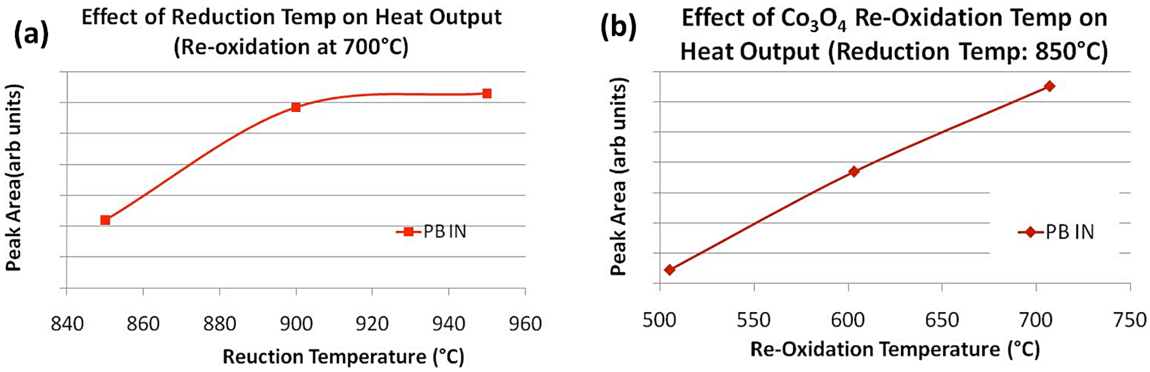

Fig. 3.10. The effect of (a) reduction (charging) and (b) re-oxidation (discharging) temperatures on magnitude of heat release (peak area) upon re-oxidation of a Co_3O_4 packed bed.

The effect of thermal cycling on the REDOX characteristics of cobalt oxide was investigated. Samples were cycled between 700°C and 900°C for a total of 500 cycles. Figure 3.11 shows the progression in the oxide's microstructure as a function of thermal cycling. Significant grain growth took place during the first 50 cycles as a fivefold increase in grain size was observed. Further cycling, up to 500 cycles, resulted in a more gradual increase in grain size. Re-oxidation, as measured by the TGA, was found to have improved despite the larger grains. Table 3.2 compares the re-oxidation fraction for the as-received sample and one that underwent 500 thermal REDOX cycles. The results were in contrast to the expected behavior, that a larger grain size reduces oxygen mass transport and leads to lower reaction kinetics. This cycled sample was characterized in an attempt to understand the reason for this improvement. XRD spectrum showed only Co_3O_4 diffraction peaks (Fig. 3.12); thus no secondary phase formed as a result of

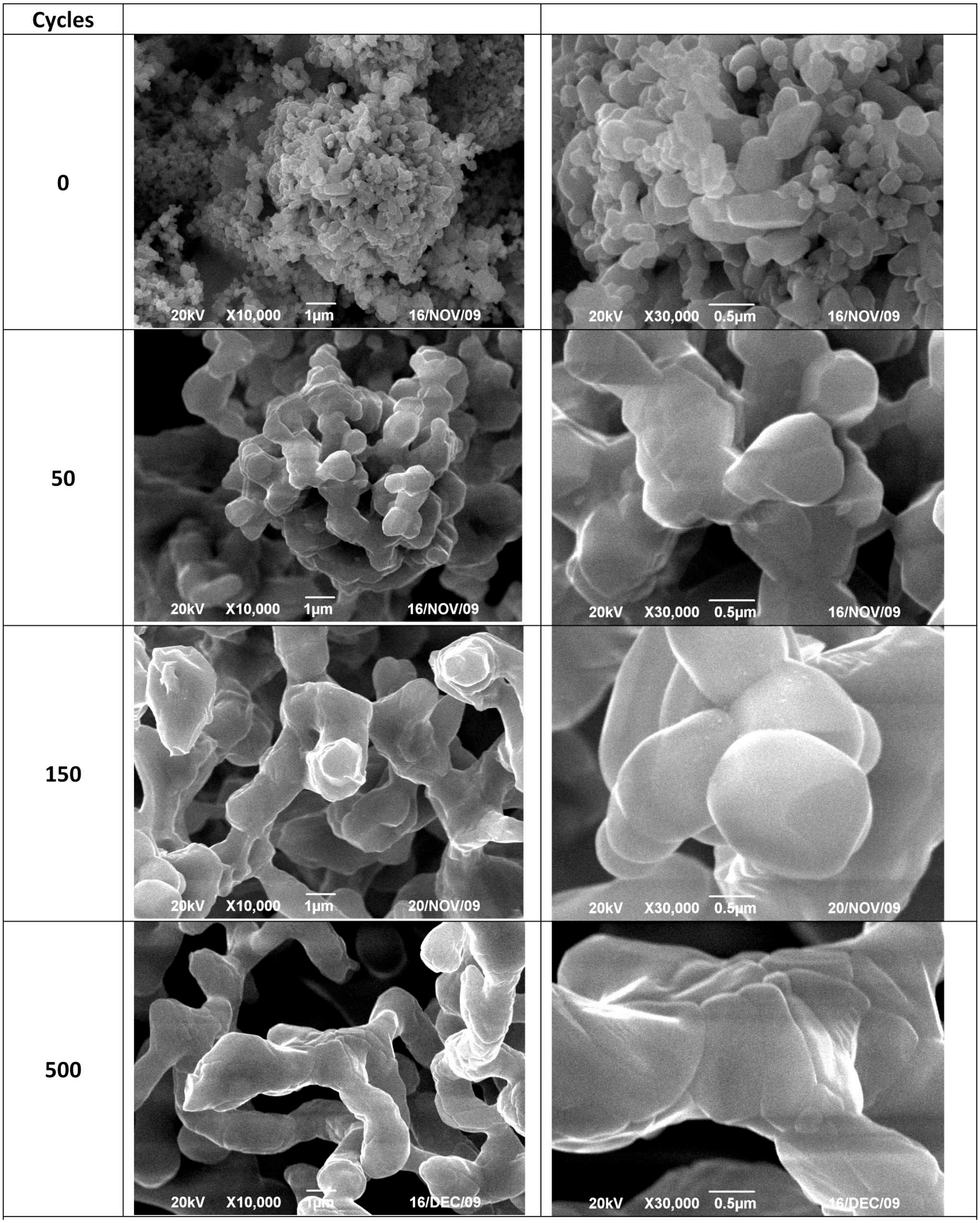

Fig. 3.11. Morphological evolution of a Co_3O_4 specimen that was cycled between 700°C and 900°C.

Table 3.2
Effect of TGA Cooling Rate on CoO→ Co_3O_4 Re-oxidation for as-Received Co_3O_4 and a Sample that has Undergone 500 Thermal Cycles

Cooling Rate (°C/min)	Re-Oxidation (1^{st} cycle)	Re-Oxidation (501^{st} cycle)
1	94.6%	100%*
10	92.3%	99.2%*
30	59.0%	93.7%*
10	92.3%	70.7%

*Sample with 0.5% Cr

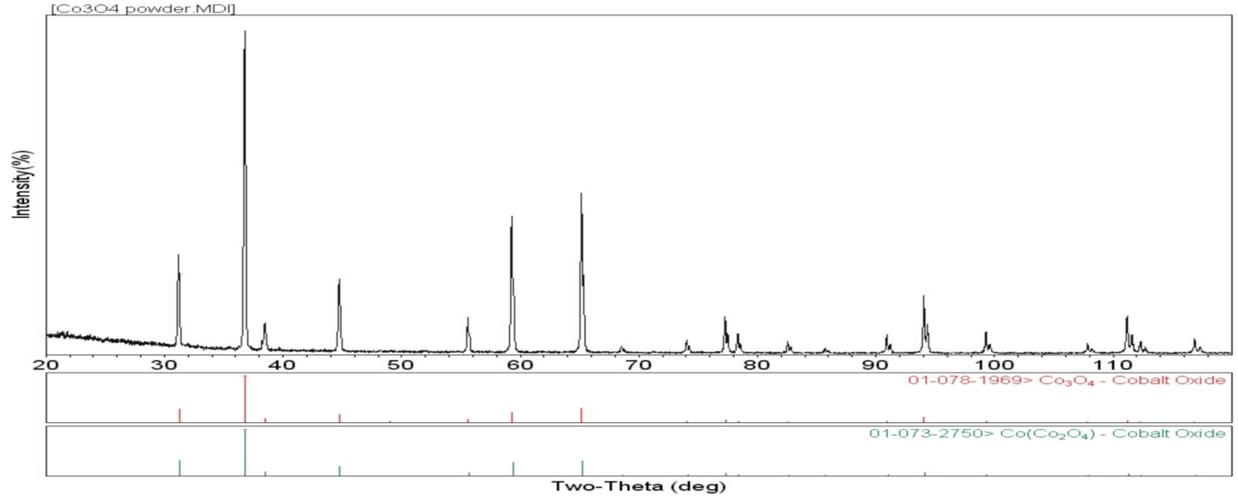

Fig. 3.12. XRD spectrum of cobalt oxide powder after 500 thermal REDOX cycles.

thermal cycling. The EDX spectra for an as-received and a cycled sample are shown in Fig. 3.13. A small amount of Cr (~0.5 at. %) was found in the latter. The added Cr must have originated from the cladding of the thermocouple embedded within the Co_3O_4 powder. The increase in re-oxidation was probably due to the mixed oxide doping effect discussed earlier. A repeated thermal cycling run showed the re-oxidation fraction decreased to around 70% in a sample which no chromium was detected. This shows that creating a mixed oxide is an effective approach to enhance the re-oxidation of TES oxide.

3.2.3. Copper Oxide

Copper oxides underwent the CuO ↔ Cu_2O REDOX reactions in air readily [Fig. 3.14(a)]. The REDOX behavior as measured by TGA is similar to that of Co_3O_4. An endothermic reduction reaction takes place during heat up followed by re-oxidation of the sample upon cooling. Post experimental observations showed the oxide sample has undergone sintering. This is due to the fact that the melting point of Cu_2O is only about 100°C above the maximum reaction temperature 1100°C. When the oxide was heated to a slightly higher temperature, the observed re-oxidation fraction was reduced [Fig. 3.14(b)]. This was because some of the oxide had melted and re-solidified. This greatly reduced the surface area available for the re-oxidation. It is impractical to operate a TES system when the equilibrium transition is so close to the melting point. Hence, copper oxide is not an appropriate TES oxide candidate.

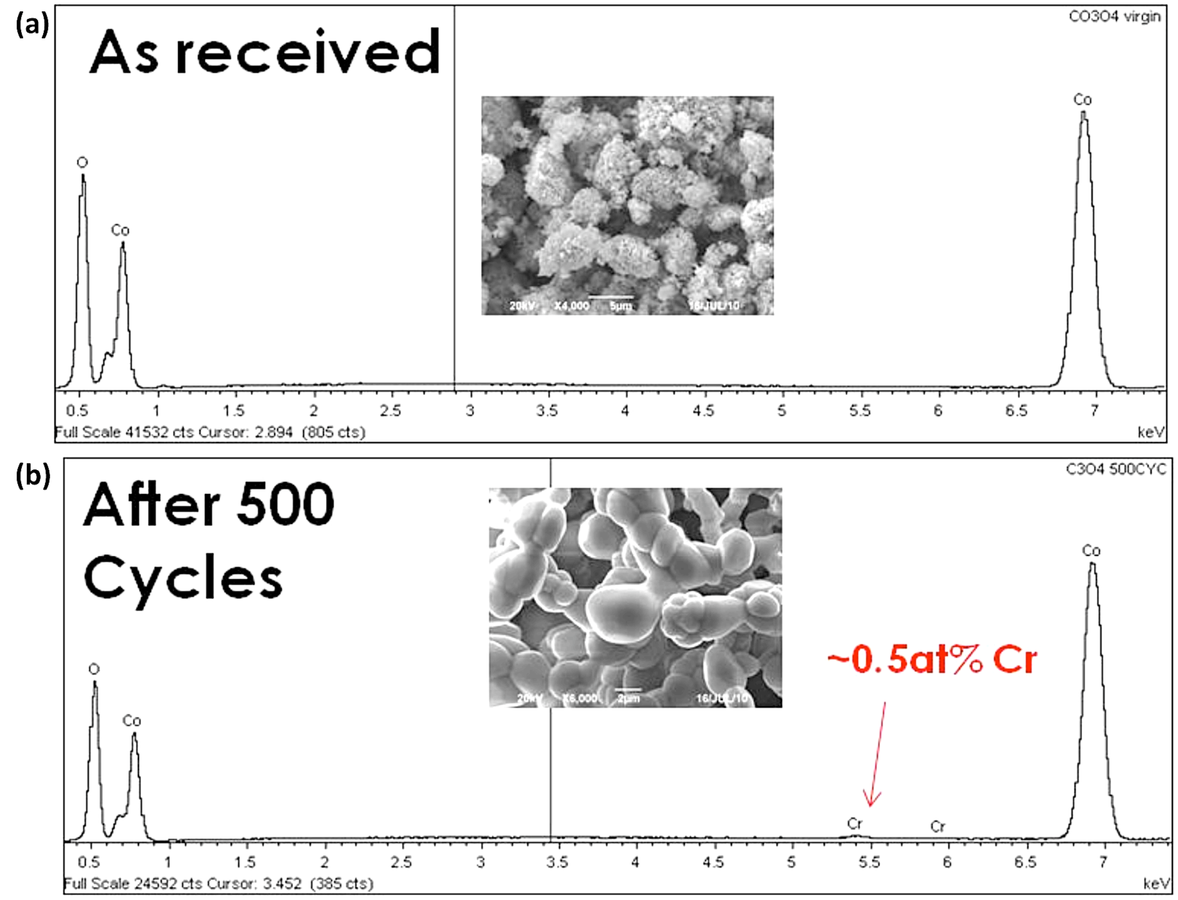

Fig. 3.13. EDX spectrum of Co_3O_4 powder (a) before and (b) after 500 thermal REDOX cycles.

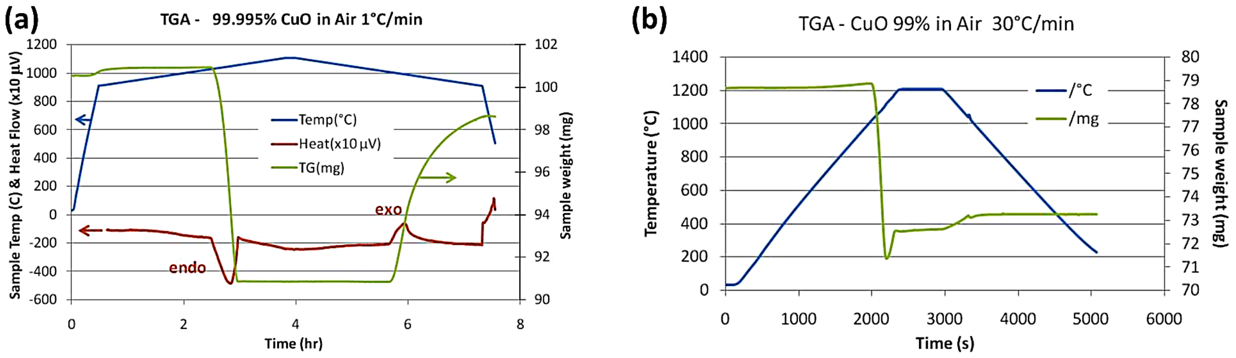

Fig. 3.14. TGA plots of CuO samples heated up to (a) 1100°C and (b) 1200°C and cooled down in air.

3.2.4. Antimony Oxide

TG analysis of Sb_2O_5 samples showed a gradual weight loss beginning at 100°C upon heating which could be a result of moisture evaporation (Fig. 3.15). However, this weight loss continued until 500°C indicating another reaction taking place in addition to evaporation. The total sample weight loss was 4.5%, which is close to the expected weight reduction (4.9%) for the $Sb_2O_5 \rightarrow Sb_2O_4$ transition. Upon cooling, there was no sample weight gain indicating that no re-oxidation was taking place. Similar behavior was observed in multiple samples at different heating and cooling rates. Since the reduction transition was not sharp and re-oxidation did not take place, antimony oxide is not a suitable TES candidate.

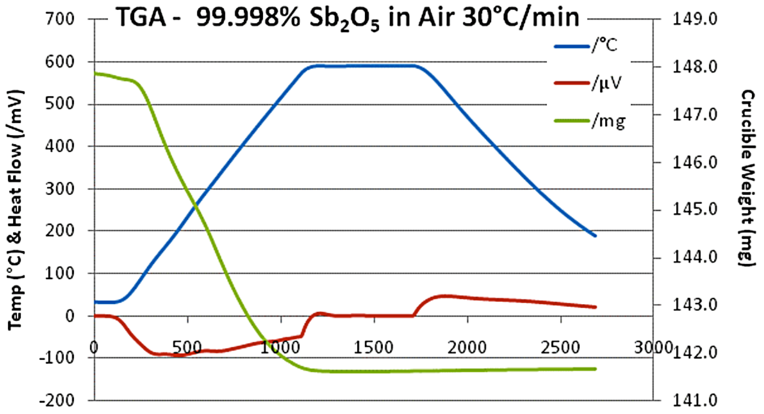

Fig. 3.15. TGA plot of a Sb_2O_5 sample heated up to 600°C and cooled down in air.

3.2.5. Lead Oxide

When PbO was studied with TGA (Fig. 3.16), a sample weight loss was registered at around 260°C. This is unexpected, as formation of all other lead oxide variants from PbO involves a weight gain. The decrease is about 0.3% which may simply be a result of degassing. Upon cooling, no re-oxidation could be detected as there was no weight gain in the specimen. This is most likely due to a combination of the slow kinetics and the existence of intermediate phases which made the REDOX transitions sluggish. Hence, PbO is not a suitable TES medium.

3.2.6. Barium Oxide

Barium oxide exhibited fast REDOX reactions during TG measurements. Figure 3.17(a) shows an oxidation-reduction cycle starting with the reduced BaO. Upon heating in air, it oxidized quickly and formed BaO_2. When the sample temperature reached around 600°C, reduction began to take place and BaO was reformed. Upon cooling, the re-oxidation fraction is significantly less that the first cycle. Repeated TGA thermal cycling showed the re-oxidation fraction remained low [Fig. 3.17(b)]. This could be due to morphological changes that affect the oxygen mass transfer. The use of barium based mixed oxides may be able to rectify this behavior. Hence, BaO was considered a potential TES candidate.

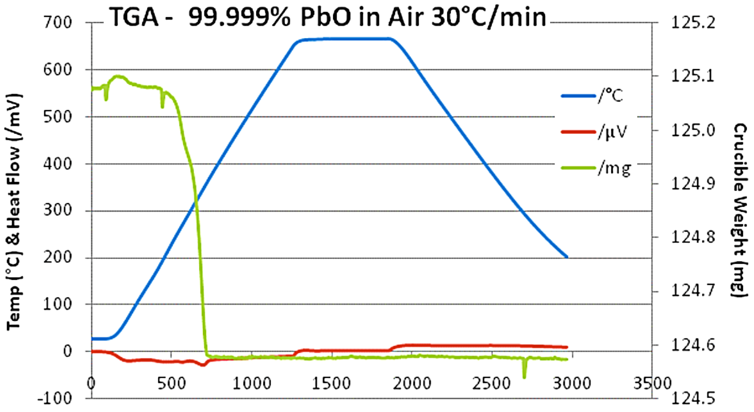

Fig. 3.16. TGA plot of a PbO sample heated up to 650°C and cooled down in air.

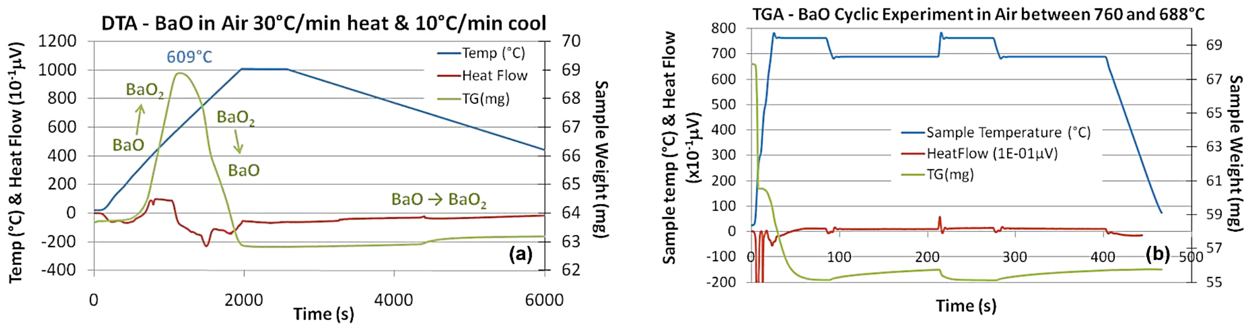

Fig. 3.17 TGA plots of BaO undergoing (a) one and (b) three thermal cycles.

3.3. Pure Oxide Down Select

A preliminary down select was carried out based on REDOX transition temperatures and materials costs and the list of potential TES oxide candidates was narrowed down to seven (Table 2.3). Among those Fe_2O_3 was eliminated due to attrition issues. The REDOX reactions of the remaining candidates were characterized in the laboratory. All oxides underwent reduction readily. Among them cobalt oxide demonstrated complete REDOX, storing and releasing heat in the process. Cobalt oxide was used as a model system to validate the proposed thermochemical heat storage concept in a packed bed reactor. Re-oxidation of the other six oxides did not go to completion due to slower reaction kinetics. Mn_3O_4 and BaO did re-oxidize, but the fraction was low. Kinetics improvements are needed in order for them to be usable. CuO showed good REDOX characteristics, but the low melting point of the reduced oxide makes this system impractical. For transitions that were known to have intermediate phases i.e. $MnO_2 \leftrightarrow Mn_2O_3$, $V_2O_5 \leftrightarrow V_2O_4$, $Sb_2O_5 \leftrightarrow Sb_2O_4$, no re-oxidation was observed. In the case of Mn_2O_3, it was proposed that surface re-oxidation retarded the reaction. The tendency for intermediate oxide formation in these systems must have acted to broaden the phase transition, which makes these oxide systems not suitable. Using preliminary experimental data and economic analyses, the project selected Co_3O_4, BaO_2 and Mn_2O_3 oxides for further developmental studies.

4. MIXED OXIDE REACTION KINETICS IMPROVEMENT

Co_3O_4, Mn_3O_4 and BaO_2 were selected for further development. Measurement results showed their re-oxidation kinetics would need to be increased for them to be used as TES media. The approach applied was to incorporate selected secondary oxides into the primary oxide so the primary cation is partially replaced by a secondary cation of different size and oxidation state. The lattice strain and charge imbalance created by the substitution should lead to an increase in vacancy density. Consequently, an enhancement in oxygen mass transfer through the lattice can be obtained giving rise to improved re-oxidation. Such an approach has been shown to increase electrical conductivity in ceramics. The following sections provide the key findings and results of the mixed oxide development process. More complete details on the various aspects of this work can be found in General Atomics reports GA-C27022 and GA-C27055.

4.1. MIXED OXIDE DEVELOPMENT

Mixed oxides can be produced via either mechanical alloying or wet chemistry methods. For large scale production, the former option is more straight forward to implement, thus it was chosen for our current development effort so large batches for future demonstration can be easily made. The mixing procedures that were developed are as follows:

1. Primary oxide (e.g. Co_3O_4) and secondary oxide powders (e.g. Fe_2O_3) with predetermined fractions were transferred into a polyimide container.
2. Tungsten carbide or stainless steel pellets were added to the powder mixture to boost mechanical mixing. The total powder to pellet weight ratio is 3:1.
3. The container was then placed on a roller for 100 hours for the powders to mix.
4. The mixed powder was annealed in air at 900°C for 100 hours or more.

The reproducibility of the mixing procedure was verified. Different samples of MnO_2-5%Fe_2O_3 were made using the above procedure. The samples have essentially identical TGA curves and their re-oxidation fraction was between 34 and 36% respectively. The effect of annealing time was also studied using the same MnO_2-5%Fe_2O_3 composition. An increase in annealing time from 100 to 275 hours did not lead to any increase in re-oxidation (Table 4.1). This indicates that an annealing time of 100 is sufficient to homogenize the MnO_2-Fe_2O_3 mixed oxides.

Table 4.1
Effect of Annealing Time on Mn_3O_4 Re-oxidation in a MnO_2-5%Fe_2O_3 Samples

Annealing (hr)	Re-oxidation (%)
100	34.0
150	34.2
275	34.0

4.2.1. Manganese Oxide

A number of transition metal oxides have been incorporated into manganese oxide. It was found that iron oxide was most effective in enhancing $Mn_3O_4 \rightarrow Mn_2O_3$ re-oxidation kinetics. The re-oxidation fraction increased by almost 20 fold (6% to 100%) when iron oxide was added (Fig. 4.1). The optimal composition was found to be around 10 at% (MnO_2-10%Fe_2O_3) (Fig. 4.2). Multiple specimens centered on this composition had been made and they all had a re-oxidation fraction between 90 to 100%. However, long term REDOX performance must be taken into account when choosing the final optimal composition.

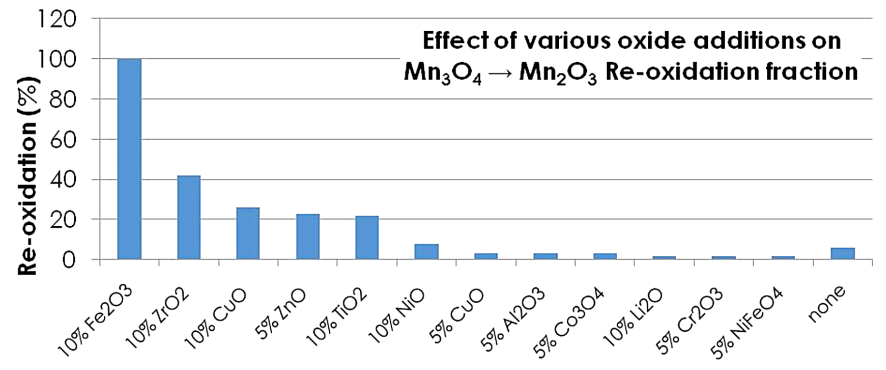

Fig. 4.1 Effect of various secondary oxide additions on $Mn_3O_4 \rightarrow Mn_2O_3$ re-oxidation fraction. Data *measured at a cooling rate of 10°C/min in air.

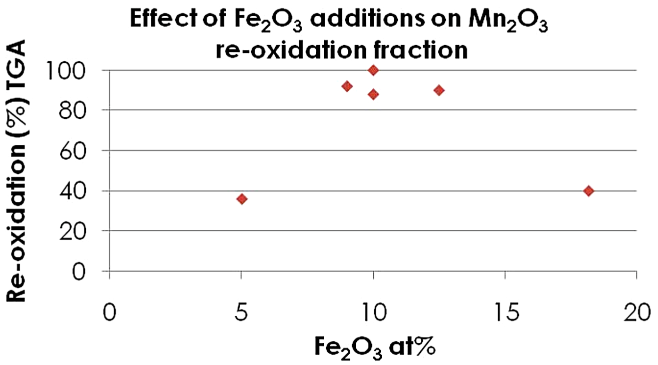

Fig. 4.2. Effect of Fe_2O_3 additions on $Mn_3O_4 \rightarrow Mn_2O_3$ re-oxidation fraction.

The charge-discharge characteristic of MnO_2-10%Fe_2O_3 in the packed bed was investigated using the set up described in Chapter 3. The equilibrium transition temperature is around 950°C. The oxide was reduced in nitrogen and the temperature was lowered to the re-oxidation temperature. Re-oxidation began as soon as air replaced the nitrogen as the carrier gas. Bed temperature rose as the reaction front traveled down the bed, as shown in Fig. 4.3, similar to what was observed with a pure cobalt oxide packed bed. However, it took almost 8 hours to complete the discharge, which indicates the kinetics are slower than cobalt oxide. Whether this is sufficient for the manganese-iron oxide to function in a TES reactor i.e. charging and discharging in 8 and 16 hours respectively, will be determined by applying the measured kinetics to a reactor model.

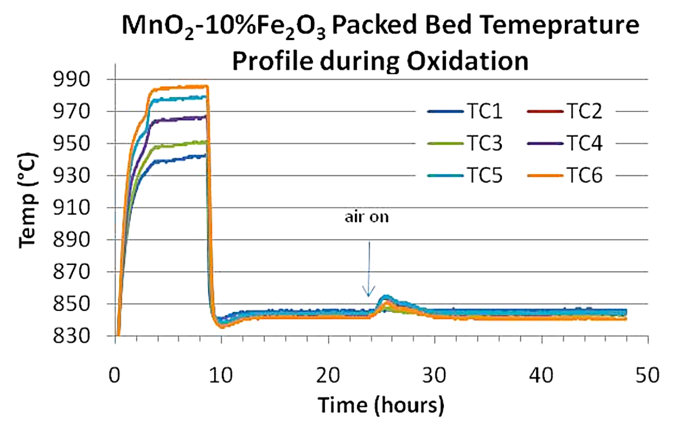

Fig. 4.3. Temperature profiles of a MnO_2-10%Fe_2O_3 packed bed within a charging and discharging cycle.

To assess the long term REDOX performance of manganese-iron mixed oxides, samples with various iron oxide compositions were put through 500 thermal cycles in the cyclic system. The physical structures of the post cycled specimens are shown in Fig. 4.4. When the iron oxide content is too low, a dense sintered structure resulted after cycling, similar to what had been observed in pure manganese oxide. For samples with 10 and 15% Fe_2O_3, re-crystallization had taken place and the overall grain size had actually reduced.

REDOX characteristics for cycled pure and mixed manganese oxides specimens were studied with TGA. A cycled pure manganese oxide underwent the $Mn_2O_3 \rightarrow Mn_3O_4$ reduction but very little re-oxidation was observed in the first TGA run (Fig. 4.5). The absence of re-oxidation is due to slow kinetics caused by the sintered grain structure. A subsequent repeat run showed very little reduction due to incomplete re-oxidation from the first run. On the other hand, the REDOX fraction, especially the magnitude of weight reduction, of a MnO_2-15%Fe_2O_3 specimen improved during thermal cycling [Fig. 4.5(b)]. This can be attributed to iron oxide additions which increased oxygen diffusivity and controlled the grain size. To compare the REDOX properties of various samples, *relative TES capacity* and *normalized reduction* were established to determine the effectiveness of the oxide additions and effect of thermal cycling.

$$\text{Normalized Reducation} = \frac{\%\ \text{measured weight loss}}{\%\ \text{theoretical weight loss}}$$

$$\text{Relative TES Capacity } = \left(\%\ \text{re-oxidation weight gain}\right)\ \text{X}\ \left(\text{Normalized weight loss}\right)$$

Composition	As Processed	After 500 thermal cycles
MnO_2-5%Fe_2O_3	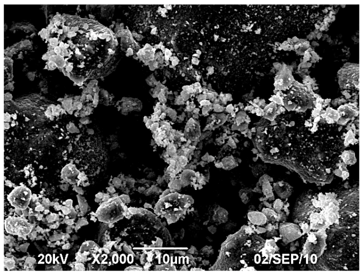	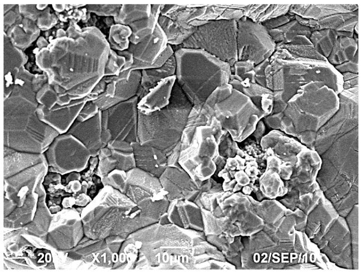
MnO_2-10%Fe_2O_3	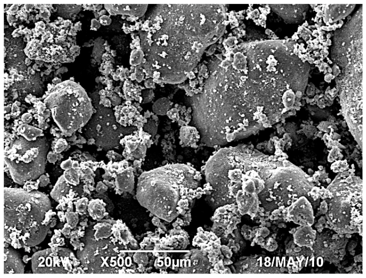	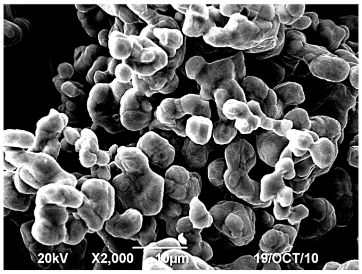
MnO_2-15%Fe_2O_3	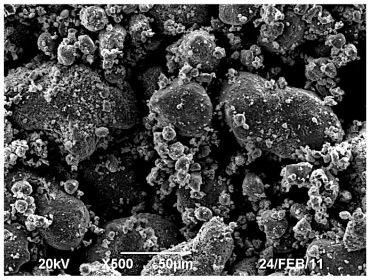	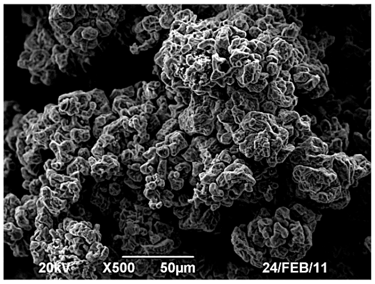

Fig. 4.4 Microstructures of manganese-mixed oxide in the as-processed and post thermal cycling states.

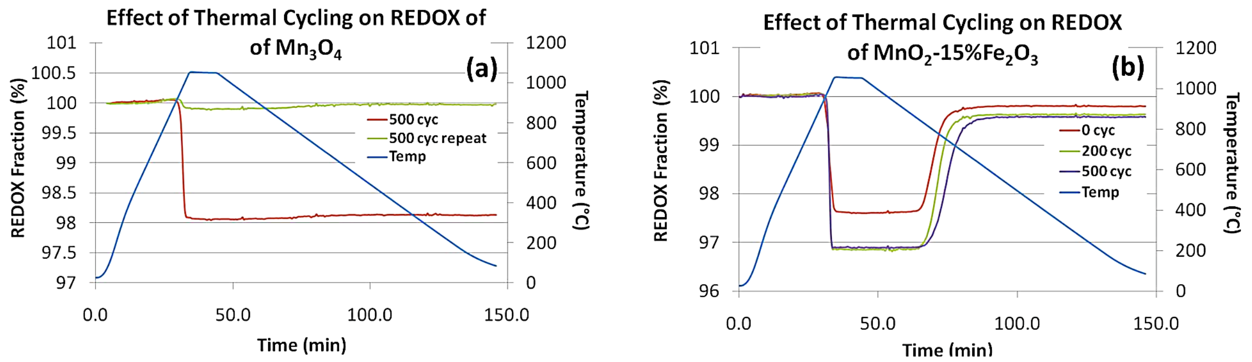

Fig. 4.5. TGA plots of (a) pure manganese oxide and (b) MnO_2-15%Fe_2O_3 samples that underwent 500 thermal cycles.

The effect of thermal cycling on these two parameters for manganese-iron mixed oxides of different compositions is shown in Fig. 4.6. Both values increased with thermal cycling i.e. the REODX properties of manganese-iron mixed oxides had actually improved. In samples with 15 and 20%Fe_2O_3, normalized reduction had increased to over 90% which is higher than that measured in a pure virgin manganese oxide sample. This enhancement could be partially due to a finer grain size. From these results, the optimal short and long term REDOX performance can be obtained at an iron oxide composition of about 15%. In all the manganese mixed oxide TGA runs, no weight increase was observed under 500°C, thus no $Mn_2O_3 \rightarrow MnO_2$ re-oxidation took place. Hence, the use of mixed oxides was not able to advance this reaction and MnO_2 can be eliminated from further consideration.

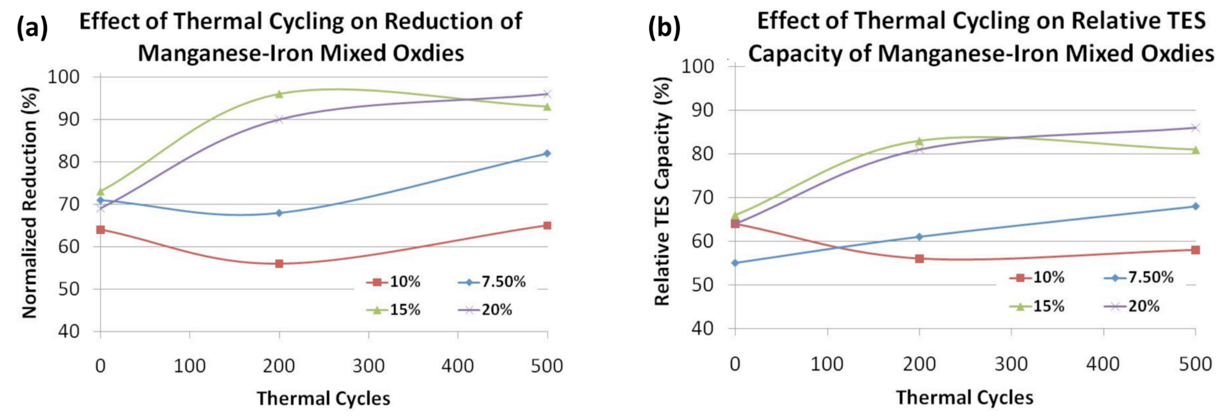

Fig. 4.6 (a) Normalized reduction fraction and (b) relative TES capacity of various manganese-iron mixed oxides.

4.2.2. Cobalt Oxide

The re-oxidation kinetics of cobalt oxide were improved through the incorporation of secondary oxides. It was found that Al_2O_3, Cr_2O_3, Fe_2O_3 additions were all effective in boosting the re-oxidation fraction in the as processed samples compared to pure cobalt oxide (Fig. 4.7). However, as the secondary oxide fraction increased, the magnitude of weight reduction decreased. This is because some of the active cobalt cations were replaced by inactive secondary cations. Hence, to maintain the mixed oxide's TES capacity, the amount of secondary oxide needs to be minimized. Table 4.2 lists the respective secondary oxide composition which gave the maximum re-oxidation fractions. The most favorable composition based solely on re-oxidation is 5 at. %Al but one must consider the long term REDOX performance before settling on an optimal composition.

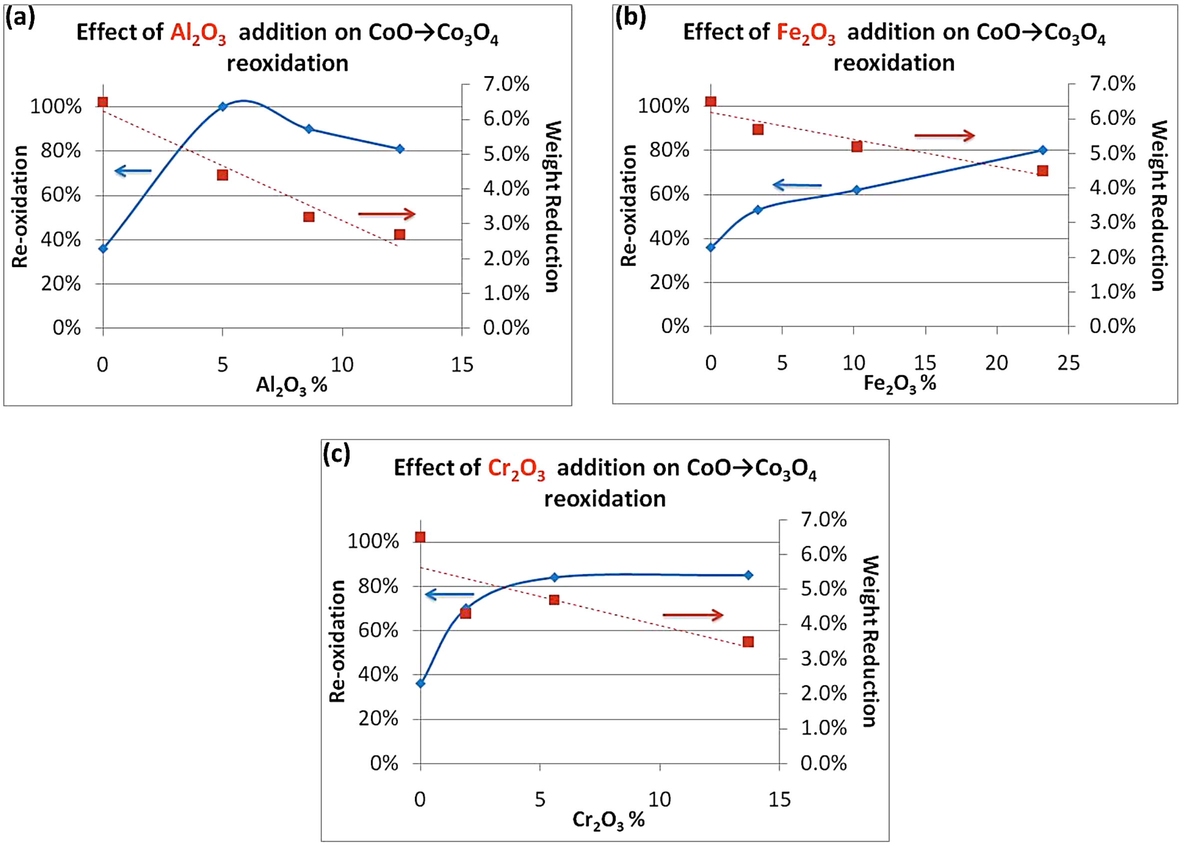

Fig. 4.7. The effect of (a) Al_2O_3, (b) Cr_2O_3 and (c) Fe_2O_3 additions on $CoO \rightarrow Co_3O_4$ re-oxidation.

Table 4.2
Maximum $CoO \rightarrow Co_3O_4$ Re-oxidation Fraction for
Various Cobalt Mixed Oxides

Mixed Co-Oxide	Re-oxidation*
5.0%Al_2O_3	100%
23.2%Fe_2O_3	81%
5.6%Cr_2O_3	84%
none	36%

*Measured at a cooling rate of 30°C/min in air.

Cobalt based mixed oxide samples were subjected to 500 thermal cycles. The microstructures of selected samples are shown in Fig. 4.8. The main noticeable difference is the grain size of the mixed oxides. Secondary oxide additions helped to limit grain growth. In addition, mixed cobalt oxides exhibited less electrostatic charging in the SEM. This indicated that their conductivities were higher which stemmed from an increased defect density.

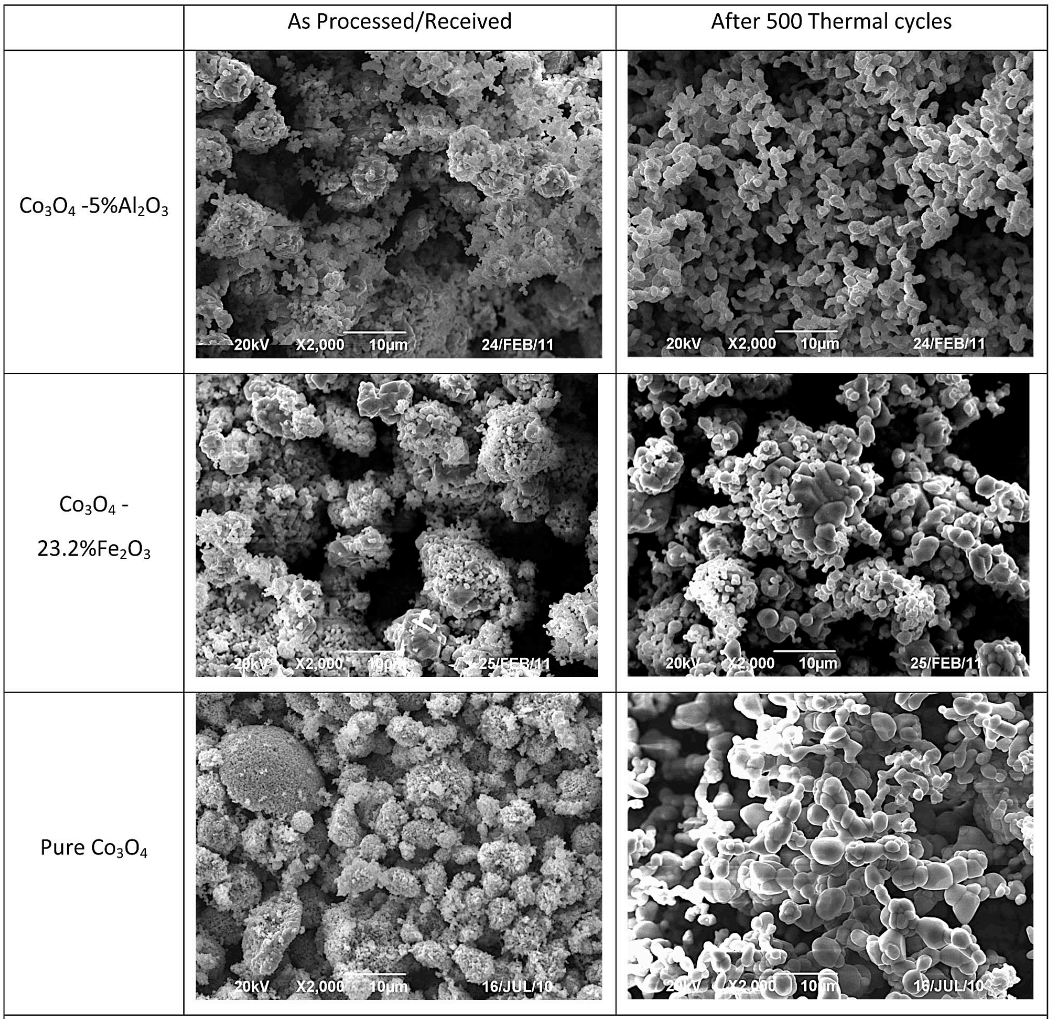

Fig. 4.8. Microstructures of pure cobalt, cobalt-iron and cobalt-aluminum mixed oxides before and after 500 thermal cycles.

The TGA plot of a Co_3O_4 -5%Al_2O_3 mixed oxide sample revealed an improvement in REDOX properties after cycling [Fig. 4.9(a)]. Similar to that observed in the manganese-iron mixed oxides, the magnitude of reduction had increased after thermal cycling. However, this improvement is in contrast to pure cobalt oxide and other cobalt-aluminum mixed oxide samples which all experienced a reduction in both normalized reduction fraction and relative TES capacity after thermal cycling (Fig. 4.10). The results showed that the cobalt-aluminum oxide composition needs to remain in a tight composition range for optimal short and long term REDOX performance. Similar post thermal cycling reduction was observed in some cobalt-iron and cobalt-chromium mixed oxide samples (Figs. 4.11 and 4.12). An exception is the mixed oxide sample with 23.2%%Fe_2O_3. The REDOX properties as measured by TGA were very stable throughout the thermal cycling process [Fig. 4.9(b)]. The cycled samples of Co_3O_4-5%Al_2O_3 and Co_3O_4-23.2%Fe_2O_3 have similar REDOX performance and TES capacity of almost 60%. Given the stable REDOX properties of Co_3O_4-23.2%Fe_2O_3, it is certainly a better choice for baseline bench top demonstration testing if the measured data is confirmed. Using Fe_2O_3 has an added advantage in that the high iron oxide content reduces the fraction of the more expensive cobalt oxide. This will decrease the overall storage and LCOE costs.

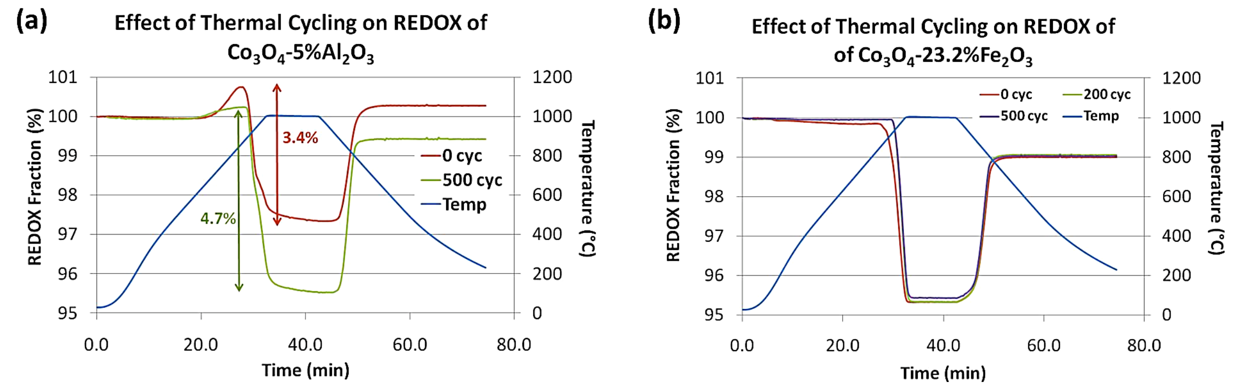

Fig. 4.9. TGA plot of (a) Co_3O_4 -5%Al_2O_3 and (b) Co_3O_4 -23.2%Fe_2O_3 samples that underwent 500 thermal cycles.

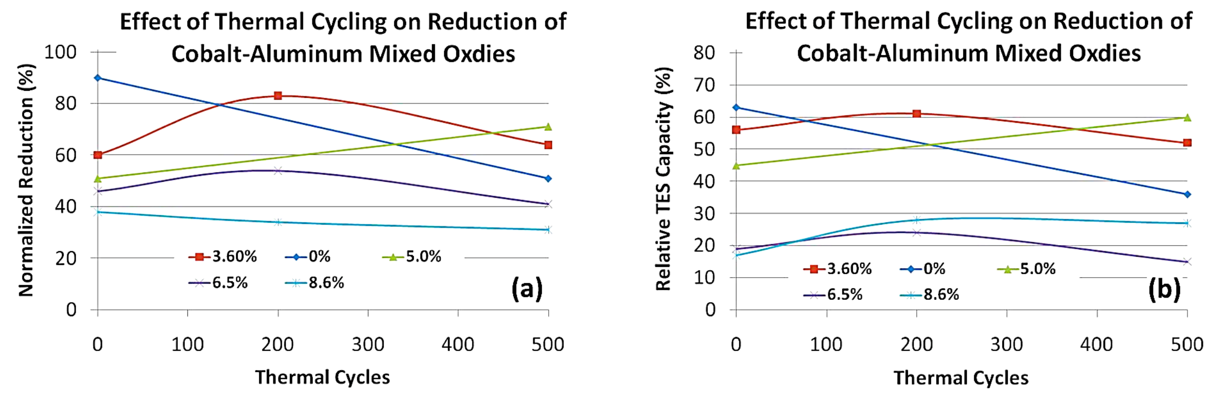

Fig. 4.10. (a) Normalized reduction fraction and (b) relative TES capacity of pure cobalt oxide and various cobalt-aluminum mixed oxides.

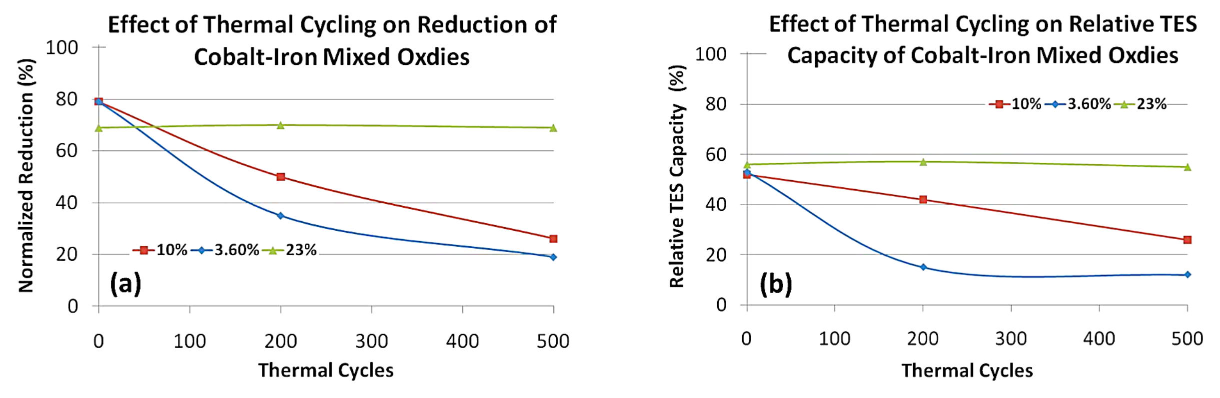

Fig. 4.11. (a) Normalized reduction fraction and (b) relative TES capacity of various cobalt-iron mixed oxides.

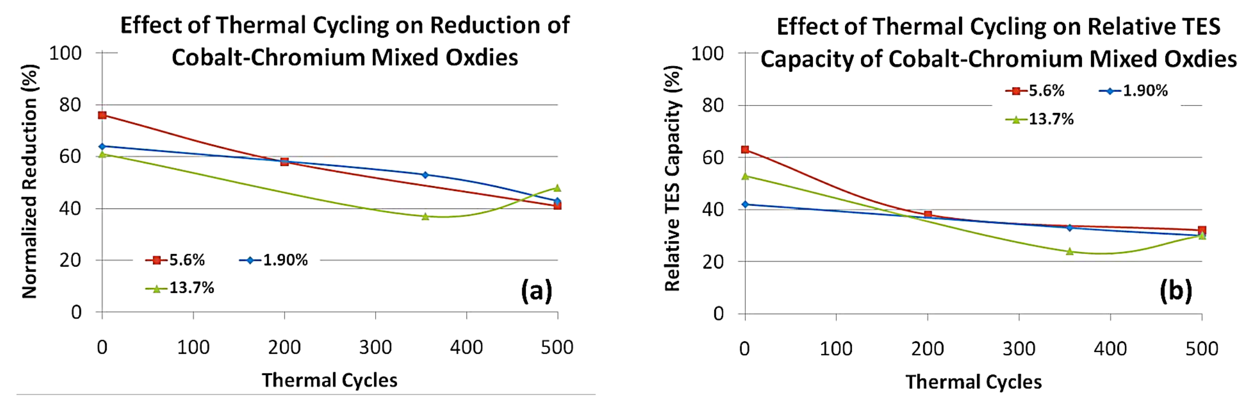

Fig. 4.12. (a) Normalized reduction fraction and (b) relative TES capacity of various cobalt-chromium mixed oxides.

The REDOX stability of Co_3O_4-5%Al_2O_3 oxide was also tested in the rotary kiln reactor described in Section 3.3.4. Figure 4.13(a) shows the temperature and oxygen concentration within the reactor during multiple REDOX operations in one test. A complete reduction and re-oxidation cycle took essentially 50 minutes, which is significantly faster than the bench top packed bed. This is due to a much higher heat transfer rate in a moving bed reactor. Figure 4.13(b) shows the variation in measured oxygen signal over a period of 6 days (30 runs). The oxygen concentration was used to determine the degree of oxide reduction with respect to theoretical. The REDOX capacity of cobalt-aluminum oxide ranged between 45 to 50% of the theoretical value and it did not decline with cycling. This shows that the mixed oxide property is stable and the rotary kiln is a viable approach to carry out the charge and discharge of TES oxide. Details of this work will be published in a paper by DLR.

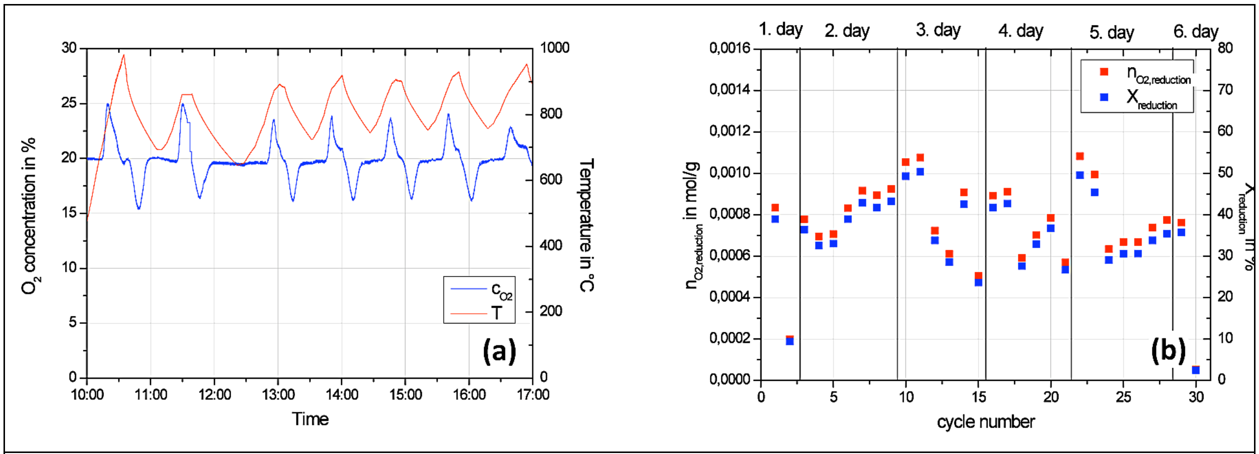

Fig. 4.13. (a) Oxygen concentration and rotary kiln temperature profile during repeated runs in one day. (b) Specific amount of oxygen and the conversion during oxide reduction.

4.2.3. Barium Mixed Oxides

A number of secondary oxides were mixed with barium oxide in an attempt to improve the REDOX properties, especially after the first thermal cycle. Additions included NiO, TiO_2, Fe_2O_3, SnO and ZnO. Furthermore, commercially available $BaTiO_3$ and $BaCuO_x$ mixed oxides were also tested. Unlike manganese and cobalt oxides, the incorporation of a secondary oxide did not lead to any improvement in the REDOX properties and stability. Figure 4.14 shows a typical TGA curve for the as processed barium based mixed oxides. The sample underwent reduction but the re-oxidation fraction is very low. This could be related to the chemical stability of barium oxide. Hence, this family of oxides is not suitable for TES.

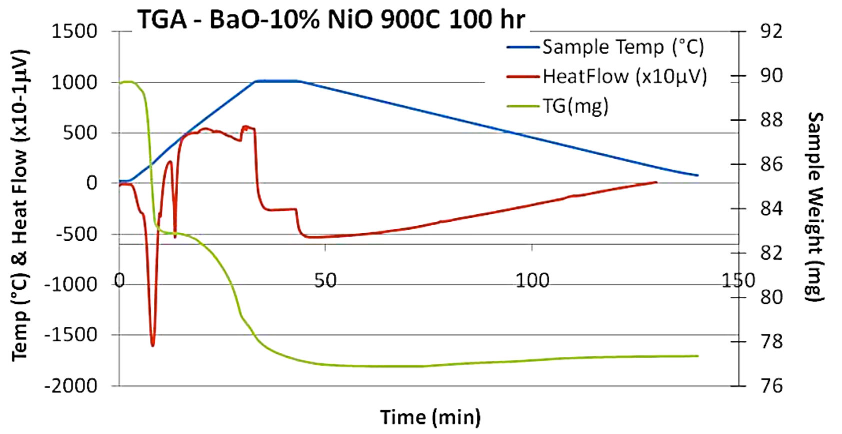

Fig. 4.14. TGA plot for a BaO-10%NiO mixed oxide.

5. MATERIALS COMPATIBILITY STUDIES SUMMARY

To integrate the TES concept into a solar plant, the reactor that holds the solid oxide will need to be constructed using proper engineering materials. In addition to containment, this will enable the reactor to operate at above ambient pressure. This reduces the volume of heat transfer fluid that needs to be cycled through the system and can also lead to faster re-oxidation due to a higher oxygen partial pressure.

The compatibility of common high temperature construction materials with manganese-iron and cobalt-aluminum mixed oxides was investigated using the thermal cyclic test systems. Coupons of selected materials were subjected to thermal cycling while they were in contact with the two oxides. This simulated the prototypical TES operating conditions and a total of 500 thermal test cycles were carried out. Details of the test results can be found in General Atomics report GA-C27024.

Reactions have been observed between the metal samples and the oxides, and they varied from simple discoloration to severe dissolution (Fig. 5.1). Sample-oxide interactions can be broken down into four different categories. First are those that show a great deal of reaction, resulting in severe dissolution, spalling or an extremely rough sample surface. The second group includes samples that have reaction induced relatively rough surfaces which also caused cracks on the surface. The third group of materials also showed surface roughening but no cracks were found. The last group is those that developed minor interaction related surface roughness with no cracks. All the samples that were tested exhibited reaction with the oxides, but the extent varied. Table 5.1 summarizes that compatibility between the selected candidates and the two oxides. Only Inconel 625 is compatible with both mixed oxides. It can thus be used to construct a packed bed reactor for bench top testing when the results are re-confirmed.

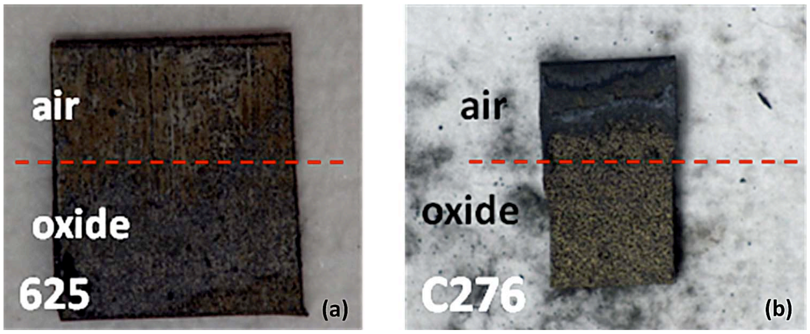

Fig. 5.1. (a) An Inconel 625 coupon and (b) a Hastelloy C276 coupon that were embedded in MnO_2-10%Fe_2O_3. and Co_3O_4-5%Al_2O_3 respectively during thermal cyclic testing.

Table 5.1
Summary of Materials Compatibility Test Results for Various TES Solid Oxides

Alloy	MnO_2-10%Fe_2O_3	Co_3O_4-5%Al_2O_3
SS 321	Fair	Poor
SS 309	Fair	Poor
SS 4340	Poor	-
253 MA	Poor	Fair
Inconel 718	Fair	Fair
9Cr- 1Mo	Poor	Poor
800H	Fair	Fair
Inconel 600	Fair	Fair
Inconel 625	Excellent	Good
Hastelloy B3	Good	Poor
Hastelloy C276	Good	Poor

Poor: moderate to serve dissolution.
Fair: very rough surface or surface cracks observed (not suitable for pressure vessel use).
Good: rough surface but no surface cracks found.
Excellent: relatively smooth surface with minimal reaction and no cracks.

6. KINETICS DATA MEASUREMENT AND PRELIMINARY REACTOR MODELING

To assess the performance of a solid oxide packed bed TES reactor, a reactor model was established. The model can determine the influences of various materials and process parameters on charging and discharging of the reactor. The first step in the process was to derive reaction rate equations based on measured oxide kinetics using TGA. These equations were then applied to the reactor model with preset boundary conditions. The performance of the reactor can then be investigated and a system design can be derived. Details of the kinetics measurements and modeling work can be found in Appendix A of this report and General Atomics report GA-C26524-MAR2010 1Q.

6.1. KINETICS DATA MEASUREMENTS

TGA data was used to determine rate equations that govern the REDOX reaction kinetics. The results can then be used to define the mechanism based on the Avarami-Erofeev solid gas reaction model:

$$d\alpha/dt = A * \exp(E_a/RT) * f(\alpha) \tag{6-1}$$

α: decomposition/re-oxidation fraction

$f(\alpha)$: correction factor– reaction mechanism related

A: pre-exponential kinetics

E_a: activation energy

By fitting the measured fraction changes at different heating and cooling rates to the rate equation, the activation energy, the kinetics and the reduction reaction mechanisms can be determined. An example is shown in Fig. 6.1(a) which shows the decomposition fraction of cobalt oxide as a function of temperatures for four different heating rates. An Arrhenius plot was then obtained from the data set [Fig. 6.2(a)]. The slope of the line is E_a/R and the pre-exponential kinetics factor, A, can then be calculated. Similarly, by measuring the re-oxidation rate at various isothermal temperatures [Fig. 6.1(a)], the pre-exponential factor and the activation energy for re-oxidation can be derived from the corresponding Arrhenius plot [Fig. 6.2(b)]. It was found that the activation energy of the reduction step decreases as a result of iron oxide additions (Table 6.1). As expected, activation energy for the re-oxidation is significantly lower but the pre-exponential is also much smaller.

To determine the reaction mechanisms, $d\alpha/dT$ plots for different $f(\alpha)$ functions were calculated and compared with the measured data (Fig. 6.3). The most probable controlling mechanism can be decided based on least square fit between the measured and the modeled data set. It was concluded that both the reduction and re-oxidation process fits best with a 3D nucleation shrinking core model i.e. oxygen diffuses uniformly in and out of the matrix during oxidation and reduction. Hence, the improvement of mass transfer in the system is essential.

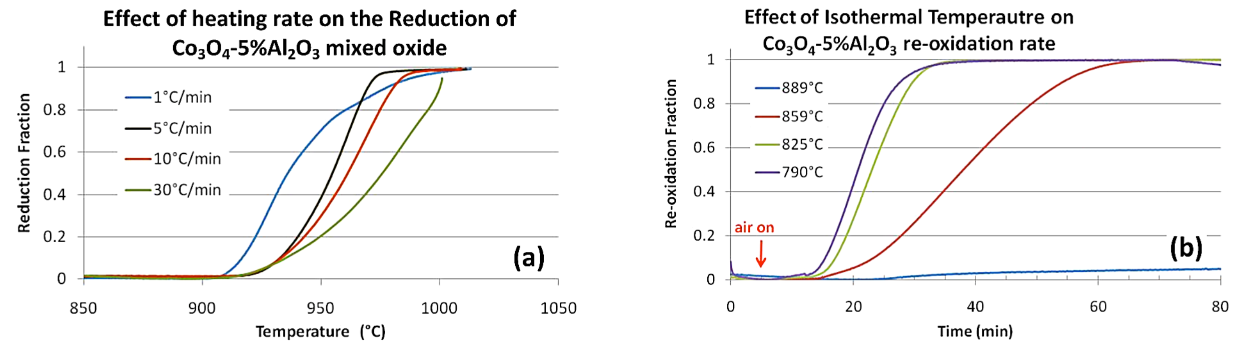

Fig. 6.1. Effect of (a) heating rate on the reduction and (b) isothermal temperature on the re-oxidation of Co_3O_4-5%Al_2O_3 mixed oxides.

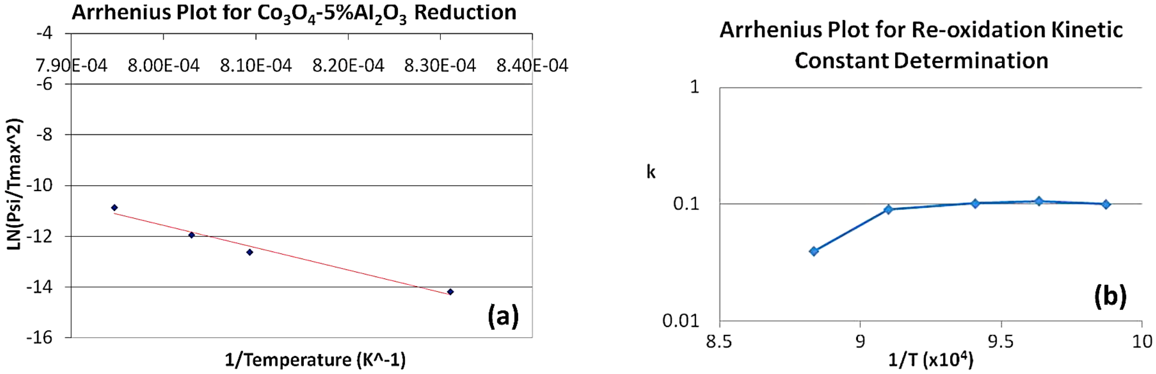

Fig. 6.2. Arrenhenius plot for Co_3O_4-5%Al_2O_3 (a) reduction and (b) re-oxidation reactions.

Table 6.1
Activation Energies and the Pre-exponential Factors Calculated for Pure Co_3O_4 and Co_3O_4-5%Al_2O_3 using TGA Measurement Data

	Pure Co_3O_4 (Dissociation)	w/ 5%Al_2O_3 (Dissociation)	w/ 5%Al_2O_3 (Re-oxidation)
Ea (kJ/mole)	960	731	165
A (s^{-1})	1.98E+39	1.01E+28	1.26E+09

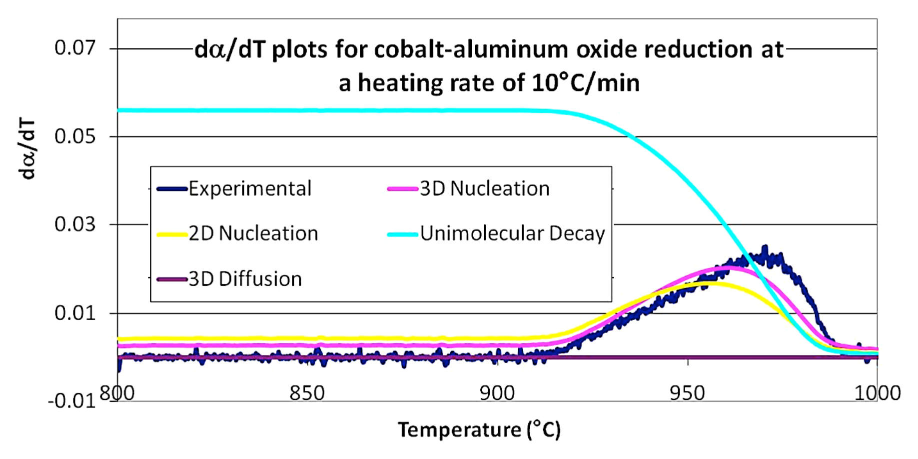

Fig. 6.3. dα/dT plots for Co_3O_4-5%Al_2O_3 reduction at a heating rate of 10°C/min.

6.2. REACTOR MODELING

For a thermochemical heat storage system utilizing a fixed bed reactor, the reactor design is a main concern. The final design has to provide an appropriate outlet air temperature and a specific power level. These are controlled by a numbers of operating parameters and inherent oxide properties. To arrive at an optimal fixed bed reactor design, it is best to study the sensitivity of oxide bed charge and discharge to the various input parameters using a reactor model (Fig. 6.4). The present fixed bed model incorporates a system of 1D partial differential equations coupled with preset initial and boundary conditions. These equations were solved numerically using Finite Element Methods (FEM) that are contained in the software COMSOL Multiphysics®. The results provided a spatial evolution of temperature, pressure and solid density within the fixed bed reactor over time. By applying the measured kinetics of pure cobalt and cobalt aluminum mixed oxides, the most effective reactor and system designs were defined. Their limitations and specific requirements were studied. The primary baseline process design targets an 8 hour charge time and up to 16 hours of discharge. The model investigated how various factors would affect this baseline assumption.

Using the established model, sensitivities of bed charging as a function of bed thermal conductivity and pre-exponential factor were studied. The baseline TES oxide properties values used are listed in Table 6.2. Full conversion was achieved within 8 hours when the baseline conductivity and pre-exponential factor of 1 W/mK and $A=1.98\cdot10^{39}$ 1/s were applied (Figs. 6.5 and 6.6). The outlet temperature was almost constant at the targeted design point of 890°C throughout the charging process and only started to increase after around 5 hours at around 60% conversion. Increasing the pre-exponential and the thermal conductivity resulted in a slight improvement. On the other hand, a decrease of both parameters led to a much longer charging period and charging could not be completed within the 8 hour window. Another consequence

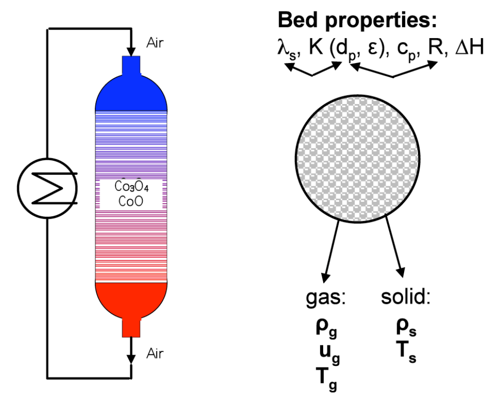

Fig. 6.4 The reactor concept with indirect heat transfer and its input and output parameters.

Table 6.2
Baseline Packed Bed Properties used for Reactor Modeling

Properties	Values
Density at end of discharge, ρss	6070 kg/m3
Density at end of charge, ρs0	5667 kg/m3
Porosity, εb	0.5
Porosity, εp	0.4
Specific heat, cpR	628+0.12*Ts J/kgK
Specific heat, cpO	328.6+0.55*Ts J/kgK
Particle thermal conductivity, λs	1 W/mK
Reaction heat of formation, ΔH	844 kJ/kgCo_3O_4
Reactor Dimension	Ø 7.4 m, L=5 m
Reactor Capacity	186 MWh reaction
Pressure Drop	Pin: 2.3 bar, Pout: 1 bar

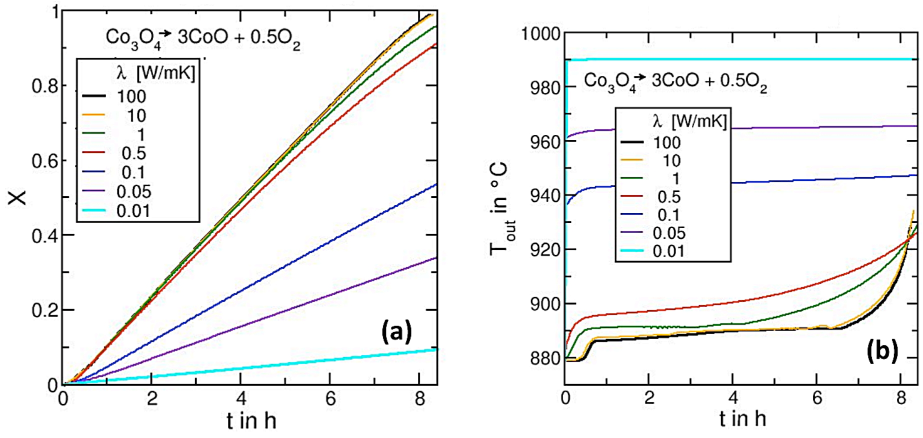

Fig. 6.5 Influence of thermal conductivity of solid particles on (a) conversion and (b) outlet temperatures.

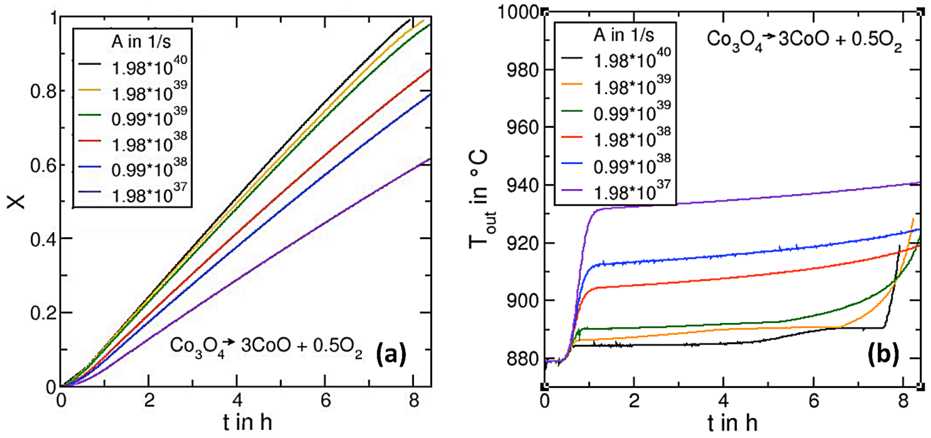

Fig. 6.6 Influence of pre-exponential factor on (a) conversion and (b) outlet temperatures.

of a lower thermal conductivity is its effect on the heat transfer coefficient and the heat transport to the fluid during re-oxidation. The transfer slowed down and the outlet temperature could not rise to the design target. Similarly, if the reaction rates were low, the reaction zone would be extended and outlet temperature would drop once this zone reached it. The results showed that with the assumed bed properties derived from measured kinetics and literature data, a promising power and temperature level could be achieved for the proposed system.

To study the efficiency of the charge/discharge process, new boundary conditions based on prototypical operations to minimize pressure drop were applied (Table 6.2). The bed properties used in the calculations are shown in Table 6.3. The goal is to identify conditions that limit the parasitic compression work (P_{cth}/P_{th}) to 20% of the system output. The effects of particle size, number of reactors and the inlet air temperature were studied.

Table 6.3
Process Parameters and Bed Properties used for TES Reactor Modeling

Capacity	Bed properties	Boundary conditions	Power
1200 MWh_{th}	Fixed bed $\varepsilon > 0.5$ $d_p < 0.1$ m	$P_{in,d}$: 0.95-0.9 bar $P_{in,r}$: 1 bar $T_{in,d}$: 1200°C-950°C $T_{in,r}$: 600°C	$P_d = 150\ MW_{th}$ $P_r = 75\text{-}600\ MW_{th}$ $P_{cth}/P_{th} < 20\%$

Figure 6.7 shows the effect of particle size and inlet temperature on parasitic load for a charging period of 8 hours. When the particle diameter is small, e.g. 1 cm, more than 20 reactors are needed for the parasitic load to stay below the 20% threshold. For large particles, only 10 or less tanks are needed to acquire the 1200 MWh_{th} thermal capacity needed (sensible heat was included in the calculations). In addition, a higher inlet temperature decreases the number of tanks required due to the lower required mass flow rate per tank. Based on these data, an inlet

temperature of 1200°C during charge is used. A design of 8 tanks (150 MW_{th} each) with a height of 4.45 m and diameter of 8.9 m containing metal oxide spheres of 3 cm particles is proposed for such storage system. The calculated losses due to the pressure drop are ~13% if 1200 MWh_{th} are transferred within 8 hours.

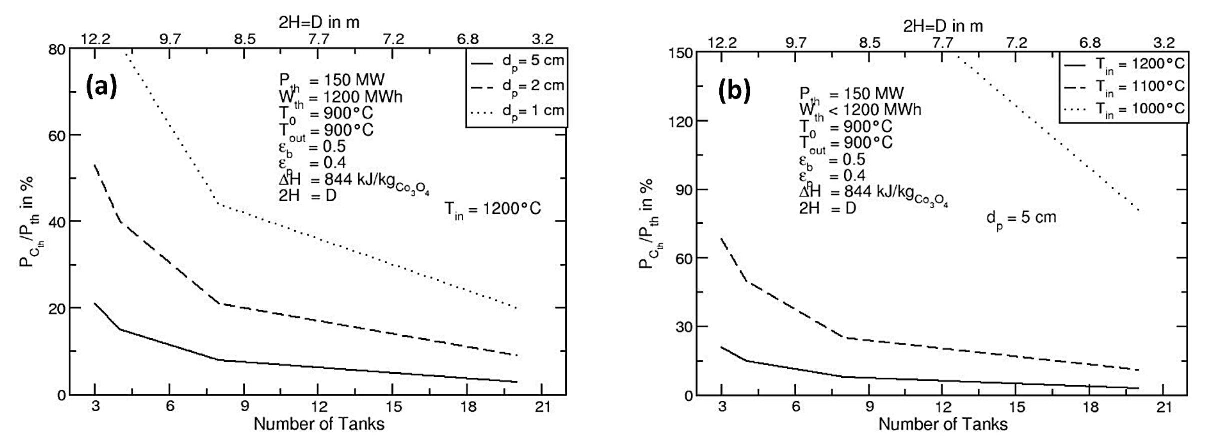

Fig. 6.7. Compression work during charge: $Co_3O_4 + \Delta H \rightarrow 3\ CoO + 0.5\ O_2$. (a) Influence of particle diameter and (b) inlet temperature.

For discharging, the power level needs to be adjusted according to electricity generation requirement. For example, at a power level of 150 MW_{th} a discharge time of 8 hours is available. Similarly for a 16 hour discharge, the power output can only be at 75 MW_{th}. The compression work for an eight tank system at different power output is shown in Fig. 6.8. For a required power level of 37.5 MW_{th} or 75 MW_{th} the parasitic losses exceed the requested 20%. Decreasing the inlet temperature (<600°C) or increasing the number of tanks is necessary to keep losses below the threshold. However, taking into account the charging requirements, it was determined that an 8 hour discharge time with a power output level of 18.75 MW_{th} is optimal. The baseline design for a 1200 MW_{th} TES system is listed in Table 6.4.

The overall capacity of this design depends on the sensible storage of the solid which was estimated at ~10%/100 K. Hence, the capacity varies between 120 (no sensible storage) and 190 MWh_{th} (ΔT_{solid}=600 K). The reactor operation is as follows: After the discharging, the bed is at 600°C. Hot air enters the reactor at 1200°C and is cooled to the equilibrium temperature of 900°C while charging the bed. At the completion of charging, the entire bed is heated up to the air inlet temperature of 1200°C. During the discharging process the air enters the storage system at 600°C and is heated up to the equilibrium temperature of 900°C. After the discharging process the solid temperature is again at 600°C. The effect of this process on the parasitic load is shown in Fig. 6.9. The demand of $P_{C,th}/P_{th}<20\%$ can only be met during the first 4 hours of the charging process. When integrated over an 8 hour period, the parasitic work is 18% even though a transient ratio as high as 28% was seen. For discharging, $P_{C,th}/P_{th}$ stays below 20% for the entire 8 hour period. A fixed bed with 3 cm diameter particles shows promising performance in terms of temperature, power level and pressure drop, but particle sizes smaller than 3 cm are not acceptable in this fixed bed design with regard to the pressure drop.

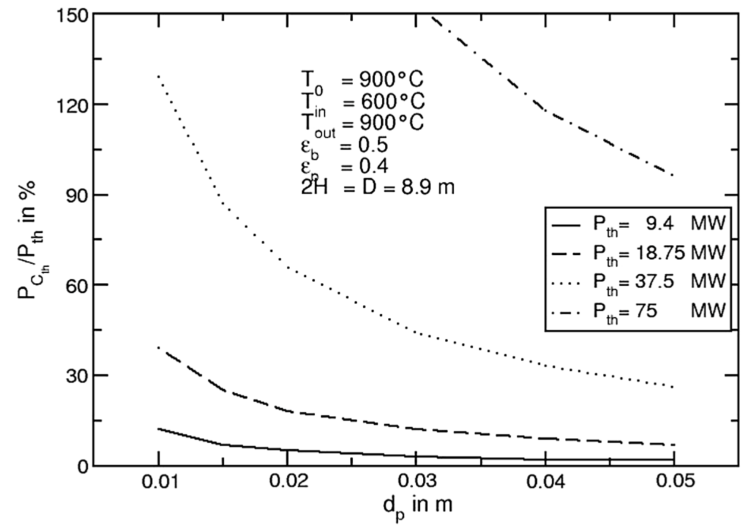

Fig. 6.8 Influence of power level on compression work during discharge.

Table 6.4
Design Parameters for a 1200 MW_{th} TES System

Geometry, Capacity	Bed Properties	Boundary Conditions	Power, Mass Flow
8x (Ø 8.9 m, H=4.45 m) 8x 504 t_{Co3O4} 8x ~120-180 MWh_{th}	ε_b=0.5, ε_p=0.4 d_p=0.03 m	$P_{out,d}$: 0.91 bar $P_{out,r}$: 0.91 bar $T_{in,d}$: 1200°C $T_{in,r}$: 600°C	8x P_d = 18.75 MW_{th} 8x P_r = 18.75 MW_{th} 8x $m_{air,d}$ =56.4 kg/s 8x $m_{air,r}$ =54.6 kg/s

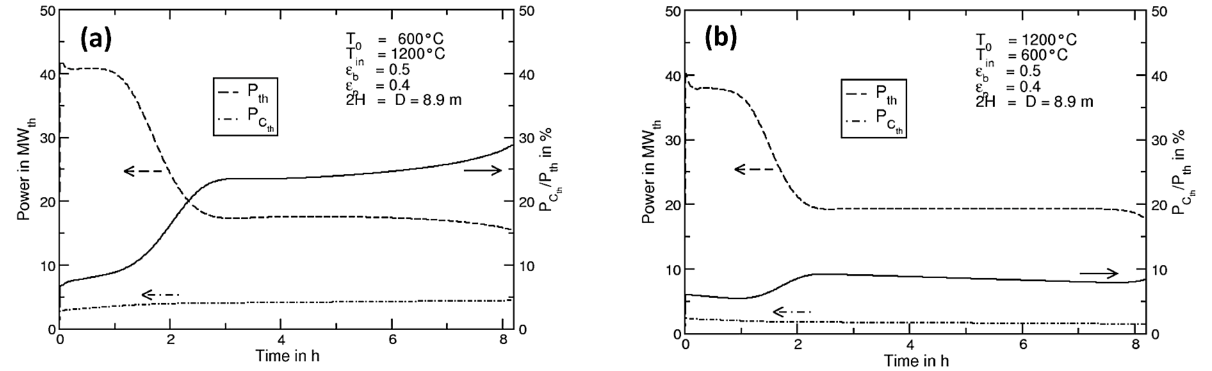

Fig. 6.9. Calculated power and parasitic losses during (a) charging and (b) discharging.

The limitations of the designed system discharge due to reaction and mass flow rates were investigated. Compared to the baseline case, if the reaction rate is effectively reduced by a factor of 100 (η_R=0.01), the discharge can still be accomplished within 8 hours [Fig. 6.10(a)] and provide a constant heat outlet at 900°C. Only at much slower reaction rates (η_R=0.001) does one observe a failure for the reactor to reach the operation targets. Hence, the reaction kinetics of cobalt-aluminum oxides had been improved to the point that it is no longer a limiting factor in the design for power levels up to 18.75 MW_{th}. In case of higher mass flow rates the limitation is stronger, as seen in Fig. 6.10(b). At the slower reaction rate (η_R=0.001) the demanded outlet temperature of 900°C cannot be reached. This serves as a reference for the applicability of TES oxides with slower reaction kinetics.

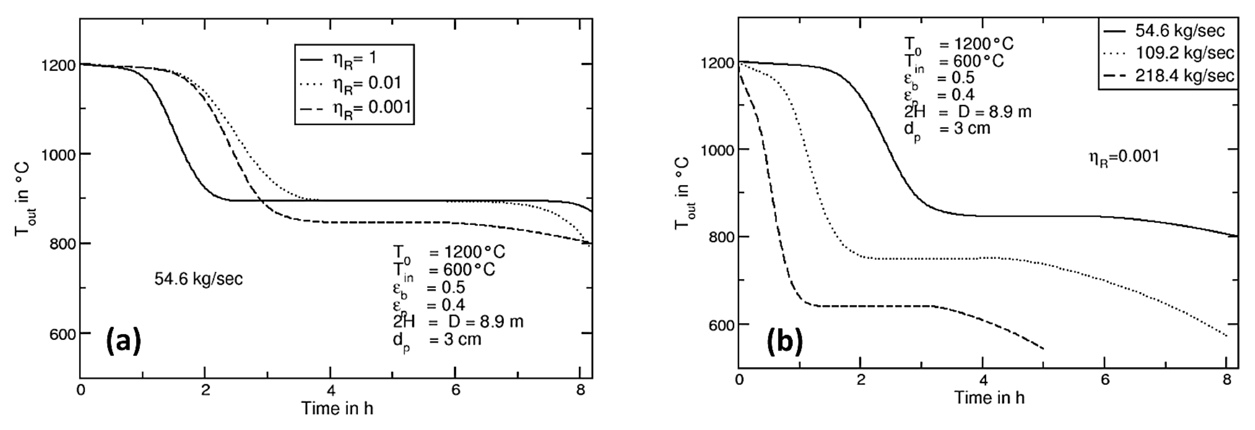

Fig. 6.10. Influence of (a) reaction and (b) mass flow rates on reactor performance during the discharging process.

In conclusion, a thermochemical heat storage system based on the reduction and re-oxidation of cobalt monoxide was investigated theoretically in terms of pressure drop, temperature distribution and power level. The proposed design of Table 6.4 is a fixed bed with direct contact between the solid material and the heat transfer fluid (HTF) air. It consists of 8 cylindrical reactor units of ~120-190 MWh_{th} thermal storage capacity. The nominal power is 18.75 MW_{th} per reactor unit which corresponds to a mass flow rate of ~55 kg/s and a charging/discharging time of 8 hours. The solid temperature shifts between 600°C and 1200°C while the outlet temperature is ~900°C according to equilibrium conditions.

Because of the higher temperature level the pressure drop is more critical for the charging process. If 20% parasitic losses can be accepted and a mass flow rate of ~55 kg/s is set, a minimum particle size of 3 cm and a temperature drop of the HTF between inlet and outlet of at least 300 K is required. On the other hand, in a bed of bigger particles, heat transfer limitation may become an issue. As an increase/decrease of the outlet temperature could be observed for the charging/discharging process for particle diameters larger than 3 cm, a minimum particle diameter of 3 cm is preferred. Assuming that the reaction kinetics are comparable to those of the powder form, a constant outlet temperature can be achieved during the charging and discharging process. A reduction of the reaction rate could be in principle acceptable down to 1% of the kinetics of the powder. The investigation of the heat transfer and kinetic limitation is valid for a power level up to 18.75 MW_{th}. In case of higher mass flow rates, these limitations may become more critical.

7. TES SYSTEM ECONOMICS

For the proposed solid oxide based system to be implemented, the cost produced energy must be competitive. Hence, system economics of a CSP integrated with solid oxide based TES were evaluated using the baseline TES system design discussed in Chapter 6. The overall storage cost and levelized cost of electricity (LCOE) were calculated. For comparison purposes, the preliminary economics of a “closed” TES system based on calcium oxide were also evaluated. Published reaction rates were used for this study.

7.1. OXIDE BASED TES SYSTEM FLOWSHEET EVALUATION AND ECONOMICS

Two coupled components of the investigation into oxide TES are (1) evaluation of process flowsheets and (2) the economics of thermal storage and electricity production. It is desired to make collection of solar energy and its subsequent conversion to electricity as efficiently and economically as possible. Thus, material and energy balances are conducted and process components are designed to meet these goals. Economics and thermal efficiency are closely coupled, as tradeoffs must be found to determine the minimum cost. Highest thermal efficiency seldom equates to minimum cost. A crude example of this is illustrated in heat exchanger temperature differences. As temperature differences are minimized, thermal efficiency increases. To accomplish this, however, heat exchanger area increases as well, and this increases cost. Economic considerations are thus integrated as early as possible into process design. Software tools are used to develop process flowsheets based upon rigorous thermodynamic models. Flowsheet data are then used as input for economic evaluation software tools. Finally, design and cost for TES and power generation is integrated into the design for the solar power components. The levelized cost of electricity (LCOE), typically given in \$/kW$_e$-h, and capital cost of TES, typically given in \$/kW$_t$-h, are the primary economic parameters used to analyze the economic viability of a solar electricity plant design.

7.1.1. The Oxide Cycle Process Flowsheet

The basic components of oxide-based flowsheets are the same for all cases. These components and the general configuration of the flowsheets are shown in Fig. 7.1. As shown in the figure, each flowsheet contains the following equipment:

- Equipment for collection and transfer of solar thermal energy
- TES equipment, in this case consisting of oxide packed-bed reactors
- Equipment for power generation, most commonly done with steam Rankine cycles
- Equipment for recuperating thermal energy within the process

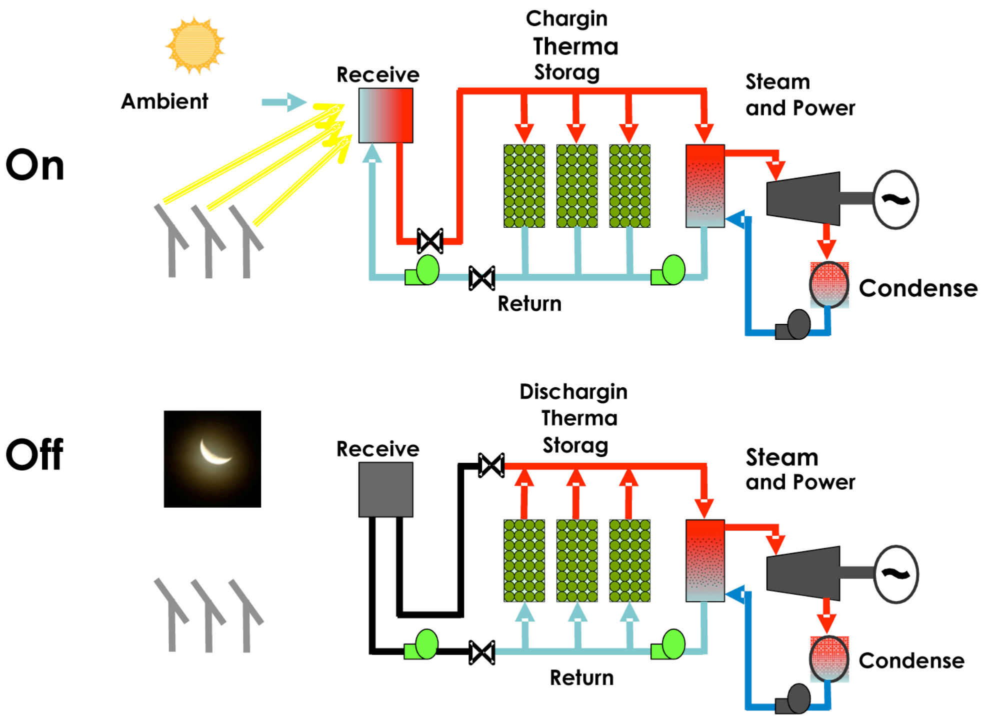

Fig. 7.1. Oxide based TES System Flowsheet Configuration

Oxide-based TES utilizes oxide transitions typically occurring over 500°C, and often near 1000°C. Thus, power tower configurations with heliostat fields are normally considered for solar thermal energy collection. Thermal receivers collect the focused thermal energy and transfer it to the process fluid (air). Packed-bed reactors contain the oxide TES material. Hot air passing through the bed during on-sun hours drives the reduction of the oxide bed, at the cost of lowering the process fluid temperature. Air passing through the oxide beds during off-sun hours is used to oxidize the beds to their original state, and heat is transferred in this case back to the process fluid. Thus, the temperature of the air exiting the packed beds is relatively constant. Steam generators and turbines produce the electricity, and heat exchange recuperators are used to recover heat remaining in the process fluid after power generation.

7.1.2. Methods for Flowsheet Analysis

Four primary tools are used to design and optimize oxide-based flowsheets:

- Aspen Plus® chemical process simulator
- Aspen Process Economic Analyzer
- COMSOL computational fluid dynamics software
- System Advisor Model

Aspen Plus® is a chemical process simulation tool used widely within the chemical process industries. It incorporates multiple thermodynamic models and some of the unit operations it is capable of rigorously simulating include heat exchangers, distillation columns, chemical reactors, and electric power conversion units. Both chemical and phase equilibria can be predicted, and the chemical reactor models can accept the gas-solid phase redox reactions that take place in the oxide TES packed beds. Sensitivity studies can be done to optimize design parameters. An additional feature is that the heat and material balances can easily be done at any scale. Models which produce one unit of product per time are useful in early calculations of process efficiency, and full-scale plant models can be used to evaluate process equipment at the intended output level.

The Aspen Process Economic Analyzer (APEA) allows for sizing and costing of chemical process equipment. It can be operated as a stand-alone package, or more conveniently, as an add-in to Aspen Plus®. Once a flowsheet is optimized at the desired scale, the equipment sizing and costing features of APEA can be activated and run within Aspen Plus®. This facilitates the use of costing as a criterion early in the design process.

COMSOL is a multi-physics software platform that uses finite element techniques for analysis of complex fluid systems, including reacting flows, as is found in the oxide packed-bed reactors. Important parameters, such as temperature profiles and working fluid pressure drops in the reactors, can be estimated with COMSOL.

The System Advisor Model (SAM) is a simulation tool developed at the National Renewable Energy Laboratory. It allows for preliminary design of several renewable energy technologies, including wind, geothermal, and solar plants. SAM contains a power tower module that allows for design of plants collecting concentrated solar thermal power. A key capability, given the proper inputs, is the prediction of costs for LCOE and TES, and also the plant capacity factor.

Capacity factor quantitatively is the ratio of actual power plant output over the course of one year to the power output if the plant were operating at 100% of capacity for the entire year. Qualitatively, the capacity factor is a measure of several parameters affecting solar plant output, including:

- Plant TES capacity
- Solar multiple
- Annual solar insulation at the plant site

As plant TES capacity increases, so does the capacity factor, as the plant is capable of operating longer during off-sun hours. The solar multiple (SM) is the ratio of solar plant peak thermal capacity to the thermal requirement of the power block at the design point. More energy is available for storage as SM increases. Annual solar insulation is a measure of annual solar energy available at a given site, and also of how the available energy varies over the course of the year. More daylight hours and more thermal energy are available during summer months, for example. To illustrate, Fig. 7.2 is a graph or solar insulation as measured in Daggett, California.

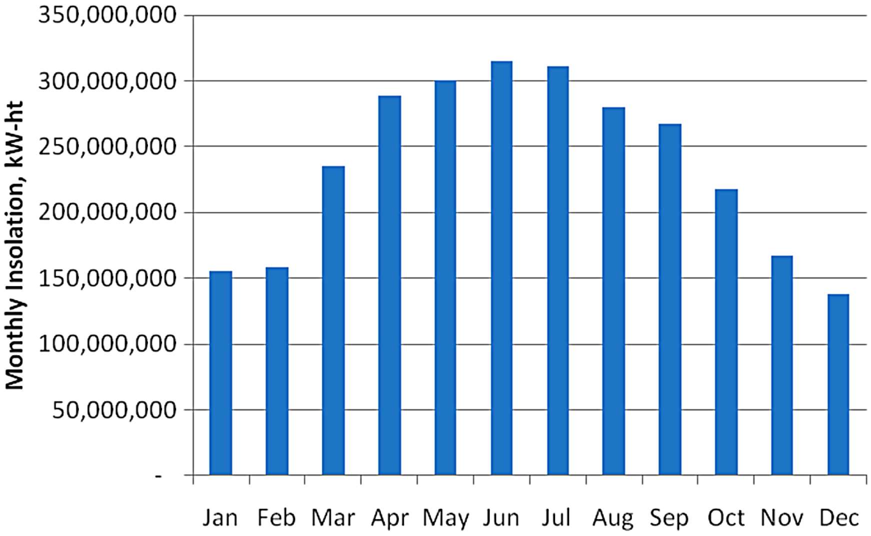

Fig. 7.2. Solar Insulation Variation by Month in Daggett, California (SAM database).

Costs for TES and LCOE were estimated for several oxide cycles over the course of the project, as shown in Figs. 7.3 and 7.4. These cost data, in conjunction with experimental results for actual redox reaction performance, allowed for particular focus on two cycles:

- Mixed Manganese Oxide
- Cobalt Oxide

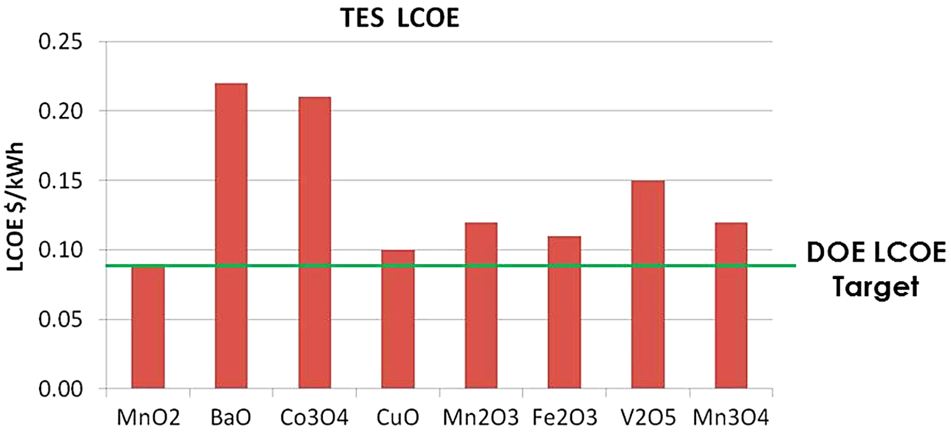

Fig. 7.3. LCOE for oxide-based TES plants.

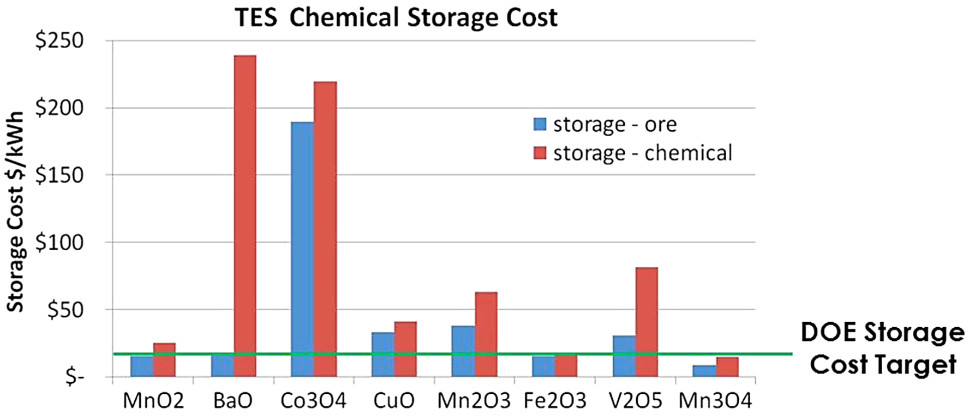

Fig. 7.4. TES costs for oxide-based TES plants.

The manganese oxide cycle stood out as having the lowest predicted LCOE. However, experimental REDOX performance was only satisfactory when a mixed manganese oxide was used. A detailed cost estimate of manufacturing/preparation of mixed oxides for use at plant scale was not completed before the end of Phase II, but a preliminary study was done for future reference to look at the effect of mixed oxide processing on LCOE. It was found that a maximum cost of \$0.50/kg oxide could be incurred for processing (beyond raw ore cost) and keep the LCOE at or below \$0.09/kW-h_e.

The cobalt oxide cycle is of technical interest, as it was a consistently good performer in the laboratory experimental evaluation of REDOX reactions in metal oxides. The cost of the ore is high, however, which makes it a difficult choice on an economic basis. However, the cobalt cycle is useful for illustrating details of the flowsheeting and costing process, as shown in the following section, using the tools described previously.

7.1.3. Costing Example using Cobalt Oxide

Figure 7.5 is an Aspen Plus® graphic describing the major components of the Oxide TES cycles. In it, “CAV1”, “DSTEAM”, and “DPOWER” simulate the solar heat input, the steam generator, and the power turbine components that are already adequately modeled within SAM.

“DBED1” and “DRECUP1” are the components that are not included in the SAM standard template. DBED1 represents the oxide packed-bed reactors, and DRECUP1 is a heat exchanger that recovers energy from the air exiting the steam generator. Aspen Plus® calculates composition, and heat and energy balances for each stream and component. It then links with APEA to size each component at the desired level, and assigns capital and installation costs.

For a 50 MWe cobalt oxide plant, APEA determined that a total of 18 shell-and-tube heat exchangers are required to carry out the heat recovery represented by RECUP1, at a total cost of \$10.4 million.

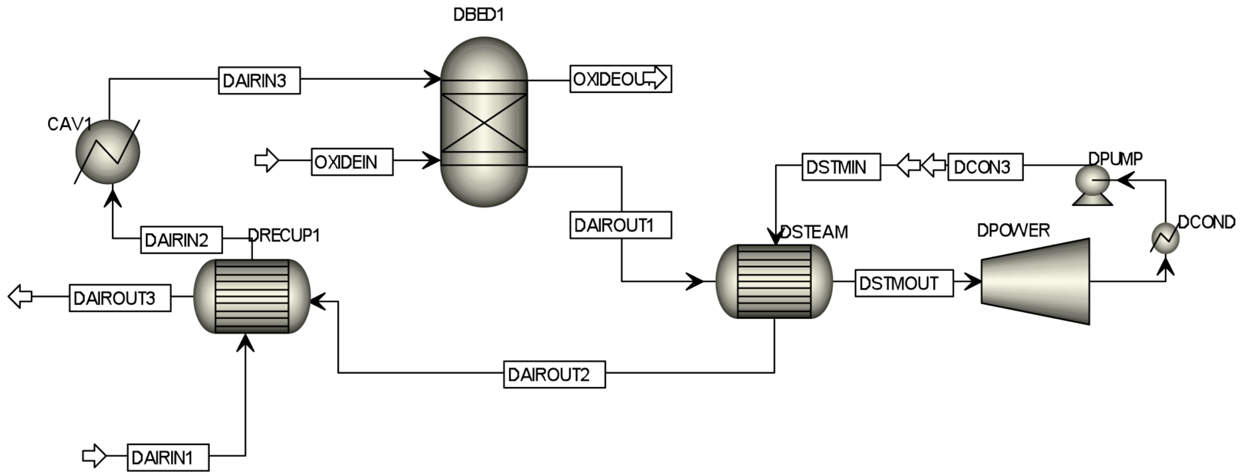

Fig. 7.5. Major components of the Oxide TES Cycle Flowsheet, as represented in Aspen Plus®.

The packed-bed reactors were sized by DLR using COMSOL. A total of 8 reactors of height 4.45 m and diameter 8.9 m provide the necessary thermal energy (1200 MW-h_t) to the process fluid. This reactor configuration minimized parasitic energy losses due to overcoming reactor pressure drop. The reactor dimensions were then supplied to APEA. In this case, carbon steel reactors were specified, with 12 inches of internal insulation. In addition, an Inconel cladding was included to preclude any corrosion of the carbon steel. APEA calculated a total cost of $11.4 million for the reactors, including $423,000 for the installed mineral wool insulation.

DLR assumed a bed porosity of 0.5, and a particle porosity of 0.4, resulting in an overall porosity of 0.7. This porosity over the volume of 8 reactors, with an oxide density of 6000 kg/m^3, leads to a requirement for 4 million kg of oxide. Table 7.1 below summarizes TES costs for 1200 MW-h_t capacity as a function of assumed cobalt oxide cost.

Table 7.1
Cobalt Oxide TES Cost Summary

Oxide cost per kg	$43	$20	$10
Total oxide cost	$172 Million	$80 Million	$40 Million
Oxide + Reactor costs	$183.4 Million	$91.4 Million	$51.4 Million
TES cost per kW-h_t	$153	$76	$43

These TES costs per kW-h_t were then inserted into SAM, along with the cost of the heat recuperation equipment and reactors from APEA, and LCOE calculations were done from there with standard SAM tools and techniques.

The DLR analysis showed that reactor pressure drop is the primary factor in efficient design. COMSOL results confirmed that parasitic losses for air delivered at temperatures near the cobalt oxide transition temperature are unacceptably high, thus DLR increased the temperature until these losses were reduced to a relatively low fraction of plant output. It was found that air at 1200°C allowed the reactors to operate in this way.

However, the combined impact on LCOE of higher peak temperature and remaining system pressure losses is severe. The cost of the solar equipment, primarily due to increased heliostat area, increases considerably. For example, at 9 hours of TES capacity, the LCOE for packed-bed reactor conditions described by DLR is near $0.30/kW-h, as summarized in Fig. 7.6.

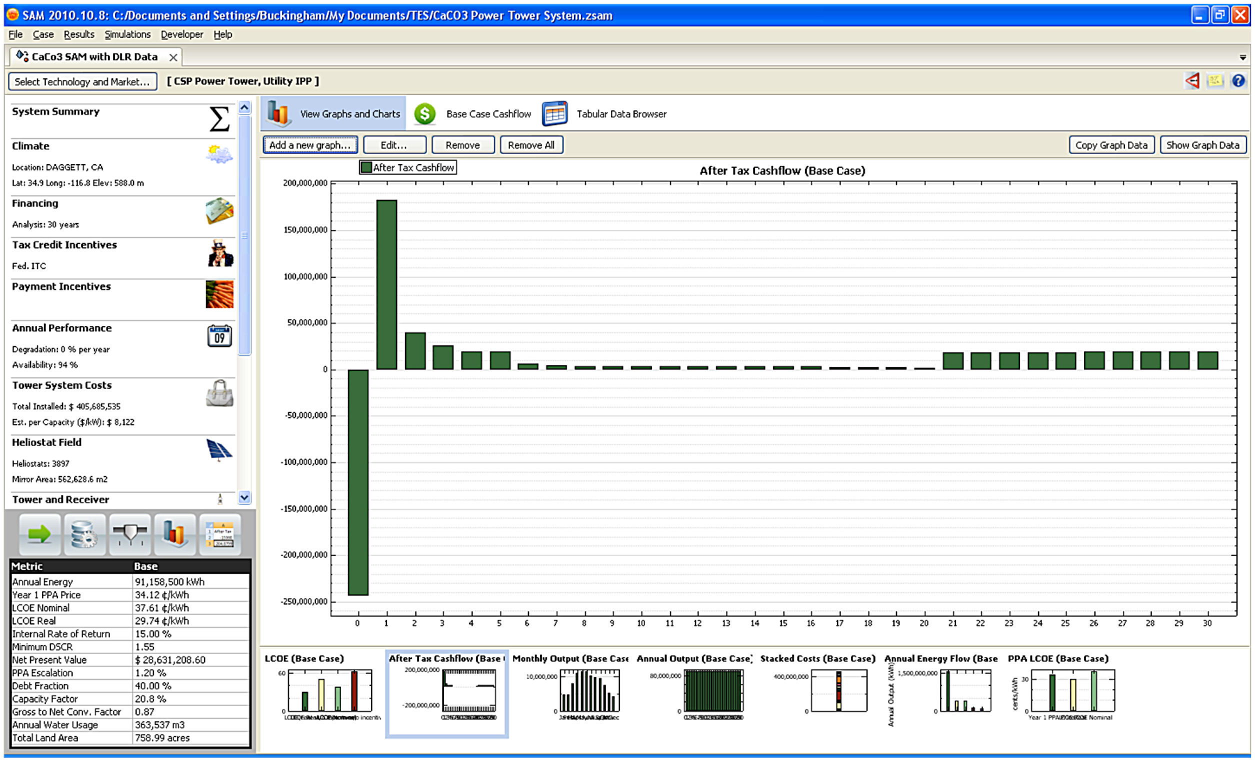

System Summary

Climate
Location: DAGGETT, CA
Lat: 34.9 Long: -116.8 Elev: 588.0 m

Financing
Analysis: 30 years

Tax Credit Incentives
Fed. ITC

Payment Incentives

Annual Performance
Degradation: 0 % per year
Availability: 94 %

Tower System Costs
Total Installed: $ 405,685,535
Est. per Capacity ($/kW): $ 8,122

Heliostat Field
Heliostats: 3897
Mirror Area: 562,628.6 m2

Tower and Receiver

Metric	Base
Annual Energy	91,158,500 kWh
Year 1 PPA Price	34.12 ¢/kWh
LCOE Nominal	37.61 ¢/kWh
LCOE Real	29.74 ¢/kWh
Internal Rate of Return	15.00 %
Minimum DSCR	1.55
Net Present Value	$ 28,631,208.60
PPA Escalation	1.20 %
Debt Fraction	40.00 %
Capacity Factor	20.8 %
Gross to Net Conv. Factor	0.87
Annual Water Usage	363,537 m3
Total Land Area	758.99 acres

Fig. 7.6. SAM output for DLR packed-bed design.

These results, found at the end of Phase II, suggest that a realistic packed-bed reactor design for Oxide TES is not economically competitive. The advanced CFD analysis techniques utilized with COMSOL were crucial in this finding. This configuration is bound by parasitic losses at lower temperatures and high solar field costs at higher temperatures. See the following section for recommended actions in the event that investigations into oxide TES are renewed in the future.

7.1.4. Recommendations for Future Economic Improvements

Two avenues for cost reduction could be pursued to reduce LCOE for oxide-based cycles. The first is a change in reactor configuration to a "moving bed" design. This could be a rotary kiln, as is being explored at DLR, or a fluidized bed reactor. A rotary kiln, for example, would not be subject to the pressure drops seen in a packed bed reactor. Advantages stemming from "exergetic efficiency" would also allow for lower peak temperature in the solar collection equipment. Exergetic efficiency can be a measure of how effectively heat is used. It specifically compares the temperature at which heat is utilized to the temperature at which it is collected. An equation illustrating this is:

$$\text{Exergetic efficiency} = \frac{1 - \dfrac{298\,\text{K}}{T_{discharge}}}{1 - \dfrac{298\,\text{K}}{T_{charge}}} \quad .$$

The heat is supplied to the packed bed reactor is at 1200°C (1473 K) and the equilibrium discharge temperature sent to the power generation equipment is near 927°C (1200 K). In this case the exergetic efficiency is 94.2%. A rotary kiln could operate at a charging temperature 50°C high than the discharge temperature, or 1250 K. Thus, the exergetic efficiency of a rotary kiln design would be 98.6%. Ultimately, the reduced pressure drop and lower peak temperature in the rotary kiln design would have significant cost improvement effects.

Lastly, a new design for power generation equipment could be considered. A power cycle based on a working fluid other than steam could provide for increased efficiency. The use of supercritical CO_2, for example, in a cycle operating near the oxide transition temperature would minimize heat exchanger temperature differences. Such cycles can be as many as 10 percentage points higher in efficiency compared to steam Rankine cycles. If the cost of equipment were competitive, the increased power conversion efficiency would have a measurable beneficial impact on LCOE.

7.2. CLOSED CYCLE ECONOMICS ASSESSMENT

Preliminary economics of a closed cycle based on calcium carbonate were assessed to determine whether it has any advantage over an open cycle system. In the calcium carbonate ($CaCO_3$) cycle, charging and discharging is based on the release and absorption of CO_2:

$$CaCO_3(s) \leftrightarrow CaO(s) + CO_2(g) \quad .$$

The primary complication is CO_2 separation and capture as it is not viable to vent large volumes of CO_2 on a continuous basis, so the cycle must be "closed." Separation of CO_2 from the heat transfer fluid (e.g. air) is essential as $CaCO_3$ dissociation requires a very low CO_2 inlet concentration due to the low dissociation pressure of CO_2. In contrast, a high CO_2 partial pressure is preferred for $CaCO_3$ formation. These two factors lead to the requirement for separation of low concentration CO_2 (3%-7%) from large volumes of air as the cycle progresses. In this case study, a monoethanolamine (MEA) solvent CO_2 extraction plant was coupled to a TES flowsheet comprised of packed bed reactors and heat exchange equipment. The estimated LCOE cost of such a plant is \$0.31/kW-h. Even though calcium carbonate is extremely cheap, the requirement to extract, compress and store CO_2 in a carbonate based TES system made it significantly more expensive than the oxide based open loop system.

8. SUMMARY

This project investigated the engineering and economic feasibility of using thermochemical cycle based multivalent solid oxides for Thermal Energy Storage (TES). The concept is based on a pair of reduction and oxidation (REDOX) reactions which forms a thermochemical cycle (TC). A list of 16 pure oxides TCs was identified as TES candidates using HSC Chemistry software. The list was narrowed down to 10 based on potential cycle operating temperatures and storage costs. Preliminary laboratory measurements and literature data showed only BaO_2, Co_3O_4, Mn_2O_3, CuO, Fe_2O_3, and Mn_3O_4 have demonstrated reversibility in their REDOX behavior under ambient conditions. A final down select was carried out and this list was further reduced to the first three oxides as the latter three were judged to be impractical for this application. Additional laboratory measurements revealed that re-oxidation kinetics improvements were needed for BaO_2, Co_3O_4, and Mn_2O_3 for them to be used as TES media.

A novel approach to enhance the REDOX kinetics of the three selected oxides was established. This technique incorporates selected secondary oxides into the matrix of the primary oxide via mechanically alloying and annealing. The partial replacement of the primary cation by an appropriate secondary cation gave rise to a charge imbalance in the lattice and increased the density of vacancies. These vacancies enhanced the ionic mass transport and resulted in faster re-oxidation kinetics. For example, the re-oxidation fraction of $Mn_3O_4 \rightarrow Mn_2O_3$ was improved by 16 times through the addition of iron oxide. Similar enhancements have been observed in cobalt-iron and cobalt aluminum mixed oxides. On the other hand, no improvement was realized in any of the barium mixed oxides. Both manganese and cobalt mixed oxides were shown to exhibit stable REDOX kinetics even after long term thermal cycling. Their TES capacity after cycling was significantly higher than their pure oxide counterpart. This can be attributed partly to the reduced grain size that stemmed from secondary oxide addition. Based on the measurement results, manganese-iron, cobalt-aluminum and cobalt-iron mixed oxides have been proposed for bench top demonstration.

The baseline system concept utilizes a packed bed reactor for charging and discharging of the TES oxide. Additionally, a moving bed reactor can also be used. The applicability of both approaches was demonstrated repeatedly in the laboratory using cobalt and manganese based oxides. To prepare for the construction of prototype reactors, construction materials compatible with manganese-iron and cobalt-iron mixed oxides were identified. Inconel 625 was found to have the best compatibility with both oxides.

To design the TES system, a reactor model was established. Measured cobalt-aluminum oxide reaction kinetics were applied to the model and the influences of bed properties and process parameters on the overall system design were investigated. The optimal design was found to be a network of eight fixed bed reactors at 18.75 MW_{th} each with charge and discharge temperature between 1200°C and 600°C which provides a constant output temperature of 900°C.

The charge and discharge time are 8 hours each respectively. Modeling results also showed that the cobalt-aluminum oxide reaction kinetics are fast and do not pose any limitation to the design. On the other hand, the mass flow rate design point must be carefully defined to minimize parasitic loads and oxide particles at around 3 cm in size work best for the present design.

A process flowsheet of a CSP plant integrated with an oxide based TES system was established. The system design defined by the reactor modeling work, the cobalt mixed oxide and the appropriate construction materials were incorporated into the flowsheet. The NREL (Solar Advisory Model) was used to define the cost of the solar facilities. It was found that the storage cost based on cobalt oxide is around $40 but can potentially decrease to $10 based on reduced materials cost on a bulk scale. The corresponding calculated LCOE was between $0.22-0.30/kW-h which also exceeded the DOE target. This cost is due to the high charging temperature required in this first design and the cost of cobalt oxide. It is expected that a moving bed reactor with manganese oxide will significantly decrease the associated cost.

In conclusion, the project demonstrated the engineering feasibility of using multivalent solid oxides for TES applications. A system based on manganese oxide and a rotary kiln has the potential to meet the economics targets. The following table summarizes the planned goals and accomplishments in the project.

GOALS	ACCOMPLISHMENTS
Identify a list of potential TC for TES and carry out preliminary evaluation	A list of 16 oxides applicable to the proposed TES concept were found
Establish an experimental protocol to evaluate the TC candidates	A protocol to measure the short and long term REDOX behavior of TES oxide has been established
Carry out a down select to narrow down the list of TC candidates for further development	Manganese, cobalt and barium oxides were selected for further development
Improve the short and long REDOX kinetics of TC candidates	The reaction kinetics of manganese and cobalt based oxides were dramatically improved through the incorporation of mixed oxides
Establish a reactor model based on the REDOX kinetics of the developed oxide	A packed bed model was established. It was used to design a TES system. The sensitivity of reactor performance to various process parameters and bed properties was established
Identify materials that can be used for reactor construction	Inconel 625 was selected as the best construction materials after extensive thermal cyclic testing
Design a CSP plant flowsheet integrated with solid oxide based TES and calculate the preliminary economics	A flowsheet that incorporate a CSP plant with a solid oxide based TES system has been established. The TES storage cost and LCOE using cobalt oxide have been defined
Carry out on sun demonstration in a rotary kiln reactor	Charge and discharge of cobalt oxide has been demonstrated in a directly irradiated rotary kiln reactor

8.1. PROJECT IMPACT

This project made a technical impact in several areas. First, an approach to improve solid oxide REDOX kinetics has been established. This innovation is useful not only for TES but also in the area of high temperature chemical heat pumps, synfuel production, water-splitting and oxygen generators. In addition, it was the first time that a solid oxide based TES concept has been demonstrated in a rotary kiln. The project also demonstrated that such a plant is feasible (from an engineering perspective) and that the compatible engineering construction materials are available. Based on the accomplishments of this project, the European commission has established a sponsorship of a similar project in developing oxide based monolithic materials for thermal heat storage applications.

ACKNOWLEDGMENT

This work prepared for the U.S. Department of Energy under DE-FG36-08GO18145.

APPENDIX A
PROGRESS REPORT FROM GERMAN AEROSPACE CENTER

Deutsches Zentrum
für Luft- und Raumfahrt e.V.
in der Helmholtz-Gemeinschaft

Progress Report

Date of preparation: 03/11/2011

Thermochemical Heat Storage for Concentrated Solar Power

Thermochemical System Reactor Design for Thermal Energy Storage

Phase II
Task 7.2 Reactor Design

Award number: DE-FG-08GO18145

Period covered: from 07/15/2010 to 01/15/2011

F. Schaube, A. Wörner, R. Tamme
German Aerospace Center
Institute of Technical Thermodynamics
Pfaffenwaldring 38-40
D-70569 Stuttgart

1 Preliminary results of phase 1

In phase I, a preliminary study of a possible reactor design with its limitations and specific requirements for a thermochemical heat storage system was presented. The results were based on the endothermic dissociation of cobalt monoxide and its exothermic re-oxidation:

$$Co_3O_4 + \Delta H \leftrightarrow 3\ CoO + 0.5\ O_2\ . \quad (1)$$

A system of 1D partial differential equations and initial and boundary conditions was applied. It was solved numerically by the Finite Element Method (FEM) using the software COMSOL Multiphysics® giving a spatial evolution of temperature, pressure and solid density over time.
In the fixed bed reactor the pressured drop and the consequent losses were a main concern. Therefore modifications of the predetermined reactor design were necessary to meet the system requirements. For the new design the temperature distribution was calculated for the discharging process (re-oxidation) and showed promising performance with regard to the outlet temperature of the reactor. However, the results were strongly depending on the input parameters such as reaction kinetics.
As in phase II improved data on the reaction kinetics are available, the reactor design as well as the charging and discharging processes are studied in detail taking into account the new experimental data. Table 1 shows the desired specifications for such storage system.

Table 1: Specifications

Capacity	Bed properties	Boundary conditions	Power
1200 MWh_{th}	*Fixed bed* *$\varepsilon > 0.5$* *$d_p < 0.1$ m*	*$P_{in,d}$: 0.95-0.9 bar* *$P_{in,r}$: 1 bar* *$T_{in,d}$: 1000°C-950°C* *$T_{in,r}$: 600°C*	*$P_d = 150\ MW_{th}$* *$P_r = 75\text{-}600\ MW_{th}$* *$P_{cth}/P_{th} < 20\%$*

2 Properties

The solid properties such as density, porosity, heat capacity, thermal conductivity and heat of reaction are summarized in Tab. 2. In this study the bed porosity ε_b defines the void fraction of the bed whereas the particle porosity ε_p defines the void fraction within the particle. In case of $\varepsilon_p<1$ the overall porosity ε is lower than the bed porosity ε_b (Eqn.(2)).

Table 2: Solid properties

Density at end of discharge, ρ_{ss}	6070 kg/m^3
Density at end of charge, ρ_{s0}	5667 kg/m^3
Porosity, ε_b	0.5
Porosity, ε_p	0.4
Specific heat, c_{pR}	628+0.12*T_s J/kgK
Specific heat, c_{pO}	328.6+0.55*T_s J/kgK
Particle thermal conductivity, λ_s	1 W/mK
Reaction heat of formation, ΔH	844 kJ/kg$_{Co3O4}$

$$\varepsilon = \varepsilon_b + \varepsilon_p - \varepsilon_b\varepsilon_p \quad (2)$$

The reaction rate is defined by an effectiveness factor η_R, the dimensionless conversion rate $\partial X / \partial t$, the porosity ε and the maximum and minimum density. For a first analysis, η_R=1 is used.

$$\mathrm{R} = \eta_R \left(\partial X \big/ \partial t \right)_{d/r} (1-\varepsilon)(\rho_{ss} - \rho_{s0}) \quad (3)$$

The conversion rates for the dissociation and re-oxidation as well as the equilibrium line of cobalt monoxide with additional 5% of Al_2O_3 have been determined by General Atomics in thermogravimetric measurements:

$$\left(\partial X \big/ \partial t\right)_d = -1.01\cdot 10^{28}\exp(-731000/RT_s)(1-X)(-\ln(1-X))^{2/3} \qquad (4)$$

$$\left(\partial X \big/ \partial t\right)_r = 1.06\cdot 10^{7}\exp(-183801/RT_s)(1-X)(-\ln(1-X))^{2/3}\,(\mathrm{P}/\mathrm{P}_{eq}\text{-}1) \qquad (5)$$

$$\mathrm{Ln}(P_{eq}) = -25.422 * 1000/(T_{eq}) + 20.01 \qquad (6)$$

It is assumed that all the solid material takes actively part in the process.

3 Mathematical model

The equation system of the mathematical model has been described in detail in the progress report of phase I. In the following, the equation system is given including an additional mass balance for the oxygen in Eqn.(9). In addition, the pressure work is taken into account in the gas energy balance Eqn.(11).

$$\frac{\partial}{\partial t}(1-\varepsilon)\rho_s = R \qquad (7)$$

$$\frac{\partial}{\partial t}(\varepsilon\,\rho_g) + \nabla\cdot(\rho_g u) = -R \qquad (8)$$

$$\varepsilon\,\rho_g \frac{\partial}{\partial t}(w_{O2}) + \rho_g u\cdot\nabla(w_{O2}) = -(1-w_{O2})R \qquad (9)$$

$$\nabla P = -\frac{\mu_g}{K}u - c_F\sqrt{K}^{-1}\rho_g u^2 \qquad (10)$$

$$\varepsilon\rho_g\, c_{pg}\frac{\partial T_g}{\partial t} + \rho_g c_{pg}(\nabla T_g)\vec{u} = \varepsilon\nabla\cdot(\lambda_g\cdot\nabla T_g) + Rc_{pg}T_g + h_{sg}(T_s - T_g) \qquad (11)$$

$$(1-\varepsilon)\rho_s\, c_{ps}\frac{\partial T_s}{\partial t} = R(\Delta H - c_{ps}T_s) + h_{sg}(T_g - T_s) \qquad (12)$$

The volumetric heat transfer coefficient h_{sg} is calculated in Eqn.(15) depending on the heat transfer coefficient h defined by Gnielinski [1], particle surface area, particle diameter and thermal conductivity of the particles.

$$h_{sg} = \frac{6(1-\varepsilon_b)}{d_p}\left(\frac{d_p}{10\lambda_s} + \frac{1}{h}\right)^{-1} \qquad (15)$$

Initial conditions are set to:

$$\rho_s = \rho_{s0},\ P = P_0,\ w_{O2} = w_{O2,0}, T_g = T_s = T_0 \qquad (16)$$

whereas boundary conditions are set to:

$$\vec{n} \cdot \nabla(\rho_s) = 0, \; P_{in} \text{ acc. to } m_{in}, \; w_{O2} = w_{O2,in}, \; T_{g,in} = T_0, \; \vec{n} \cdot \nabla(T_s) = 0 \qquad (17)$$

$$P = P_{out}, \;\; \vec{n} \cdot \nabla(\rho_s) = \vec{n} \cdot \nabla(w_{O2}) = \vec{n} \cdot \nabla(T_i) = 0 \qquad (18)$$

The system of 1D partial differential equations together with the initial and boundary conditions is solved numerically by FEM using the software COMSOL Multiphysics®. Time steps and grid are refined until the results do not depend on the number of calculation points anymore.

3.1 Assumptions

- The thermochemical storage is part of an open, not pressurized system.
- Air is used as the heat transfer fluid (HTF) and is also the medium to transport the reactant oxygen. There is direct contact between the air and the solid material.
- The storage system consists of cylindrical packed bed reactors containing metal oxide spheres.
- The metal oxide forms stable spherical structures with constant porosity and particle diameters up to 10 cm. There is no breakage of particles due to volume expansion. Bed porosity does not change during the process.

4 Reactor design

4.1 Pressure drop

In a fixed bed configuration the pressure drop is a main concern. Therefore the mean pressure drop and its consequent parasitic losses due to pumping power have been evaluated. The properties of air are needed for the calculation of the pressure drop according to Eqn.(10). In this preliminary study, air properties at 1 bar and at a mean temperature, being 1000°C for the discharging and 750°C for the charging process are used [2]. The outlet pressure is set to 0.91 bar which correlates to an equilibrium temperature of 900°C. The thermal equivalent of the isentropic compression work is calculated in Eqn.(19) as a function of pressure drop:

$$P_{C,th} = \frac{1}{0.33} \frac{\kappa}{\kappa - 1} \frac{R}{M_g} T_{in} \dot{m}_{in} \left(\left(\frac{P_{in}}{P_{out}} \right)^{\kappa-1/\kappa} - 1 \right) \qquad (19)$$

4.1.1 Charging process

For the charging process Fig.1 shows the ratio of the thermal equivalent of the compression work to the maximum thermal power versus the number of tanks. It is assumed that the HTF is cooled down to the equilibrium temperature of T_{eq}=900°C while passing through the reactor. A maximum tank diameter of D=2H and a thermal capacity of 1200 MWh_{th} (including sensible storage according to ΔT_{solid}=300 K) is assumed. According to that, the requirement of 8 h charging time leads to the isentropic compression work depending on particle diameter as shown on the left side and inlet temperature as shown on the right.

It can clearly be seen that the pressure work reduces with increasing number of tanks. On the other hand the slope of the lines decreases as well. Therefore a further increase of the number of tanks only slightly reduces the pressure drop.

In addition, bigger particles and lower requested mass flow rates through the reactor (as a result of a higher inlet temperature) lead also to lower pressure drops. Assuming a maximum acceptable ratio of 20%, the required amount of tanks in case of an inlet temperature of 1200°C and 5 cm particles would be 3, in case of 2 cm particles it would be 8 and in case of 1 cm particles 20 tanks are required. For a particle diameter of 5 cm and a reduced inlet temperature of 1100°C 11 tanks are required. However, it has to be noted that the thermal capacity of the tanks includes around 10% per 100 K temperature drop/rise of the solid. Therefore lower inlet temperatures result in capacities <1200 MWh_{th}.

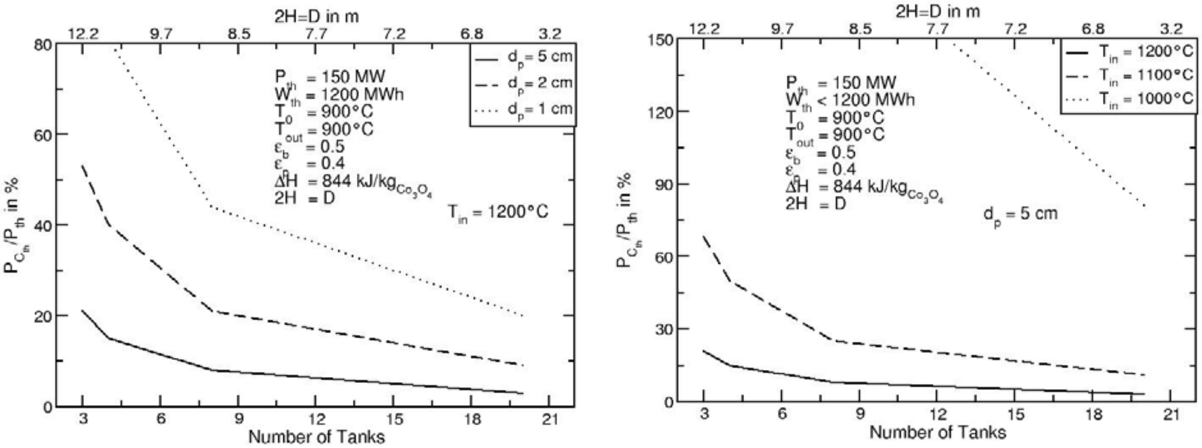

Figure 1: Compression work during charge: $Co_3O_4+\Delta H \rightarrow 3\ CoO+0.5\ O_2$
Influence of particle diameter (left) and inlet temperature (right)

Because of the quadratic term in Eqn.(10) an inlet temperature of 1000°C which may be maximum in solar tower systems results in such high pressure drops that the fixed bed design can not be implemented with theoretical parasitic losses lower than 20%. In that case, a pressurized system, other bed design options such as fluidized beds or rotary kilns or other possible reactions with lower equilibrium temperatures have to be considered. If a fixed bed is realized, a temperature difference of ~300 K between inlet and outlet of the HTF is preferable.

However, in order to exemplify the thermal performance of such storage system, an inlet temperature of 1200°C during charge is used in the following. According to that, a design of 8 tanks with a height of 4.45 m and diameter of 8.9 m containing metal oxide spheres of 3 cm particles is proposed for such storage system. The calculated losses due to the pressure drop are ~13% if 1200 MWh_{th} are transferred within 8 hours.

4.1.2 Discharging process

During the discharging process a temperature difference of 300 K between inlet temperature and equilibrium temperature is theoretically feasible if the inlet temperature is set to 600°C. The system can be designed as proposed above if the requirements in terms of power are equal to those of the charging process. If not, the storage system should be separately dimensioned for either charging or discharging, depending on which case is more critical in terms of pressure drop. Tab. 3 shows different possible discharge configurations with regard to discharge time and power.

If a discharge time of 16 h at a power level of 150 MW_{th} is demanded, the number of tanks has to be doubled in comparison to the charging process. Also, if 16 h can be performed at 75 MW_{th} the mass flow through the 8 tanks and the power transferred per tank decreases. As a result, the pressure drop reduces compared to the charging process.

On the other hand, if a discharge time of 4 or 2 h at a power level of 150 MW_{th} is demanded, higher power levels per tank are required if only 4 or 2 of the 8 tanks should be discharged (These cases are equal to a 8 tank design at 300 MW_{th} or 600 MW_{th}). Another possibility is to partially discharge the 8 (or 16) tanks only to an extent of 50%, 25% or 12.5%. The advantages are lower mass flows or power levels per tank, but additional sensible thermal losses due to temperature equalization within the tank between the charging and discharging process are involved.

Table 3: Tank capacity of 150 MWh$_{th}$, discharge configurations

Discharge time *h*	Power *MW$_{th}$*	Number of tanks *100% conversion*	Number of tanks *x% conversion*	Power per tank *MW$_{th}$*
16	75	*8*	-	*9.4*
16	150	*16*	-	*9.4*
8	150	*8*	-	*18.75*
8	150	-	*16*	*9.4*
4	150	*4*	-	*37.5*
4	150	-	*8*	*18.75*
4	300	*8*	-	*37.5*
4	300	-	*16*	*18.75*
2	150	*2*	-	*75*
2	150	-	*8*	*18.75*
2	150	-	*16*	*9.4*
2	600	*8*	-	*75*
2	600	-	*16*	*37.5*

There are two options to adjust the power level in a direct contact thermochemical storage system. First the mass flow rate can be set according to Fig.2. Higher power levels result in higher mass flows and parasitic losses due to pressure drop. For a required power level of 37.5 MW$_{th}$ or 75 MW$_{th}$ the parasitic losses exceed the requested 20%. Thus, more tanks are required: Assuming particle diameters of 3 cm, 20 tanks of a height of 3.25 m and a diameter of 6.5 m or 70 tanks of a height of 2.15 m and diameter of 4.3 m are required, respectively.

Second the inlet temperature can be reduced. In either case it has to be evaluated whether the reaction kinetics is still fast enough to provide the heat of reaction to rise the temperature of the HTF. Higher power levels per tank may be a difficult task as increasing particle diameters will reduce the reaction rate. These questions are addressed in the following based on the thermal performance of a fixed bed of a height of 4.45 m and a diameter of 8.9 m.

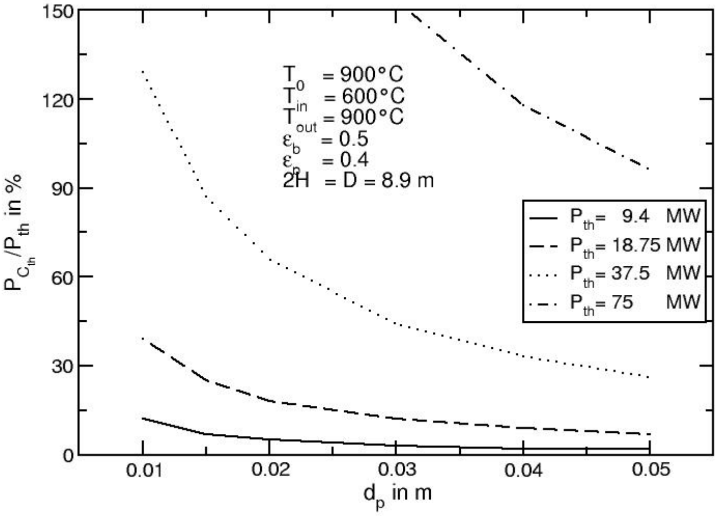

Figure 2: Compression work during discharge: 3 CoO+0.5 $O_2 \rightarrow Co_3O_4 + \Delta H$
Influence of power level

4.2 Thermal performance

During the charging or discharging process of the thermochemical reactor heat has to be provided or removed at a constant temperature level. This can be achieved by setting the mass flow of the HTF and of the reactant in compliance with the heat transfer and reaction rate.

In a fixed bed configuration a reaction and heat transfer zone develops as exemplified for the discharging process in Fig.3. First the incoming air flows through that part of the solid which has already re-oxidised and has therefore already reached the inlet temperature T_{in}. Second the air flow enters the reaction zone where the reaction takes place and heat is transferred from the solid to the gas. As soon as the equilibrium temperature is reached the reaction stops and the air flows through the bed at maximum (=equilibrium) temperature. The length of that zone depends on the reaction kinetics and the heat transfer characteristics. It should be as short as possible compared to the overall length of the reactor because the outlet temperature will start to drop once it reaches the outlet.

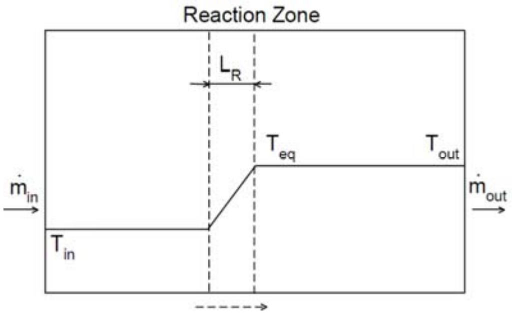

Figure 3: Moving reaction zone

The aim of the following investigation is to classify the limiting parameters with regard to thermal performance. These could be the heat capacity of the overall mass flow rate (A), the feed of the gaseous reactant (B), the solid-gas heat transfer (C) or the particle reaction rate (D). Figure 4 shows the outlet temperature as a function of time for a strong limitation due to case A, B, C or D. In general, the operating point of the reactor should be in a range where the overall mass flow rate is limiting due to the thermal capacity of the feed flow (case A). In that case the heat transfer as well as the reaction rate is fast enough to heat the HTF to the equilibrium temperature. Then the output power level can be controlled by variation of the HTF mass flow rate whereas the outlet temperature is constant throughout the process.

If the heat transfer is limiting (case C) the outlet temperature will start to drop as soon as the reaction zone reaches the outlet as it is not long enough to transfer the required heat to the HTF. In contrast, in case of strong kinetic limitation or a low feed of the gaseous reactant (B, D), the outlet temperature is at a constant level below the desired outlet temperature. The heat transfer is fast enough but the reaction proceeds at a low, constant level throughout the reactor.

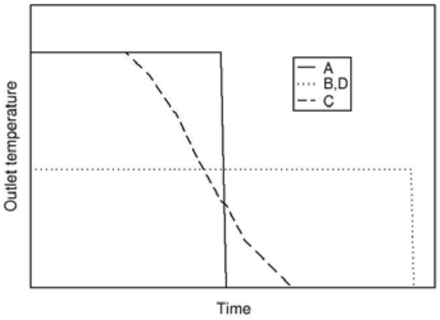

Figure 4: Theoretical outlet temperature

4.2.1 Results

Table 4 summarizes the specifications of a first design in terms of bed geometry and properties, boundary conditions and requested power level. Even though in the case of the charging process the inlet pressure is expected to be 0.95-0.9 bar (outlet of solar plant) and in the case of the discharging process it is expected to be 1 bar (ambient), an outlet pressure of 0.91 bars is assumed. This is due to the fact that only the outlet pressure can be set in the simulation tool if an incoming mass flow is fixed. As this pressure corresponds to an equilibrium temperature of 900°C whereas 1 bar would result in T_{eq}=905°C, the impact on the thermal performance is supposed to be negligible at this point. The inlet pressure is expected to be less than 0.96 bar taking into account the effect of pressure drop according to section 4.1.

Table 4: Design specifications

Geometry, Capacity	Bed properties	Boundary conditions	Power, Mass flow
8x (Ø 8.9m, H=4.45 m)	ε_b=0.5, ε_p=0.4	$P_{out,d}$: 0.91 bar	8x P_d = 18.75 MW_{th}
8x 504 t_{Co3O4}	d_p=0.03 m	$P_{out,r}$: 0.91 bar	8x P_r = 18.75 MW_{th}
8x ~120-180 MWh_{th}		$T_{in,d}$: 1200°C	8x $m_{air,d}$ =56.4 kg/s
		$T_{in,r}$: 600°C	8x $m_{air,r}$ =54.6 kg/s

In this section air properties are calculated as a function of temperature and pressure.
The mass flow rate at the inlet is set according to the nominal power and the maximum temperature rise of the HTF of 300 K. The overall capacity depends on the sensible storage of the solid which is ~10%/100 K. Therefore it may vary between 120 (no sensible storage) and 190 MWh_{th} (ΔT_{solid}=600 K).
The gas and solid temperature change during one cycle is as follows: After the discharging process the solid temperature is 600°C. Then, during the charging process the air enters the reactor at 1200°C and is cooled to the equilibrium temperature of 900°C. In the end all solid material is heated up to the air inlet temperature of 1200°C. During the discharging process the air enters the storage system at 600°C and is heated up to the equilibrium temperature of 900°C. After the discharging process the solid temperature is again at 600°C.
Figure 5 and 6 show the thermal performance in terms of outlet temperature, conversion, power and consequent parasitic losses for the charging and discharging process.

In case of the charging process, the outlet temperature first rises to 900°C, heating up the solid from 600°C to 900°C. Afterwards, we find a constant outlet temperature, conversion rate and power level in Fig.5. The air mass flow is cooled down to the equilibrium of ~900°C, releasing 150 MWh_{th} within 6.2 hours. Due to the higher temperature drop of ΔT_{solid}=600 K instead of ΔT_{solid}=300 K the overall capacity increases to 190 MWh_{th} instead of the nominal capacity of 150 MWh_{th}. According to Fig.4 the mass flow rate is the limiting factor.

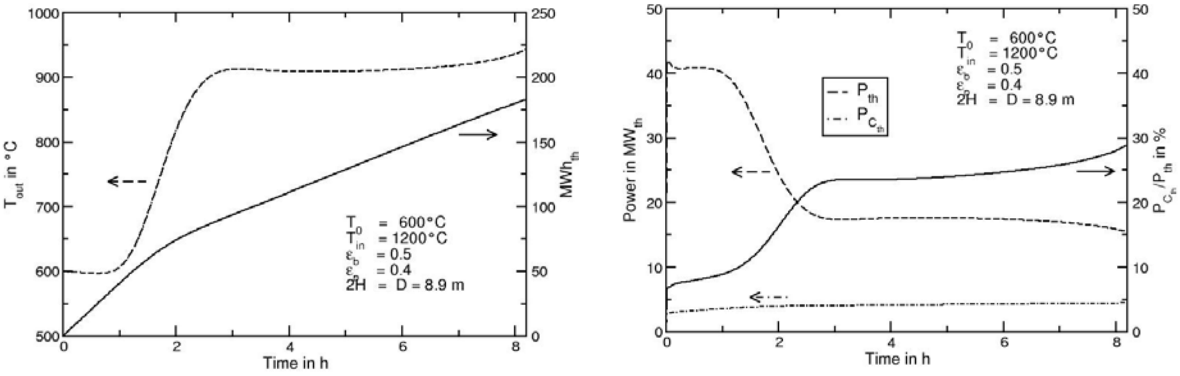

Figure 5: Performance during the charging process: $Co_3O_4+\Delta H \rightarrow 3\ CoO+0.5\ O_2$
Outlet temperature and conversion (left), power and parasitic losses (right)

In constrast to the power level, the parasitic losses due to pressure drop increase during the process. In the beginning the solid material has temperature of T_0=600°C. During the charging process the reaction zone develops, dividing the reactor into a hot and cold zone. Thus, the pressure drop increases due to higher gas velocity in the expanding hot zone. The demand of $P_{C,th}/P_{th}$<20% can only be met during the first four hours of the charging process.

Even though the integral over the first eight hours states 18%, the transient ratio increases up to 28%. Therefore particle diameters smaller than 3 cm are not acceptable in this fixed bed design with regard to the pressure drop.

In case of the discharging process the outlet temperature first drops to 900°C, cooling down the solid from 1200°C to 900°C. Afterwards, it remains constant at that level as seen in Fig.(6). Therefore the theoretical equilibrium temperature of ~900°C is reached. Similar to the charging process we find an overall capacity of 190 MWh_{th}. According to Fig.4 the mass flow rate is the limiting factor.

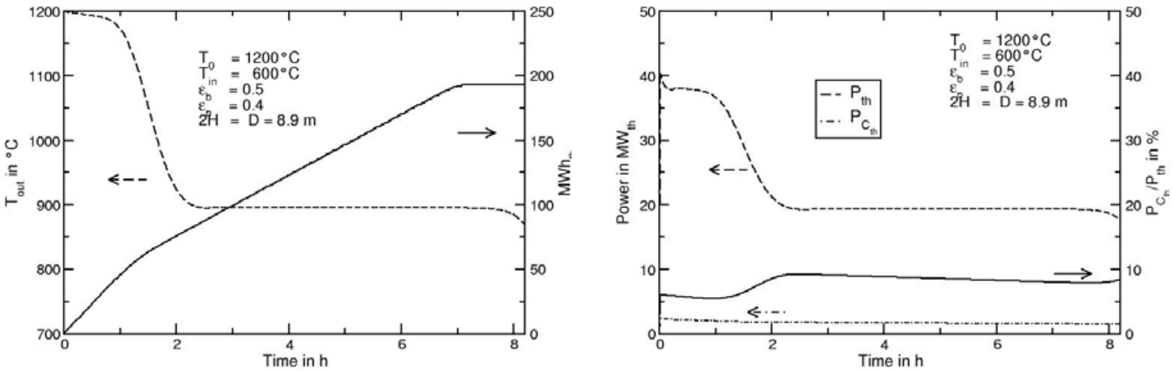

Figure 6: Performance during the discharging process: 3 CoO+0.5 $O_2 \rightarrow Co_3O_4+\Delta H$
Outlet temperature and conversion (left), power and parasitic losses (right)

The pressure drop is reduced with higher conversion because the cold zone expands during the process. Consequently, the parasitic losses are also diminished due to lower temperatures during the discharging process.
Figure 7 shows the cold and hot zones along the reactor length which develop in case of the charging and discharging process. In case of the charging process the reaction zone has a length of ~1.2 m whereas 90% of conversion are achieved after 0.5 m. In case of the discharging process it has a length of 0.8 m whereas 90% of conversion are achieved after 0.3 m.

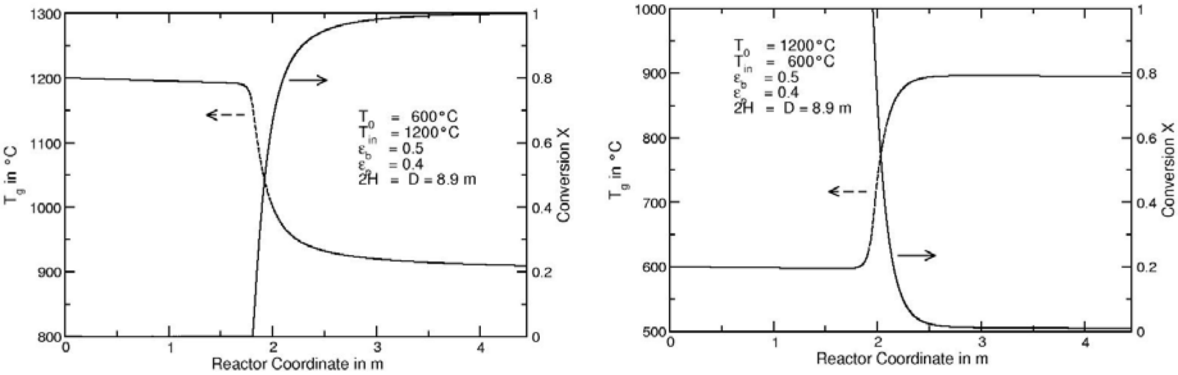

Figure 7: Reaction zone at t=4 h during the charging (left) and discharging (right) process

In general, a fixed bed of 3 cm particles shows promising performance in terms of temperature, power level and pressure drop. The parasitic losses due to pressure drop are below 18% in case of the charging and below 10% in case of the discharging process. However, it has to be evaluated in which way the particle size influences the overall process due to a decreased heat transfer or a reduced reaction rate.

4.2.2 Limitation due to heat transfer

According to Eqn.(15) the particle diameter has an impact on the overall heat transfer coefficient. Lower heat transfer rates may result in lower outlet temperatures as the heat of reaction can not be transferred sufficiently to the HTF. Moreover, the particle temperature will be close to equilibrium because of minor heat exchange. As the reaction kinetics slow down near equilibrium, the reaction rate is diminished as well. In contrast, smaller particles may increase the heat transfer rate, shorten the reaction zone and may result in higher outlet temperatures.
Figure 8 shows the outlet temperature for different particle diameters of 3, 5 and 10 cm for the charging (left) and discharging process (right), respectively.

In case of the charging process, it can be seen that the outlet temperature remains almost constant providing consequently a constant power level. The temperature level is slightly lower for 3 cm or 1 cm particles compared to those of a diameter of 10 cm. This is due to heat transfer limitation. In case of the charging process heat transfer coefficients of h~180 W/m^2K , h~100 W/m^2K or h~60 W/m^2K can be achieved which result in overall volumetric heat transfer coefficients of h_{sg}~45000 W/m^3K, h_{sg}~7800 W/m^3K or h_{sg}~1100 W/m^3K for particle diameters of 1 cm, 3 cm or 10 cm, respectively. 193 MWh_{th} (d_p= 1 cm), 180 MWh_{th} (d_p= 3 cm), or 157 MWh_{th} (d_p= 10 cm) could be transferred to the gas within 8 hours, respectively.

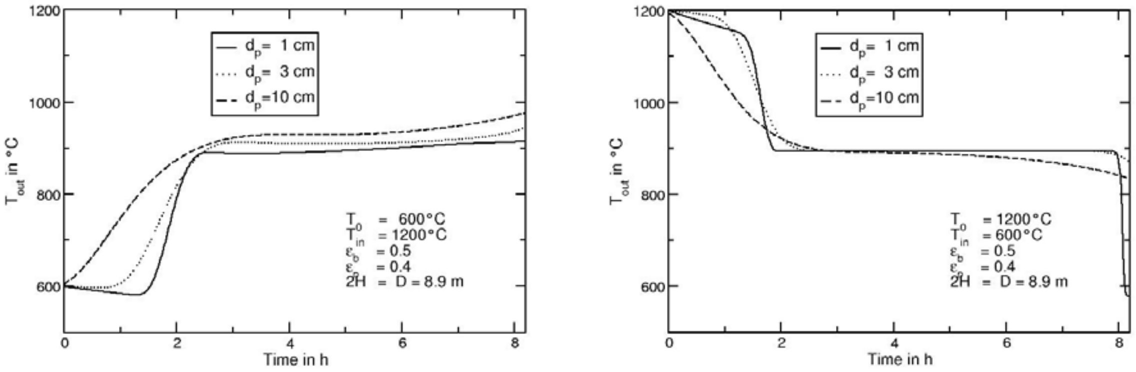

Figure 8: Performance during the charging (left) and discharging (right) process
Influence of particle diameter on outlet temperature

In case of the discharging process, it can be seen that the outlet temperature remains constant. Only a slight decrease can be observed for a bed of 10 cm particles. Heat transfer coefficients of h~170 W/m^2K , h~100 W/m^2K or h~60 W/m^2K can be achieved which result in overall volumetric heat transfer coefficients of h_{sg}~44000 W/m^3K, h_{sg}~7400 W/m^3K or h_{sg}~1100 W/m^3K for particle diameters of 1 cm, 3 cm or 10 cm, respectively. Similar to the charging process, the sensible heat of the system almost compensates the limitation due to heat transfer in case of 10 cm particles. 180-170 MWh_{th} could be transferred to the gas within 8 hours.

In general, a fixed bed of 3 cm particles shows promising performance in terms of heat transfer. Heat transfer coefficients are in the same range for the charging and discharging process. However, it still has to be discussed in which way a reduction of the reaction rate due to increasing particle diameters has a further impact on the process. As dissociation kinetics were found to be faster as the re-oxidation, this question will be addressed in the next section with regard to the discharging process.

4.2.3 Limitation due to the reaction rate

Experimental data of kinetics are provided for material in powder form only. Therefore the exact influence of the particle size on the thermal process can not be determined at this point. However, it can be discussed to which amount a reduction of the reaction rate would be acceptable. Therefore in this study varied effectiveness factors are implemented which result in a variation of the reaction rate according to Eqn.(3).

Figure 9 shows the outlet temperatures (left) and conversions (right) for a fixed bed of 3 cm particles and different effectiveness factors. In addition, for an effectiveness factor of η_R=0.001 the mass flow rates are varied in Fig.10 according to the nominal powers of 18.75 MW_{th}, 37.5 MW_{th} and 75 MW_{th} defined in Tab.3.

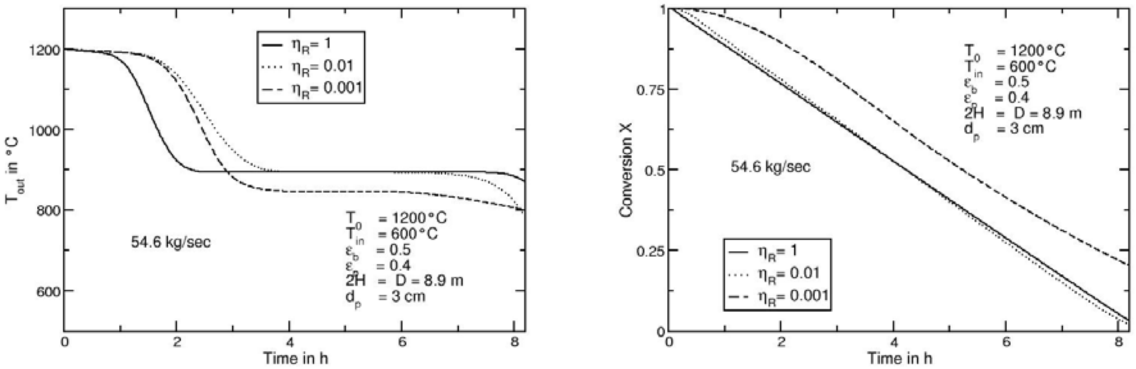

Figure 9: Performance during the discharging process, 54.6 kg/sec: 3 CoO+0.5 $O_2 \rightarrow Co_3O_4 + \Delta H$ Influence of the reaction rate

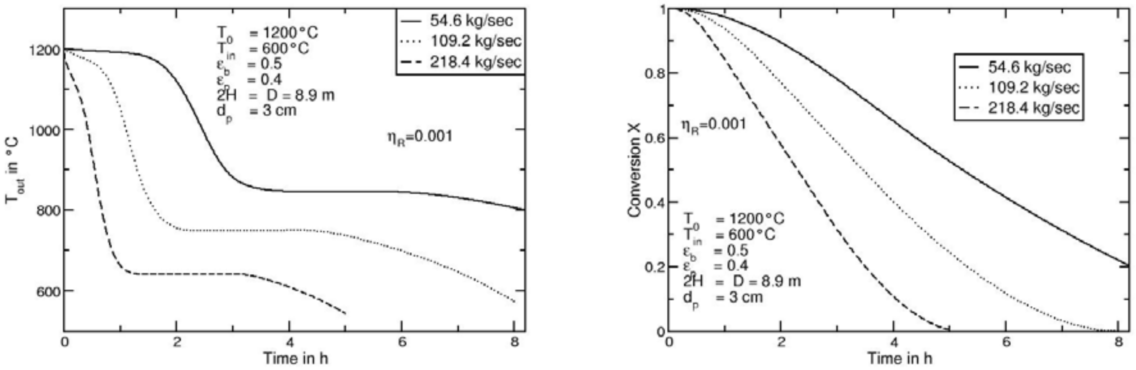

Figure 10: Performance during the discharging process, η_R=0.001: 3 CoO+0.5 $O_2 \rightarrow Co_3O_4 + \Delta H$ Influence of the mass flow rate

Good thermal performance with regard to outlet temperature and conversion can be observed for reduced reaction rates down to an effectiveness factor of η_R=0.01. Only for η_R=0.001 the level slightly decreases. However, this is only valid for power levels up to 18.75 MW_{th}. In case of higher mass flow rates the limitation is stronger as seen in Fig.10. Assuming an effectiveness factor of η_R=0.001, the demanded outlet temperature of 900°C can not be reached. For a nominal power of 18.75, 37 or 75 MW, the nominal discharge time is 8, 4 or 2 h but only 180, 145 or 94 MWh_{th} could be transferred to the air within that amount of time, respectively.

4.3 Conclusion

A thermochemical heat storage system based on the dissociation and re-oxidation of cobalt monoxide was investigated theoretically in terms of pressure drop, temperature distribution and power level. The proposed design of Tab.4 is a fixed bed with direct contact between the solid material and the heat transfer fluid (HTF) air. It consists of 8 cylindrical reactor units of ~120-190 MWh_{th} thermal storage capacity. The nominal power is 18.75 MW_{th} per reactor unit which corresponds to a mass flow rate of ~55 kg/s and a charging/discharging time of 8 hours. The solid temperature shifts between 600°C and 1200°C while the outlet temperature is ~900°C according to equilibrium conditions.

Because of the higher temperature level the pressure drop is more critical for the charging process. If 20% parasitic losses can be accepted and a mass flow rate of ~55 kg/s is set, a minimum particle size of 3 cm and a temperature drop of the HTF between inlet and outlet of at least 300 K is required.
On the other hand, in a bed of bigger particles heat transfer limitation may become an issue. As an increase/decrease of the outlet temperature could be observed for the charging/discharging process for particle diameters larger than 3 cm, a maximum particle diameter of 3 cm is preferable.
Assuming that the reaction kinetics are comparable to those of the powder form, a constant outlet temperature can be achieved during the charging and discharging process. A reduction of the reaction rate could be in principle acceptable down to 1% of kinetics of powder.
The investigation of the heat transfer and kinetic limitation is valid for a power level up to 18.75 MW_{th}. In case of higher mass flow rates these limitations may become more critical.

The theoretical performance of the investigated thermochemical storage system is promising for solar thermal applications. Future work items in order to implement a prototype are proposed as follows:

- Formation of stable particle structures with comparable kinetics
- Determination of the impact of particle size on kinetics
- Study of tank cost versus cost as a result of pumping power
- Investigation of different reactions at lower temperature levels (charging process)
- Investigation of different bed configurations, e.g. fluidized beds or rotary kilns

5 References

[1] Gnielinski, V., 2006. “Wärmeübertragung Partikel-Fluid in durchströmten Haufwerken, Abschnitt Gj”. In VDI-Wärmeatlas, 10 ed.

[2] Span, R., 2006. “Stoffwerte von Luft, Abschnitt Dbb1”. In VDI-Wärmeatlas, 10 ed.